CHARGE AND ENERGY TRANSFER DYNAMICS IN SINGLE-WALL CARBON NANOTUBE ENSEMBLES

By

Jared J. Crochet

Dissertation

Submitted to the Faculty of the

Graduate School of Vanderbilt University

In partial fulfillment of the requirements

for the degree of

DOCTOR IN PHILOSOPHY

in

INTERDISCIPLINARY MATERIALS SCIENCE

December, 2007

Nashville, TN

Approved :

Tobias M. Hertel

Richard F. Haglund

Sandra J. Rosenthal

Kalman Varga

Sharon M. Weiss

ACKNOWLEDGEMENTS

This dissertation would not be possible if it were not for our many fruitful collaborations. I would like to thank the following people and organizations for their efforts:

Nanotube Synthesis-
D. Resasco - Northwestern University

Nanotube Sorting-
M. Arnold and M. Hersam - Northwestern University
D. Heller and M. Strano - Massachusetts Institute of Technology
F. Bonaccorso and A. Ferrari - Cambridge University
K. Mueller and C. Reichert - Karlsruhe

Vacuum Filtration Films-
K. Aguirre and R. Martel - Universite de Montreal

Spectroscopy-
L. Luer and G. Lanzani - Politecnico di Milano
K. Arnold and M. Kappes - Karlsruhe

Theory-
V. Perebeinos and P. Avouris - IBM

I also acknowledge my mentor and advisor, T. Hertel, who was instrumental in preparing me for this dissertation. Finally, I owe my gratitude to my wife, L. Crochet, who endeavored 3.5 years of graduate student life while giving birthing and raising our two sons.

TABLE OF CONTENTS

LIST OF FIGURES

Chapter 1 **Page**

Chapter 2

Chapter 3

Chapter 4

Chapter 5

INTRODUCTION

The understanding of charge and energy transfer dynamics in electro-optic materials is essential for a microscopic description of their optical properties and transport phenomena. In nanophase materials, where quantum confinement effects are pronounced, departure from bulk-like properties may become evident and is of both fundamental and applied interest [Ada03]. Single-wall carbon nanotubes (SWNTs) belong to a unique class of one-dimensional nanoscale materials due to their extraordinarily large aspect ratio, outstanding transport and mechanical properties, and high chemical stability [Bau02]. The graphitic surface of SWNTs is inert and its one-dimensional electronic structure and its dynamical properties support conduction with extremely long ballistic mean free paths. In addition, it was recently shown that nanotubes also exhibit intriguing optical properties that can be traced back to the peculiarities of the Coulomb interaction between charge carriers in low-dimensional systems [And97]. The optical spectra are found to be dominated by strongly bound excitons and have stimulated research in optical science and technology for carbon nanotubes.

Nonetheless, implementation of SWNTs in new technologies has in part been hampered because of sample heterogeneity and insufficiently low photoluminescence (PL) quantum yields (QYs) of less than 0.1% [O'co02, Wan05]. It is therefore of practical and fundamental scientific interest to better understand the microscopic mechanisms that are responsible for low photoluminescence quantum yields and to explore whether the emission efficiency can be increased. Motivated by this grand

challenge, the specific aim of this dissertation is to understand the influence of dimensionality and local dielectric environment on charge-carrier dynamics and photoluminescence quantum yields in semiconducting carbon nanotubes. This dissertation is divided into three major section in which a) a technology is developed to purify nanotube samples and systematically control the local dielectric environment by structural sorting of nanotube crystallites, and b) ultra-fast and continuous wave (CW) spectroscopy is used to investigate intratube and c) intertube energy and charge transfer in semiconducting nanotube samples.

Improved synthesis of carbon nanotubes today allows reducing sample heterogeneity considerably. Recently developed catalysts for example now allow to obtain samples with a high percentage of (6,5) carbon nanotubes [Kit00], recently found to be approximately 40% by Raman spectroscopy [Jor05]. Additionally, fluorescent nanotube suspensions can readily be made by aqueous surfactant encapsulation via ultrasonication [O'Co02]. Density-gradient ultracentrifugation, which sorts colloidal particles by their buoyant density, has recently been shown to provide a tool for sorting isolated nanotubes by their structure and metallicity [Arn06]. Smaller diameter nanotubes tend to be more buoyant while larger diameter tubes tend to be the least buoyant. The abovementioned structural sorting technique is used in this work as a basis for the development of a technology to structurally sort nanotube *crystallites* – small nanotube bundles - by their buoyant density. Within the work discussed here size selection of crystallites is used as a means to tailor the local dielectric environment so as to provide a desired degree of screening of the Coulomb interaction between the electron and hole that constitute the exciton. In addition, the magnitude of the dielectric function

can be controlled by engineering crystallites to be composed of a majority of metallic or semiconducting tubes.

Charge carrier dynamics in heterogeneous nanotube ensembles have been investigated extensively using ultra-fast pump-probe as well as CW spectroscopies with little consensus of the decay mechanisms over the past five years [Lau03, Kor04, Kon04, Ost04, Jon05]. Linear absorption and fluorescence spectra of a system with well defined resonances – such as SWNTs – can under favorable circumstances be used to gather information on dephasing times of excitonic or free carrier like photo-excitations. Ultra-fast pump-probe spectroscopy provides complementary information to CW spectroscopy by directly probing recovery of the ground state as well as excited state dynamics. At the outset of this dissertation charge carrier dynamics in SWNTs had been studied using strongly heterogeneous samples which can lead to ambiguities in the interpretation of both linear and non-linear optical spectra. In this thesis traditionally prepared colloidal suspensions of nanotubes are found to contain a majority of non-fluorescing SWNT crystallites whose spectral weight contributes strongly to the overall absorbance but reduces the effective quantum yield by orders of magnitude if compared to isolated tubes. Additionally, the CW spectral features are broadened in-homogeneously due to local variations in the dielectric function determined by the statistical average of crystallite constituents.

Here, we are able resolve CW line-widths ,determine PL QYs, and investigate microscopic decay mechanisms of samples that are homogeneous with respect to crystallite size, but heterogeneous with respect to isolated tube variations – such as defects and lengths. This allows for the proper investigation of isolated tube's ensemble

averaged quantum yield and decay mechanisms from energetically higher lying excitonic states to lower lying excitonic states or the ground state. Moreover, the evolution of CW spectra, PL QY, and dynamics with increasing dielectric function of the environment is investigated within structurally sorted SWNT crystallites. This provides new insight into the importance of the screened Coulomb interaction between electrons and holes in semiconducting SWNTs. This work will also allow to study ultra-fast electron transfer mechanisms between neighboring tubes and how these can quench fluorescence.

References

[Ada03] Adams, D. M., L. Brus, et al. (2003). "Charge transfer on the nanoscale: Current status." Journal of Physical Chemistry B **107**(28): 6668-6697.

[And97] Ando, T. (1997). "Excitons in carbon nanotubes." Journal of the Physical Society of Japan **66**(4): 1066-1073.

[Arn06] Arnold, M. S., A. A. Green, et al. (2006). "Sorting carbon nanotubes by electronic structure using density differentiation." Nature Nanotechnology 1(1): 60-65.

[Bau02] Baughman, R. H., A. A. Zakhidov, et al. (2002). "Carbon nanotubes - the route toward applications." Science **297**(5582): 787-792.

[Jon05] Jones, M., C. Engtrakul, et al. (2005). "Analysis of photoluminescence from solubilized single-walled carbon nanotubes." Physical Review B **71**(11).

[Jor05] Jorio, A., A. P. Santos, et al. (2005). "Quantifying carbon-nanotube species with resonance Raman scattering." Physical Review B 72(7).

[Kit00] Kitiyanan, B., W. E. Alvarez, et al. (2000). "Controlled production of single-wall carbon nanotubes by catalytic decomposition of CO on bimetallic Co-Mo catalysts." Chemical Physics Letters **317**(3-5): 497-503.

[Kon04] Kono, J., G. N. Ostojic, et al. (2004). "Ultra-fast optical spectroscopy of micelle-suspended single-walled carbon nanotubes." Applied Physics a-Materials Science & Processing **78**(8): 1093-1098.

[Kor04] Korovyanko, O. J., C. X. Sheng, et al. (2004). "Ultrafast spectroscopy of excitons in single-walled carbon nanotubes." Physical Review Letters **92**(1).

[Lau03] Lauret, J. S., C. Voisin, et al. (2003). "Ultrafast carrier dynamics in single-wall carbon nanotubes." Physical Review Letters **90**(5).

[O'co02] O'Connell, M. J., S. M. Bachilo, et al. (2002). "Band gap fluorescence from individual single-walled carbon nanotubes." Science **297**(5581): 593-596.

[Oga91] Ogawa, T. and T. Takagahara (1991). "Optical-Absorption and Sommerfeld Factors of One-Dimensional Semiconductors - an Exact Treatment of Excitonic Effects." Physical Review B **44**(15): 8138-8156.

[Ost04] Ostojic, G. N., S. Zaric, et al. (2004). "Interband recombination dynamics in resonantly excited single-walled carbon nanotubes." Physical Review Letters **92**(11).

[Wan05] Wang, F., G. Dukovic, et al. (2005). "The optical resonances in carbon nanotubes arise from excitons." Science **308**(5723): 838-841.

Publications

This dissertation is based on the following publications:

T. Hertel, Z. Zhu, J. Crochet, C. McPheeters, H. Ulbricht, and D. Resasco, "Exciton Dynamics Probed in Carbon Nanotube Suspensions with Narrow Diameter Distribution," Physica Status Solidi (b), Vol. 243, Issue 13, 3186-3191, 2006.

Zipeng Zhu, Jared Crochet, Michael Arnold, Mark Hersam, Hendrik Ulbricht, Daniel Resasco, and Tobias Hertel, "Pump Probe Spectroscopy of Exciton Dynamics in (6,5) Carbon Nanotubes," The Journal of Physical Chemistry C, Vol. 111, Issue 10, 3831-3835, 2007.

Jared Crochet, Michael Clemens, and Tobias Hertel, "Quantum Yield Heterogeneities of Aqueous Single-wall Carbon Nanotube Suspensions," Journal of the American Chemical Society, Vol. 129, Issue 26, 8050-8059, 2007.

J. Crochet, M. Clemens, and T. Hertel, "Optical Properties of Structurally Sorted Single-wall Carbon Nanotube Ensembles," Physica Status Solidi (b), Vol. 244, Issue 11, 3964-3968, 2007.

T. Hertel, V. Perebeinos, J. Crochet, K. Arnold, M. Kappes, and Ph. Avouris, "Intersubband Decay of 1-D Exciton Resonances in Carbon Nanotubes," Nano Letters, In Press, 2007.

Larry Lüer, Sajjad Hoseinkhani, Jared Crochet, Tobias Hertel, Guglielmo Lanzani., "Direct Determination of Exciton Size and Mobility in (6,5) Carbon Nanotubes," In Preparation.

J. Crochet, F. Bonnacorso, A. Ferrari, T. Hertel, "Engineering of (n,m) Specific Single-wall Carbon Nanotube Crystallites," In Preparation.

J. Crochet, T. Hertel, "Exciton Dynamics in Single-wall Carbon Nanotube Crystallites," In Preparation.

CHAPTER I

REVIEW OF THE ELECTRONIC STRUCTURE OF AROMATICS

Aromaticity is a common property among sp^2 bonded carbon in both molecular and bulk forms. The size extrema of the aromatics are benzene, the minimum, and graphene, the maximum. Even though the sizes of these carbon compounds vary greatly, their physical properties can be described by delocalized π electrons. An overview of the physical structure, simplified electronic structure, and optical properties of benzene and graphene is given as a prelude to a physical description of single-wall carbon nanotubes (SWNT). Moreover, the importance of dimensionality, excitons, and symmetry for the optical properties of SWNT is discussed. Nanotubes may be considered to lie in the middle of the extremes of aromaticity and implications of this hypothesis are reviewed in terms of both molecular and bulk-like behaviors of the relaxation of photoexcited states.

A. The Size Extremes of Aromaticity

1. Benzene: The Prototypical Aromatic

According to Hückel's rule, planar ring molecules consisting of $4n+2$ π electrons (where n is positive integer) can be estimated to be aromatic [Wil65]. Aromaticity is believed to further stabilize σ bonded planar ring molecules by the contribution of each

atomic constituent to a delocalized molecular wavefunction. As the size of the molecule gets larger and the screening of the repulsion between carbon atoms gets larger aromaticity may still be observed even though the 4*n*+2 rule fails. The prototypical aromatic hydrocarbon is the benzene ring that is composed of six carbon atoms in a hexagonal cycle that are hydrogen terminated. The full hexagonal symmetry of this planar structure belongs to the dihedral D_{6h} symmetry group which describes the six-fold symmetry consisting of six mirror planes between the carbon atoms and six rotations which bring the atoms onto themselves, Fig. 1. a. This symmetry is also important to the description of both graphene and single-wall carbon nanotubes. It is very helpful for the discussion of extended π electron systems such as graphene to introduce the electronic structure of benzene in terms of delocalized π electrons, according Hückel's rule, which captures the irreducible symmetry of the molecular orbitals (MO) using group theory [Wil65, Fre00, Sch01]. In reality the electronic structure is much more complicated due to the coupling of the electronic states to vibrational degrees of freedom of the nuclei, the presence of the terminating hydrogen atoms, and the electron-electron interaction. In simple terms, the wave function of each orbital can be written as,

$$\psi_k(\vec{r}) = e^{ik\theta}\eta_k(\vec{r}), \tag{1}$$

where $\eta(\vec{r})$ is the atomic orbital, p_z in this case, and the phase factor dependent on the azimuthal angle θ is determined by the quantum numbers $k = 0,\pm1,\pm2,...\pm n-1$, where n is the number of π electrons. This arises from the cyclic boundary condition imposed on a free particle confined to a ring. The Hückel tight binding eigenvalues are given by,

$$\varepsilon_k = \varepsilon_0 - 2t\cos\left(\frac{2\pi k}{n}\right), \tag{2}$$

where the on-site energy of a π electron at atomic site $\vec{r}$ is given by $\varepsilon_0 = \langle \eta_k(\vec{r}) | H | \eta_k(\vec{r}) \rangle$ and the hopping energy of moving a π electron from site $\vec{r}$ to nearest neighbor $\vec{r}'$ is given by $t = \langle \eta_k(\vec{r}) | H | \eta_k(\vec{r} \pm \vec{r}') \rangle$ [Wil65]. The Hamiltonian used here, *H*, is consider to be a single-particle operator that depends on only one electronic coordinate at a time. Benzene's lowest energy orbital in this model contains six π electrons all in phase, given by symmetry-adapted linear combination notation (SALC) $1a_{2u}$, with energy $\varepsilon_0 - 2t$.

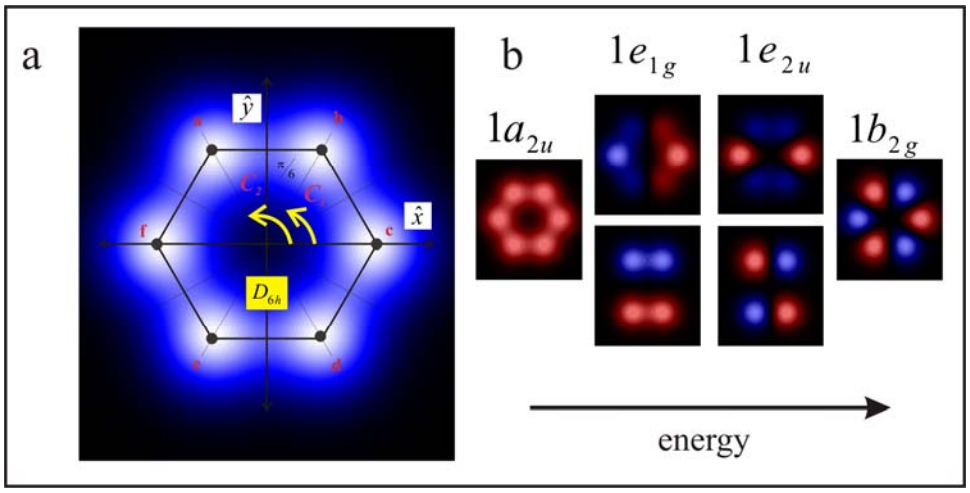

Figure 1. a. Physical structure of benzene approximated by a linear combination of *p* atomic orbitals locates at each of the six carbon atoms**. b.** The orbital wavefunctions of benzene within the LCAO approximation according to Hückel's rule. Red is positive amplitude and blue is negative amplitude. The symmetry characters of the hexagonal group label the orbitals.

This molecular orbital is responsible for the additional stability of the structure. The highest occupied molecular orbital (HOMO) $1e_{1g}$ will be doubly degenerate and has energy $\varepsilon_0 - t$ and the lowest unoccupied molecular orbital (LUMO) $1e_{2u}$ will also be

doubly degenerate with energy $\varepsilon_0 + t$. The energetically highest state $1b_{2g}$ will have six π electrons all out of phase with each other with energy $\varepsilon_0 + 2t$, Fig. 1. b.

Since electrons are fermions, spin is important in the energetic ordering of electronic states which is determined by the strength of the Coulomb interaction. In general electron wavefunctions are written as, $|\Psi\rangle = N|\psi\rangle|\chi\rangle$, where N is a normalization factor, $|\psi\rangle$ is the spatial wavefunction, and $|\chi\rangle$ is the spinor. Depending on the pairing of spins, they can be labeled as triplet or singlet states determined by parallel/anti-parallel and symmetric/anti-symmetric combinations of single spins. Singlet states describe an electronic level containing antisymmetric anit-parallel spins. In simple terms of atomic notation, the total spin angular momentum s is zero and the spin projection m_s is also zero. The spin wave function can be written as an antisymmetric combination of single electron spinors according to:

$$|\chi_1\rangle = |\uparrow\downarrow\rangle - |\downarrow\uparrow\rangle. \tag{3}$$

The triplet states have spin angular momentum $s = 1$ and the spin projection can range from $m_s = -1,0,+1$, and a symmetric combination of single electron spinors. The three triplet spin wavefunctions are,

$$|\chi_3^{+1}\rangle = |\uparrow\uparrow\rangle, |\chi_3^{-1}\rangle = |\downarrow\downarrow\rangle, |\chi_3^{0}\rangle = |\uparrow\downarrow\rangle + |\downarrow\uparrow\rangle. \tag{4}$$

Including the electron-electron interaction the eigenstates of the many-body Hamiltonian become linear combinations of the molecular orbitals in Fig. 1. b. and are labeled by their symmetries associated with the SALC orbitals. Due to the electron-electron interaction, the singlet ground state (S_0) of benzene, $1A_{1g}$, is a sum of the HOMO orbitals, $1e_{1g}$, and

the lowest energy orbital, $1a_{2u}$ [Hay74]. The singlet excited states (S_n) and triplet states (T_n) contain many different combinations of the orbitals from Fig. 1, but only a few can be accessed by spectroscopic methods due to selection rules which are directly related to the symmetry of the wave functions that make up the ground and excited states.

Due to the strong coupling between the vibrational coordinates (Q) and the electronic states, molecular excitations are modeled as discrete transitions between potential energy surfaces [Yar01]. This is done within the limits of the Born-Openheimer approximation and allows for the adiabatic evolution of the electronic Schrödinger equation on a potential energy surface (PES) associated with the motion of the nuclei. The electronic singlet ground state in its vibrational ground state can be coupled to an excited singlet state (S_n) by an external field, Fig. 2. a. The most straightforward way to access the excited singlet energy levels is through absorption spectroscopy, which couples the singlet ground state to excited singlet states through an electromagnetic field. In principle, the frequency-dependent absorption coefficient $\alpha(\omega)$ can be calculated with the aid of Fermi's golden rule as,

$$\alpha(\omega) = \frac{16\pi e^2}{\omega^2} \sum_n \left|\langle S_n | H' | S_0 \rangle\right|^2 \rho(\hbar\omega - \Omega_n), \tag{5}$$

where photons of energy $\hbar\omega$ connect the singlet ground state to excited singlet states weighted by the oscillator strength (OS) of the n^{th} transition $f = C\left|\langle S_n | H' | S_0 \rangle\right|^2$, where C is a constant, and the density of states (DOS) is $\rho(\hbar\omega - \Omega_n)$ [Vol04]. The interaction Hamiltonian can be approximated by dipole operator, $H' = e\vec{r} \cdot \vec{E}$, where $\vec{r}$ is an electronic coordinate and $\vec{E}$ is the electric field vector of the incident wave. For

molecules such as benzene the wavefunctions $|S\rangle$ will be composed of a product of electronic and vibrational wavefunctions in accordance with the adiabatic approximation, and the Franck-Condon principle is implied such that the OS is reduced to $|\langle\varphi_n|\varphi_0\rangle|\langle\psi_n|H'|\psi_0\rangle|^2$ where $|\langle\varphi_n|\varphi_0\rangle|^2$ is the Franck-Condon factor that weights the degree of vibrational overlap of the excited and ground state wavefunctions [Con26]. In principle the stronger the vibrational overlap, the stronger the transition.

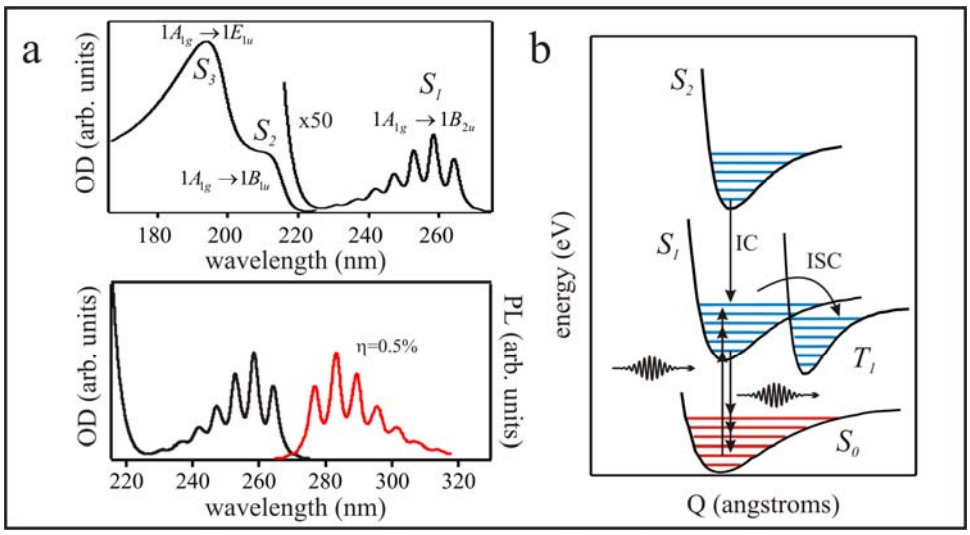

Figure 2. a. Schematic of the singlet absorption and emission spectra of benzene reproduced from [Ina72]. When dissolved in hexane the fluorescence quantum yield is 0.5%. **b.** The electronic structure dependence on the molecular configuration Q within the Born-Oppenheimer approximation. Excitation to higher-energy singlet excited states decay to lower-energy singlet excited states by internal conversions (IC) and radiative decay can follow. The potential energy surface crossings of the excited singlet and triplet states can facilitate an intersystem crossing (ISC) that leads to phosphorescence or non-radiative decay.

The absorption spectrum of liquid benzene has three dominant features that could be assigned by *ab initio* calculations to specific electronic transitions [Ina72]. The transitions are very broad due to the many vibrational sidebands from the strong electron-

phonon coupling mentioned above, Fig. 2. a. The first excited-state band (S_1) has a relatively weak oscillator strength and is an excitation from the $1A_{1g}$ ground state to the $1B_{2u}$ state which is a sum of the $1e_{1g}$ and $1e_{2g}$ orbitals. The next band (S_2) is moderately strong and is assigned as the transition form $1A_{1g}$ to $1B_{1u}$ which is a sum of the $1a_{2u}$ and $1b_{2g}$. The highest state (S_3) is very strong and is assigned as E_{1u} which is a sum of $1a_{2u}$ and $1e_{1g}$. The fluorescence spectrum is in general a mirror image of the first excited singlet-state transition S_1.

The fluorescence quantum yield of benzene dissolved in hexane exciting at S_1 transition was reported to only be 0.5% [Daw68]. This implies that most of the absorbed energy from the incoming light is diverted into channels that are not optically active. Internal conversions (IC) are responsible for the non-radiative decay of the excited singlet states to the singlet ground state and are usually mediated by phonons, Fig. 2.a. Also, intersystem crossing (ISC) of singlet states into triplet states are responsible for non-radiative decay and has been studied extensively in benzene [Hen70, Bur69]. Spin orbit coupling is known to play a role in the ISC mechanism in benzene despite the relatively small atomic number of carbon.

2. Graphene: The Infinite Polycyclic Aromatic

The other aromatic extreme is graphene. It consists of an infinite sheet of carbon atoms arranged in a hexagonal lattice, Fig. 3. a . The two-atom unit cell is defined by the lattice vectors,

$$\vec{a}_1 = \frac{a}{2}\hat{x} + \frac{\sqrt{3}a}{2}\hat{y} \text{ and } \vec{a}_2 = \frac{a}{2}\hat{x} - \frac{\sqrt{3}a}{2}\hat{y} \tag{6}$$

where a is the carbon-carbon bond length [Wal47]. As in benzene, the electronic structure can be described by delocalized π electrons, and again the D_{6h} symmetry group reduces the complexity of the problem.

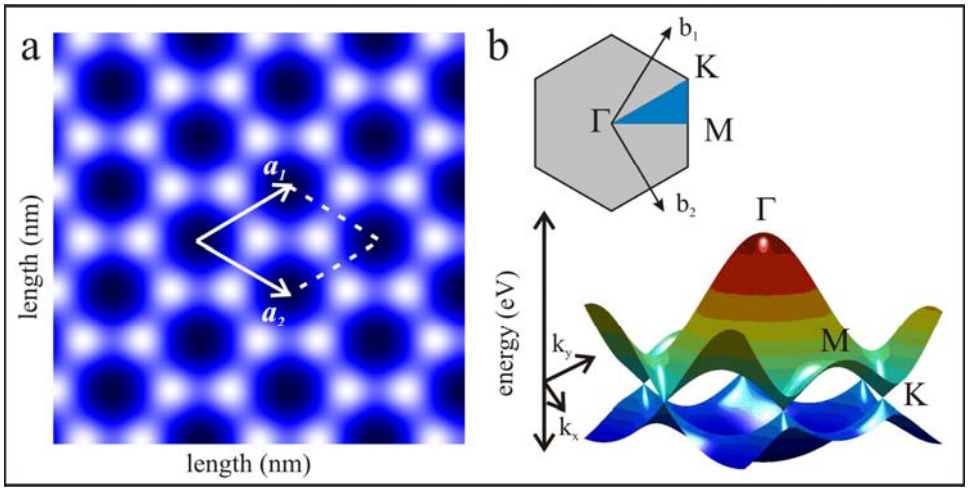

Figure 3. a. Real space lattice of graphene represented by a linear combination of *p* atomic orbitals. **b.** The first Brillouin zone of the reciprocal lattice (blue) and the dispersion of the π and π* bands plotted in two dimensional momentum space. The high symmetry points in momentum space are labeled. The π and π* bands approach each other as a cone (Dirac cone) and touch at the K point.

The symmetry of the reciprocal lattice, given by the vectors,

$$\vec{b}_1 = \frac{2\pi}{\sqrt{3}a}\hat{x} + \frac{2\pi}{a}\hat{y} \text{ and } \vec{b}_2 = \frac{2\pi}{\sqrt{3}a}\hat{x} - \frac{2\pi}{a}\hat{y}, \tag{7}$$

is the same as the real-space lattice and allows one to use the irreducible symmetry of the hexagon to construct the first Brillouin zone (FBZ) labeled by the high symmetry points Γ, M, K, Fig. 3. b. Within the nearest neighbor (NN) tight binding method the dispersion relation for the π and π^* crystal orbitals are [Sai92],

$$\varepsilon_{\vec{k}}^{\pi,\pi^*} = \varepsilon_0 \pm \frac{t\sqrt{3+2\cos\left(\vec{k}\cdot\vec{R}_1\right)+2\cos\left(\vec{k}\cdot\vec{R}_2\right)+2\cos\left(\vec{k}\cdot\vec{R}_3\right)}}{1+s\sqrt{3+2\cos\left(\vec{k}\cdot\vec{R}_1\right)+2\cos\left(\vec{k}\cdot\vec{R}_2\right)+2\cos\left(\vec{k}\cdot\vec{R}_3\right)}}, \quad (8)$$

where ε_0 and t are the same integrals defined in the previous section, s is the overlap of π orbitals on neighboring sites defined as $s = \left\langle \eta_k\left(\vec{r}\right) \middle| \eta_k\left(\vec{r} \pm \vec{R}_i\right) \right\rangle$, and $\vec{R}_i$ are the nearest neighbor atomic positions.

The eigenvalues are no longer discrete as in the case of benzene, but take on continuous values of k_x and k_y, which are wavevectors or crystal momentum vectors associated with the reciprocal lattice. The positive root corresponds to the anitbonding band of the crystal orbital π^*, and the negative root to the bonding band of the crystal orbital π, or equivalently the electron band and hole band. The on-site energy is chosen as the Fermi level $\varepsilon_0 = 0$, and the hopping energy and overlap integral are chosen for best agreement with *ab initio* calculations $t = -3.033eV, s = 0.129$ according to [Sai92]. The π and π^* bands versus crystal momentum in the 2D reciprocal graphene plane is shown in figure 3. b. At the Γ point the dispersion takes on the maximum/minimum value and all of the molecular orbitals within the π/π^* crystal orbital are in phase/out of phase as in the molecular orbitals of benzene. Moreover, near the K point the bands approach each other linearly as a cone (referred to as the Dirac cone [Nov05]) and touch at the K point making graphene a semimetal or zero-gap semiconductor.

In order to understand the optical response of graphene it is useful analyze the symmetry of the crystal wave functions and the energy dependence of the oscillator strength. The crystal wavefunctions of the π and π^* bands are given by,

$$\psi_{\vec{k}}^{\pi}\left(\vec{r}\right) = e^{i\vec{k}\cdot\vec{R}_A}\eta\left(\vec{r}-\vec{R}_A\right) + e^{i\vec{k}\cdot\vec{R}_B}\eta\left(\vec{r}-\vec{R}_B\right) \text{ and } \psi_{\vec{k}}^{\pi^*}\left(\vec{r}\right) = e^{i\vec{k}\cdot\vec{R}_A}\eta\left(\vec{r}-\vec{R}_A\right) - e^{i\vec{k}\cdot\vec{R}_B}\eta\left(\vec{r}-\vec{R}_B\right), \quad (9)$$

where $\vec{R}_A$ and $\vec{R}_B$ are the positions of the two atoms in the unit cell. The electron and hole wavefunctions and their products at the K and M points are given in Fig. 4.a. The crystal momentum dependent OS in eq. 7 becomes $\left|\left\langle \psi_{\vec{k}}^{\pi} \left| H' \right| \psi_{\vec{k}}^{\pi^*} \right\rangle\right|^2$ and can be calculated within the dipole approximation by averaging all of the dipole crystal momentum integrals connecting electrons and holes within the FBZ at fixed e-h energy , Fig. 4.b. It is straightforward to see from the product wavefunctions in Fig. 4.a. why the oscillator strength vanishes at the K point due to the lack of an induced dipole moment in the plane, i.e. zero charge separation.

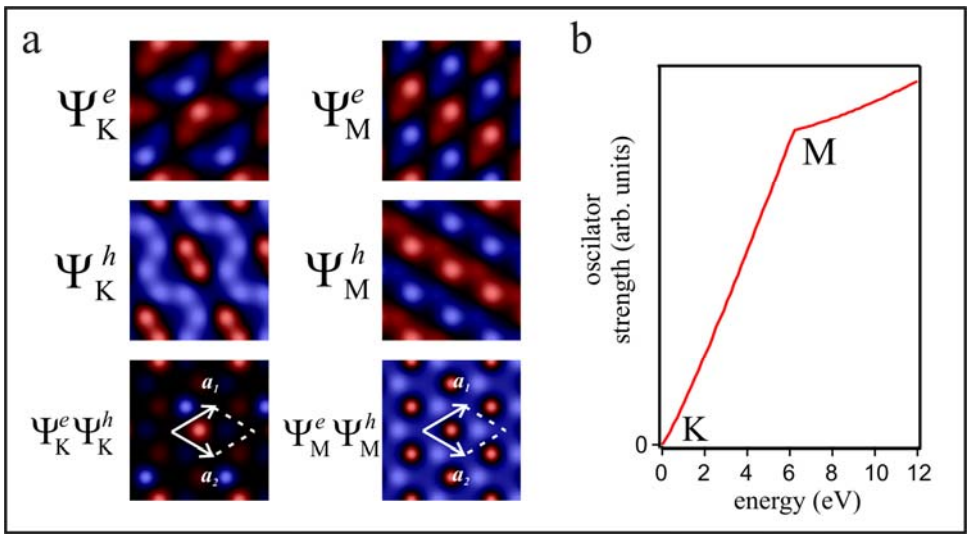

Figure 4.a. Real part of the tight binding Bloch wavefunctions for the electron, hole, and electron times hole at the high symmetry points K and M. **b.** The tight binding oscillator strength of graphene as a function of photon energy for light polarized along the x-axis.

The DOS of the electrons and holes is calculated by adding all of the states up for a fixed energy within the FBZ and is formally given by $DOS^{\pi} = \rho\left(\hbar\omega - \varepsilon^{\pi}\right)$ and $DOS^{\pi^*} = \rho\left(\hbar\omega - \varepsilon^{\pi^*}\right)$, Fig. 5.a. Approaching the K point, the DOS for electrons and

holes as well as the joint density of states, $JDOS^{\pi,\pi^*} = \rho\left(\hbar\omega - \varepsilon^{\pi} + \varepsilon^{\pi^*}\right)$, vanishes similarly to the OS, which makes spectroscopic study of low energy electronic excitations difficult [Pai70]. Conversely, Raman spectroscopy of graphene in the visible wavelength range is possible and provides information on the effects of layer stacking and the peculiarities of the linear electronic dispersion relation [Fer06]. Also using nonlinear spectroscopy, excitations in graphite show an energy dependence of the relaxation rate by scattering with the continuum of free e-h pairs belonging to the linear bands, and in turn give their energy to the lattice by emission of phonons [Moo01, Xu96, Sei90], Fig. 5.b.

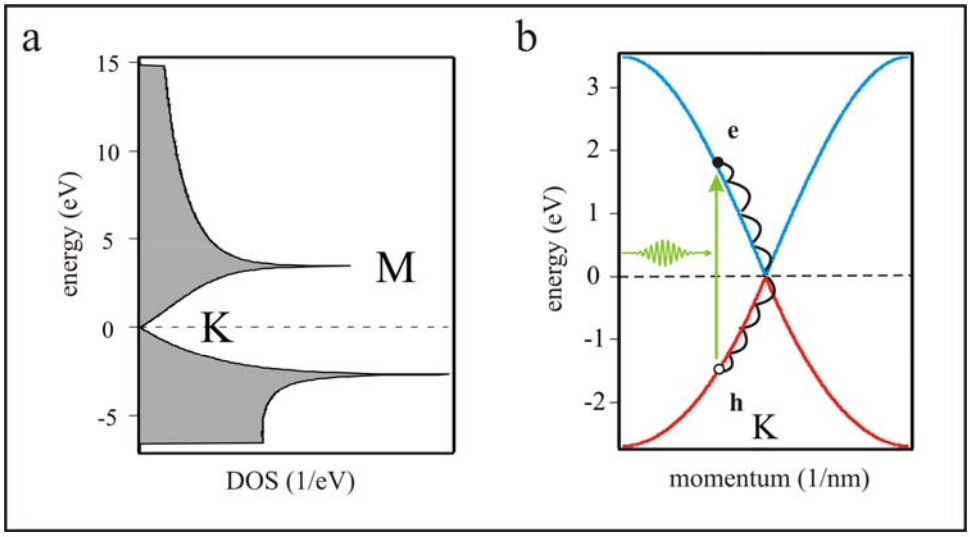

Figure 5. a. The density of states of graphene, the linear dispersion relation leads to a vanishing density of states at the Fermi level. **b.** Electronic relaxation pathway for photoexcited states near the K point.

B. Single-wall Carbon Nanotubes: Infinite Polycyclic with a Twist

Single-wall carbon nanotubes (SWNTs) are tubules of graphene that vary in diameter depending on how they are cut from the graphene sheet. For all practical purposes they are treated as one-dimensional materials and quantization of graphene wavevectors along the circumferential direction can be used to approximate the electronic structure [Ham92, Min95]. The unit cell is defined by two vectors on the graphene plane; a translational vector that maps out the length of the unit cell along the tube axis, $\vec{T}$, and a chiral vector that defines the circumference, $\vec{C}_h$ [Sai92, Tan92]. They are both defined in terms of the graphene lattice vectors $\vec{a}_1$ and $\vec{a}_2$ and integers (n,m) as

$$\vec{T} = \frac{2m+n}{d_R}\vec{a}_1 + \frac{2n+m}{d_R}\vec{a}_2 \text{ and } \vec{C}_h = n\vec{a}_1 + m\vec{a}_2, \tag{10}$$

where d_R is the greatest common devisor of $2m+n$ and $2n+m$. When $n=m$ the tube is classified as armchair, zigzag when $m=0$, and all other $n \neq m$ are chiral. The unit cell of the *(6,5)* tube is mapped out on the graphene sheet in figure 6 a and the tube itself is schematically shown in 6 b. The underlying symmetry is the D_{6h} group, but when the graphene sheet is rolled up as a tubule a new rotational symmetry of 180° around the center of a C-C bond, U, is invoked. The U symmetry changes every $\hat{z}$ coordinate to $-\hat{z}$ and leaves the lattice unchanged, and for all tube types the U symmetry applies [Bar06]. For armchair and zigzag tubes additional symmetries are present due to mirror planes and screw rotations.

The reciprocal lattice vectors associated with the translational and chiral vectors are found by applying periodic boundary conditions and are given by,

$$\vec{K}_1 = \frac{1}{N}\left[\left(\frac{2n+m}{d_R}\right)\vec{b}_1 + \left(\frac{2m+n}{d_R}\right)\vec{b}_2\right] \text{ and } \vec{K}_2 = \frac{1}{N}\left[m\vec{b}_1 - n\vec{b}_2\right], \tag{11}$$

respectively, where N is the number hexagons per unit cell given by,

$$N = \frac{2\left(n^2 + m^2 + nm\right)}{d_R}. \tag{12}$$

Wavevectors associated with the circumference of the tube are quantized and lead to $2N$ cuts in the plane associated with each of the $2N$ carbon atoms for a particular (n,m) index. The line segment of length $2\pi/T$ defines the FBZ, and each of the N line segments is associated with an angular momentum μ. Furthermore, the reciprocal lattice of chiral SWNT cut through the Dirac cones of K and K′ points at equivalent distances leading to double degeneracies, Fig 6.b.

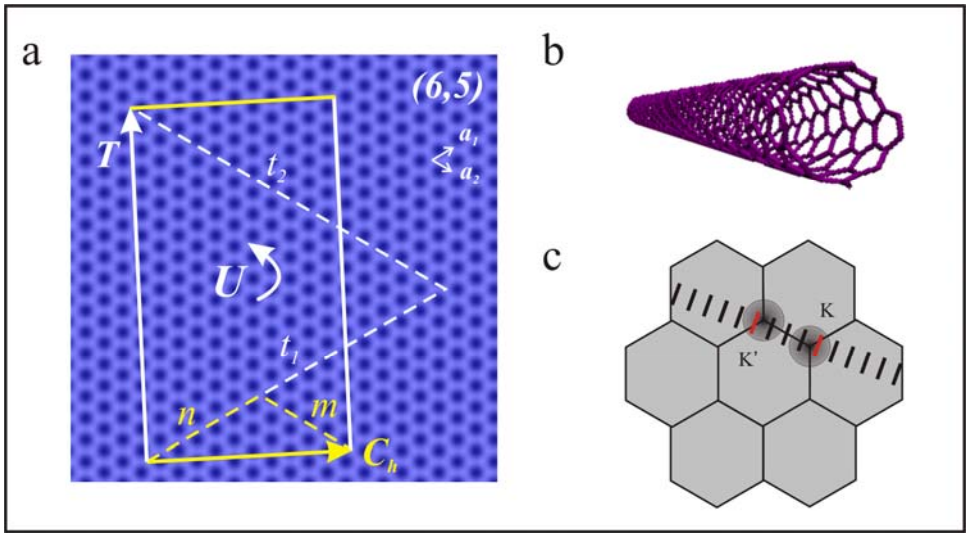

Figure 6.a. Unit cell of the $(6,5)$ tube with the rotational symmetry axis U. **b.** Ball and stick model of the (6,5) tube. **c.** Schematic of the first Brillouin zone, in red, of a chiral SWNT which cuts through the Dirac cone of graphene near the K and the K' points.

This tight binding model of graphene can be used to illustrate the geometrical dependence on the electronic structure of SWNT. The band structure is found by replacing $\vec{k}$ in eq. 8 with,

$$\vec{k} = k\frac{\vec{K}_2}{|\vec{K}_2|} + \mu\vec{K}_1 \ , \tag{13}$$

where $-\pi/T \le k \le \pi/T$ and $\mu = 0...N-1$. The DOS and band structure for the first few electronic states are given in Fig. 7 a and 7 b for the (7,4) metallic SWNT and (6,5) semiconducting SWNT. The DOS contains Van Hove singularities (VHS) [Van53] associated with the parabolic bands made by cutting through the Dirac cones associate with the graphene sheet.

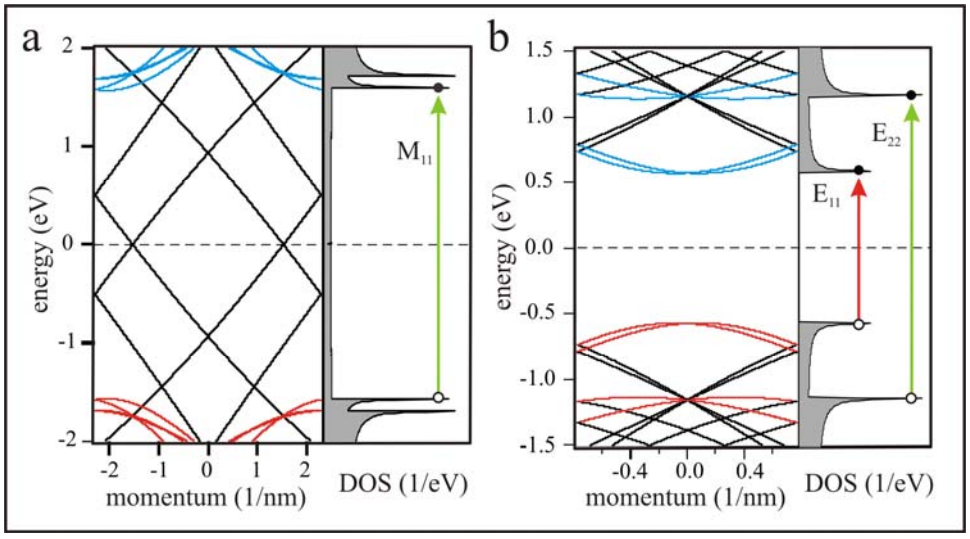

Figure 7. Tight binding band structure and density of states (DOS) of the **a.** (7,4) and **b.** (6,5) tubes. The colored bands are responsible for the singularities in the DOS, and the gray bands are responsible for the continuum of states. For light polarized parallel to the tube axis, excitations from the conduction band to the valence band in semiconductors are labeled E_{ii} and in metallic tube M_{ii}.

The hopping integral is taken as the value from graphene, $t = -3.033eV$, and the overlap integral is set as $s = 0$ for historical reasons [Sai92]. Electronic states at these energies are molecular-like and discrete due to quantum confinement around the circumference, while others not at the VHS are associated with the continuum along the tube axis. Excitations from a VHS in the i^{th} conduction band to the i^{th} valence band in metallic tubes are designated by M_{ii} and in semiconductors by E_{ii}.

The real part of the tight binding wavefunctions for the doubly degenerate (6,5) E_{11} electrons and holes at the K and K′ points is plotted in Fig. 8. U symmetry operations on the wavefunctions the spatial coordinate (0,0) transform the wavefunctions as a doublet ${}_{k}E_{\mu}$ and ${}_{-k}E_{\mu}$, and the wavefunction at $k = 0$ as a singlet where one state is symmetric ${}_{0}A_{0}^{+}$ and the other antisymmetric ${}_{0}A_{0}^{-}$ [Dam99]. The symmetric state ${}_{0}A_{0}^{+}$ is not optically active in the dipole approximation while ${}_{k}E_{\mu}$, ${}_{-k}E_{\mu}$, and ${}_{0}A_{0}^{-}$ are [Vuk02]. In the limit that the electrons and holes interact the aforementioned symmetries become important in ordering excitonic states and determine their optical activity.

The empirical model presented above neglects the effect of the electron-electron interaction which alters the band structure, and electron-hole interaction which leads to the formation of excitons [Ich99, Rho00]. State of the art calculations treat corrections to electron-electron interaction as a perturbation from density functional theory, which underestimates the band gap, and use the full dielectric function within the random phase approximation to calculate the electron self energy within the *GW* approximation [Spa04, Cha04]. The correction leads to an opening of the free particle band gap due to exchange and correlation effects and is the most accurate model to date, Fig. 9. The electron-hole interaction is treated by solving the Bethe-Salpeter equation (BSE), which is used to

calculate the excitation energy Ω_S and exciton amplitudes, A_{vc}^S, between valence (v) band electrons and conduction (c) band holes under the influence of the Coulomb interaction [Spa05]. The imaginary part of the dielectric function is then calculated similarly to the absorption coefficient in equation 5, where the oscillator strength is now determined by the matrix element $\left|A_{vc}^S \langle c|H'|v\rangle\right|^2$.

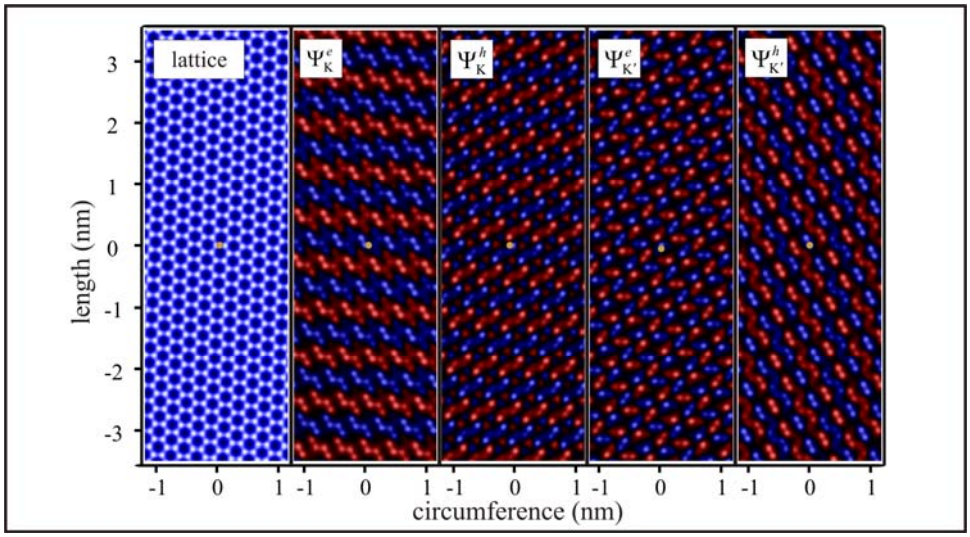

Figure 8. Real space lattice and the E_{11} tight binding wave functions for the (6,5) tube at the K and K′ points. The wavefunctions transform as a doublet labeled by the1-D point group notation ${}_k E_\mu$, where the K / K′ electrons are symmetric/ antisymmetric and the K / K′ holes are antisymmetric/symmetric with respect to U symmetry.

In principle one could then calculate the excitonic contributions and the free particle contributions to the imaginary part of the dielectric function by considering the OS and DOS with and without the e-h interaction, Fig. 9. Due to the reduced screening in one-dimension almost all of the OS is transferred to strongly bound excitons and there is very little absorption from the continuum [And97]. Binding energies of excitons in semiconducting SWNT have been predicted and measured experimentally and range

from 0.3-1.0 eV [Mau05, Wan06, Per04]. Interestingly excitons are also predicted to be important in metallic SWNT although the binding energy is significantly less [Des07].

The energetic ordering of the fine structure of the excitonic states is determined by the Coulomb interaction and the symmetry of the wavefunctions [And06]. The degeneracy of the free particle states in figure 8 is lifted by the Coulomb interaction due to intravalley and intervalley, K and K′, mixing. Intervalley interactions mix electrons from K with holes from K′ and vice versa and lead to states with zero center of mass momentum that transform under the U rotation as singlets, ${}_0A_0^+$ and ${}_0A_0^-$, similarly to their free particle counterparts. The wavefunctions of these states are given by symmetric and antisymmetric combinations of electron-hole wavefunctions such that,

$$ {}_0A_0^+ \rightarrow \left|\mathrm{KK}'\right\rangle - \left|\mathrm{K}'\mathrm{K}\right\rangle \text{ and } {}_0A_0^- \rightarrow \left|\mathrm{KK}'\right\rangle + \left|\mathrm{K}'\mathrm{K}\right\rangle . \tag{14} $$

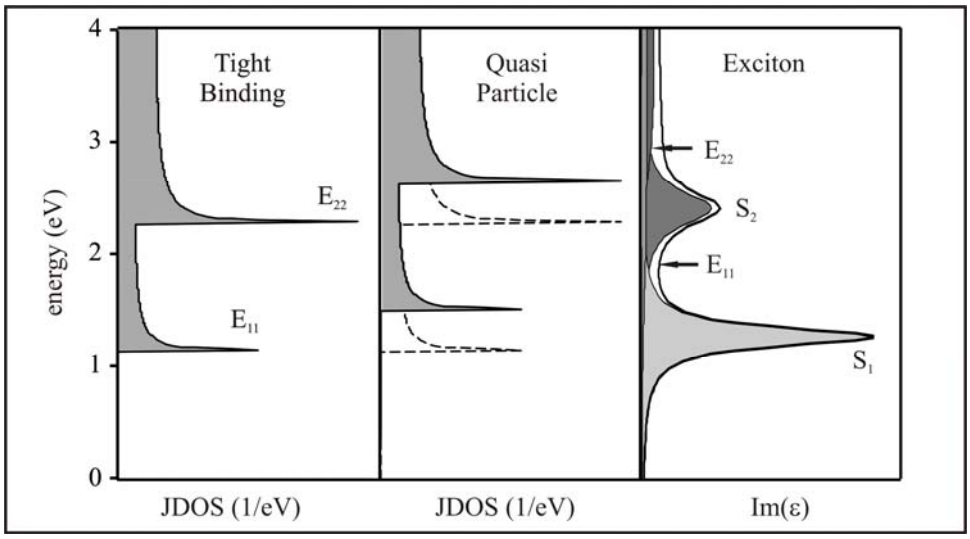

Figure 9. The joint density of states (JDOS) of the (6,5) tube in the tight binding picture, schematic of the JDOS in the quasi-particle picture, and schematic of the imaginary part of the dielectric function within the exciton picture. The oscillator strength is transferred to the excitons and there is very little e-h continuum.

The probability to find the electron with a fixed hole position at (0,0) and the circumferentially averaged electron density relative to the hole position is plotted for both cases in figures 10 a and b respectively. The optically inactivity of ${}_0A_0^+$ state is evident from the low electron density relative to the hole compared to the ${}_0A_0^-$ state. This comes from the presence of a node in the envelope of the exciton wavefunction for the ${}_0A_0^+$ state [Jia07]. Intravalley interactions bind electrons and holes within respective K and K′ valleys and lead to a set of excitons that transform as a doublet under the U rotation, ${}_kE_\mu$ and ${}_{-k}E_\mu$, just as their single-particle constituents. These states are also optically inactive due to relatively large momentum needed for excitation, but are allowed in phonon-assisted processes [Per05, Ple05].

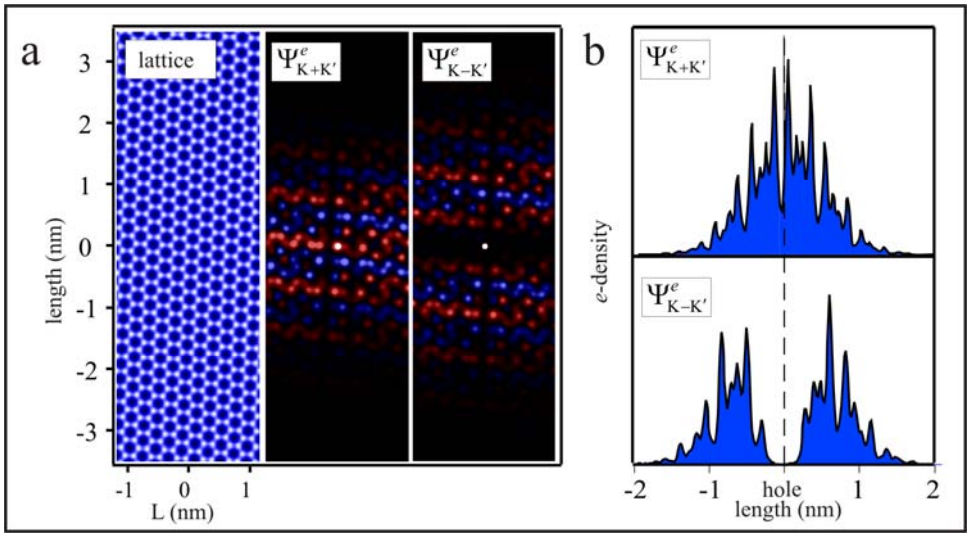

Figure 10. a. The lowest lying E_{11} exciton wavefunctions (electron wavefunctions with hole fixed at 0,0 and a *ad hoc* Gaussian envelope of 1.5 nm) for the (6,5) tube. **b.** The electron density averaged over the circumference for a fixed hole position at (0,0) of the two lowest exciton states. The symmetric combination of K and K' lead to a maximum electron density at the hole, and the asymmetric combination lead to a minimum electron density at the hole.

When spin multiplicity is considered, there is a sixteen fold degeneracy due to the four spatial combinations of e-h wavefunctions and the four possibilities of spin configuration. The energetic ordering of the possible sixteen states is shown in figure 11, and the lowest state in the singlet manifold is the ${}_0A_0^+$ state [Zha04, And06, Cap06]. The next highest is the dipole allowed state and is highlighted where transitions can take place due to the dispersion of light. The splitting of these two states is on the order of a few meV and at room temperature both are believed to be in thermal equilibrium [Mor07, Ber07] .

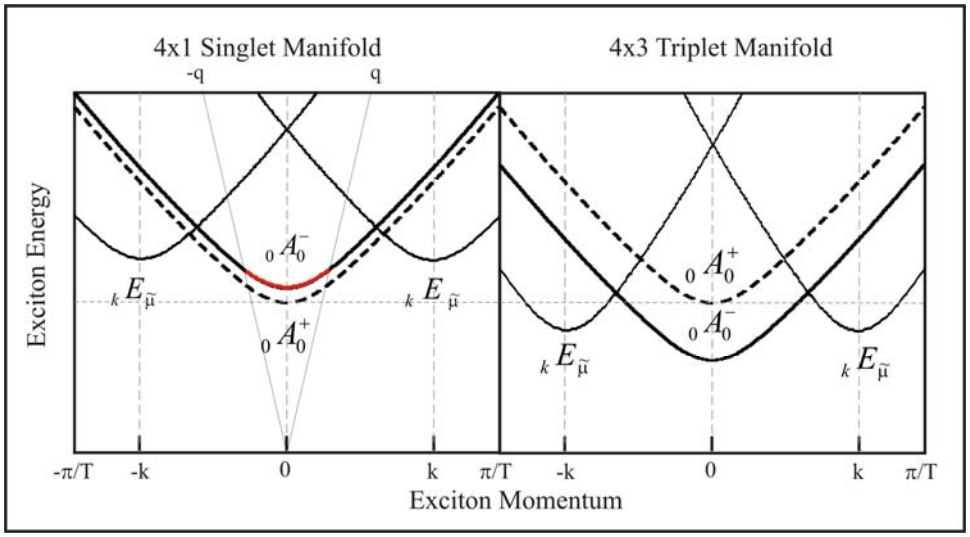

Figure 11. The 4x4 valley degeneracy of the electron and hole bands at the K and the K' points is lifted by the electron/hole interaction and becomes a 4x1 singlet exciton manifold and a 4x3 triplet manifold. The only dipole-allowed state is in the singlet manifold and is odd with respect to *U* symmetry. A degeneracy between singlet and triplet states that are even with respect to *U* symmetry is shown.

In the case of the triplets, the exchange interaction vanishes and the ordering is purely due to the direct part of the Coulomb interaction, and it turns out there is an accidental degeneracy with the lowest singlet exciton and its triplet counterpart [Cap06].

Additionally, the singlet-triplet splitting for the bright excitons has a $1/d^2$ dependence and for the (6,5) tube is on the order of 70 meV [Cap07]. Degeneracies such as these have been predicted in conjugated polymers [Abe92], and could effect relaxation of excitons in SWNT through efficient intersystem crossing. In theory each E_{ii} transition should contain the singlet and triplet states mentioned above, but the transfer of oscillator strength from the continuum of e-h pairs to the excitons may become less for higher energy states and excitonic effects may become negligible.

C. Relaxation Mechanisms of Photoexcitations

1. Internal Conversions in Aromatics

Internal conversions transfer energetically higher lying electronic or excitonic states into energetically lower lying electronic or excitonic states of the same spin multiplicity by a microscopic scattering mechanism. The three electronic structures discussed in the previous section included the extremes of aromaticity as found in, benzene and graphene, and as an intermediate case of SWNT. Knowledge of the relaxation mechanism of the extrema can give insight to processes that may occur in nanotubes. In the case of benzene the electronic excitations are coupled strongly to the vibrational degrees of freedom and relaxation takes place through very efficient internal conversions [Hen71]. Graphene, on the other hand, has not been studied experimentally by optics in its single-layer form until recently [Bla07, Yan07]. Ultrafast optical experiments on high-quality samples of graphite have provided clues to the peculiar

nature of graphene and its linear dispersion relation, but this has yet to be done on single layer graphene. Yet, Raman spectroscopy of optical phonons in metallic SWNT reveal peculiarities in the screening of the ion-ion interaction near the zone boundary and are interpreted as effects from the well-know, Kohn anomaly [Pis07]. This effect explains the difference between Raman spectra of semiconducting and metallic SWNTs, and gives clues that graphene should behave the same way and that excitations to the dipole allowed electronic states relax to electronic states that are coupled strongly to the lattice by "softened" phonon modes.

It can be expected, as in the case in benzene that in isolated excited semiconducting SWNT will undergo molecular like internal conversions by phonon scattering. Conversely, the continuum of states that do not contribute to the formation of excitons may also provide an efficient scattering mechanism for internal conversion. Until recently the photoluminescence quantum yields have only been reported to be around 0.1%, and most of the energy must be dissipated through nonradiative decay channels as in benzene that has a quantum yield of 0.5% [O'Co00]. There is no evidence for strong vibrational coupling as in benzene in the optical spectra of SWNT, but the peculiar nature of one dimension excitations may hide these effects. As long as energy and momentum is conserved the mechanism of internal conversion may take on both molecular and bulk like characteristics in SWNTs. If both processes compete with each other than the branching ratio between the two is of interest to account for low observed photoluminescence quantum yields.

2. Intersystem Crossing in Aromatics

Intersystem crossing processes transfer energetically higher lying electronic or excitonic states into energetically lower lying or energetically equivalent states of different spin multiplicity. In order to flip a spin that changes the multiplicity of the excitation, the product of the square of the spin orbit interaction and the final density of states must be non-negligible. Intrinsic spin orbit interaction in atomic carbon is on the order of 6 meV or ≈ 70 °K and estimated in isolated benzene to be approximately 0.1 meV or ≈ 1 °K [Min06]. Due to strong electron-phonon coupling, intersystem crossings can overcome internal conversions by mixing π and σ states in benzene [Hen71]. The Franck-Condon factors are extremely important in these processes and determine not only the oscillator strengths of the optical transitions, but also the efficiency of intersystem crossing mechanisms. Despite the small spin-orbit interaction, triplets efficiently quench the fluorescence of benzene and can account for the observed low quantum yield [Daw86]. In SWNT the notion of Franck-Condon factors being important in optical transitions has not been reported, but in transport measurements this interpretation has been used to explain phonon assisted tunneling between electronic states [Sap06].

In graphene it has been estimated that the intrinsic spin orbit coupling is on the order of 1 μeV or ≈ 10 mK and may arise from the local curvature of the topologically imperfect sheet that mixes π and σ orbitals [Min06]. The mixing of π and σ orbitals may be even stronger in small diameter SWNTs and spin orbit interactions of approximately 0.1 meV or ≈ 1 °K have been predicted which is similar to Benzene [Hue06]. Moreover,

the degeneracy of the lowest lying singlet exciton and its triplet counterpart along with the one dimensionality of the Coulomb interaction would lead to a large density of states for the singlets to scatter into even though the spin-orbit interaction is rather small. Therefore, even though the Condon factors may not play a significant role in nanotubes the extremely large density of states may compensate and allow for an efficient decay channel fro singlet excitons. By determining the non-radiative lifetime of the lowest lying singlet state a good estimate of the spin-orbit interaction should be accessible.

3. Electron and Exciton Energy Transfer

When synthesized, SWNT form large crystallites due to relatively strong van der Waals interactions [Ter94]. The crystallites consist of statistical mixtures of semiconducting and metallic tubes that do not fluorescence. Intertube relaxation pathways may be very important and dominate intratube processes in crystallites. The mechanism involved are not very clear, but theoretical speculations of intertube tunneling and delocalization have been reported with out any clear evidence from experiment [Kwo98, Maa00, Sta00]. In aggregates of molecules and quantum dots, exciton energy transfer can take place depending on the physical distance and spectral overlaps of acceptors and donors [Pow75, Kag96]. Also, electron transfer can lead to ionized states that have a different ground state due to the gain of an extra electron or hole and become dark states or charge transfer excitons.

If energy transfer resulted in emission from a smaller band gap tube it is most likely that the donor singlet state and acceptor singlet state are coupled though a dipolar

field. In the case of non-radiative energy transfer with significant donor emission and acceptor absorption spectral overlap and the interactions between the donor acceptor is relatively week Förster type exciton energy is most likely involved [Vol04]. Typical separations between acceptor and donor exceed 1 nm and the transfer rate follows the well known R^{-6} dependence. Conversely, if the interaction between acceptor and donor are relatively strong and the interspacing is approximately 1 nm or less wavefunction overlap becomes a critical component of the transfer mechanism and the exchange interaction must be taken into account [Dex53]. Energy transfer in this regime is considered to be Dexter transfer and the rate decreases exponentially as the interspacing is increased. Moreover, since the exchange interaction becomes important in this regime, this is the dominant mechanism for triplet-triplet exciton energy transfer and may or may not lead to emissive states. In essence this is an electron or hole exchange mechanism and can be classified as an ultrafast electron transfer mechanism. [Vol04]. In nanotubes the intertube spacing is on the order of 3 Å and the tubes are bound by approximately 500 meV per micron of tube contact. Therefore, the relative strength of the interaction between tubes can be tested if exciton energy transfer is found to be either Förster or Dexter in nature.

D. References

[Abe92] Abe, S., J. Yu, et al. (1992). "Singlet and triplet excitons in conjugated polymers." Physical Review B **45**(15): 8264 LP - 8271.

[Ada03] Adams, D. M., L. Brus, et al. (2003). "Charge transfer on the nanoscale: Current status." Journal of Physical Chemistry B **107**(28): 6668-6697.

[And97] Ando, T. (1997). "Excitons in carbon nanotubes." Journal of the Physical Society of Japan **66**(4): 1066-1073.

[And04] Ando, T. (2004). "Excitons in carbon nanotubes revisited: Dependence on diameter, Aharonov-Bohm flux, and strain." Journal of the Physical Society of Japan **73**(12): 3351-3363.

[And05] Ando, T. (2005). "Theory of electronic states and transport in carbon nanotubes." Journal of the Physical Society of Japan **74**(3): 777-817.

[And06] Ando, T. (2006). "Effects of valley mixing and exchange on excitons in carbon nanotubes with Aharonov-Bohm flux." Journal of the Physical Society of Japan **75**(2).

[Bac02] Bachilo, S. M., M. S. Strano, et al. (2002). "Structure-assigned optical spectra of single-walled carbon nanotubes." Science **298**(5602): 2361-2366.

[Bar06] Barros, E. B., A. Jorio, et al. (2006). "Review on the symmetry-related properties of carbon nanotubes." Physics Reports-Review Section of Physics Letters **431**(6): 261-302.

[Ber07] Berger, S., C. Voisin, et al. (2007). "Temperature dependence of exciton recombination in semiconducting single-wall carbon nanotubes." Nano Letters **7**(2): 398-402.

[Bla07] Blake, P., E. W. Hill, et al. (2007). "Making graphene visible." Applied Physics Letters **91**(6).

[Cap06] Capaz, R. B., C. D. Spataru, et al. (2006). "Diameter and chirality dependence of exciton properties in carbon nanotubes." Physical Review B **74**(12).

[Cap07] Capaz, R. B., C. D. Spataru, et al. (2007). "Excitons in Carbon Nanotubes: Diameter and Chirality Trends." Physica Status Solidi B **244**, 4016-4020.

[Cha04] Chang, E., G. Bussi, et al. (2004). "Excitons in carbon nanotubes: An ab initio symmetry-based approach." Physical Review Letters **92**(19).

[Coo86] Cooper, D. L., J. Gerratt, et al. (1986). "The Electronic-Structure of the Benzene Molecule." Nature **323**(6090): 699-701.

[Con26] Condon, E. (1926). "A Theory of Intensity Distribution in Band Systems." Physical Review **28**(6): 1182 LP - 1201.

[Dam99] Damnjanović, M., I. Milošović‡, et al. (1999). "Full symmetry, optical activity, and potentials of single-wall and multiwall nanotubes." Physical Review B **60**(4): 2728 LP - 2739.

[Daw86] Dawson, W. R. and M. W. Windsor (1968). "Fluorescence Yields of Aromatic Compounds." Journal of Physical Chemistry **72**(9): 3251-&.

[Des07] Deslippe, J., C. D. Spataru, et al. (2007). "Bound excitons in metallic single-walled carbon nanotubes." Nano Letters **7**(6): 1626-1630.

[Dex53] Dexter, D. L., (1953). "A Theory of Sensitized Luminescence in Solids." The Journal of Chemical Physics . 21(5): 836-850.

[Duk05] Dukovic, G., F. Wang, et al. (2005). "Structural dependence of excitonic optical transitions and band-gap energies in carbon nanotubes." Nano Letters **5**(11): 2314-2318.

[Fer06] Ferrari, A. C., J. C. Meyer, et al. (2006). "Raman spectrum of graphene and graphene layers." Physical Review Letters **97**(18).

[Fren00] Frenking, G. (2000). "Perspective on "Quantentheoretische beitrage zum benzolproblem. I. Die elektronenkonfiguration des benzols und verwandter beziehungen" - Huckel E (1931) Z Phys 70 : 204-286." Theoretical Chemistry Accounts **103**(3-4): 187-189.

[Ham92] Hamada, N., S. Sawada, et al. (1992). "New One-Dimensional Conductors - Graphitic Microtubules." Physical Review Letters **68**(10): 1579-1581.

[Hay74] Hay, P. J. and I. Shavitt (1974). "Ab-Initio Configuration Interaction Studies of Pi-Electron States of Benzene." Journal of Chemical Physics **60**(7): 2865-2877.

[Hen71] Henry, B. R. and W. Siebrand (1971). "Spin-Orbit Coupling in Aromatic Hydrocarbons - Analysis of Nonradiative Transitions between Singlet and Triplet States in Benzene and Naphthalene." Journal of Chemical Physics **54**(3): 1072.

[Hue06] Huertas-Hernando, D., F. Guinea, et al. (2006). "Spin-orbit coupling in curved graphene, fullerenes, nanotubes, and nanotube caps." Physical Review B **74**(15).

[Min06] Min, H., J. E. Hill, et al. (2006). "Intrinsic and Rashba spin-orbit interactions in graphene sheets." Physical Review B **74**(16).

[Ich99] Ichida, M., S. Mizuno, et al. (1999). "Exciton effects of optical transitions in single-wall carbon nanotubes." Journal of the Physical Society of Japan **68**(10): 3131-3133.

[Ina72] Inagaki, T. (1972). "Absorption-Spectra of Pure Liquid Benzene in Ultraviolet Region." Journal of Chemical Physics **57**(6): 2526.

[Jia07] Jiang, J., R. Saito, et al. (2007). "Chirality dependence of exciton effects in single-wall carbon nanotubes: Tight-binding model." Physical Review B **75**(3).

[Kag96] Kagan, C. R., C. B. Murray, et al. (1996). "Long-range resonance transfer of electronic excitations in close-packed CdSe quantum-dot solids." Physical Review B **54**(12): 8633-8643.

[Ker05] Kertesz, M., C. H. Choi, et al. (2005). "Conjugated polymers and aromaticity." Chemical Reviews **105**(10): 3448-3481.

[Kwo98] Kwon, Y. K., S. Saito, et al. (1998). "Effect of intertube coupling on the electronic structure of carbon nanotube ropes." Physical Review B **58**(20): 13314-13317.

[Maa00] Maarouf, A. A., C. L. Kane, et al. (2000). "Electronic structure of carbon nanotube ropes." Physical Review B **61**(16): 11156-11165.

[Mau05] Maultzsch, J., R. Pomraenke, et al. (2005). "Exciton binding energies in carbon nanotubes from two-photon photoluminescence." Physical Review B **72**(24).

[Min95] Mintmire, J. W. and C. T. White (1995). "Electronic and Structural-Properties of Carbon Nanotubes." Carbon **33**(7): 893-902.

[Moo01] Moos, G., C. Gahl, et al. (2001). "Anisotropy of quasiparticle lifetimes and the role of disorder in graphite from ultrafast time-resolved photoemission spectroscopy." Physical Review Letters **87**(26).

[Mor07] Mortimer, I. B. and R. J. Nicholas (2007). "Role of bright and dark excitons in the temperature-dependent photoluminescence of carbon nanotubes." Physical Review Letters **98**(2).

[Nov05] Novoselov, K. S., A. K. Geim, et al. (2005). "Two-dimensional gas of massless Dirac fermions in graphene." Nature **438**(7065): 197-200.

[O'Co02] O'Connell, M. J., S. M. Bachilo, et al. (2002). "Band gap fluorescence from individual single-walled carbon nanotubes." Science **297**(5581): 593-596.

[Pai70] Painter, G. S. and D. E. Ellis (1970). "Electronic Band Structure and Optical Properties of Graphite from a Variational Approach." Physical Review B **1**(12): 4747-&.

[Per04] Perebeinos, V., J. Tersoff, et al. (2004). "Scaling of excitons in carbon nanotubes." Physical Review Letters **92**(25).

[Per05] Perebeinos, V., J. Tersoff, et al. (2005). "Effect of exciton-phonon coupling in the calculated optical absorption of carbon nanotubes." Physical Review Letters **94**(2).

[Ple05] Plentz, F., H. B. Ribeiro, et al. (2005). "Direct experimental evidence of exciton-phonon bound states in carbon nanotubes." Physical Review Letters **95**(24).

[Pis07] Piscanec, S., M. Lazzeri, et al. (2007). "Optical phonons in carbon nanotubes: Kohn anomalies, Peierls distortions, and dynamic effects." Physical Review B **75**(3).

[Pow75] Powell, R. C. and Z. G. Soos (1975). "Singlet Exciton Energy-Transfer in Organic Solids." Journal of Luminescence **11**(1-2): 1-45.

[Roh00] Rohlfing, M. and S. G. Louie (2000). "Electron-hole excitations and optical spectra from first principles." Physical Review B **62**(8): 4927-4944.

[Roo92] Roos, B. O., K. Andersson, et al. (1992). "Towards an Accurate Molecular-Orbital Theory for Excited-States - the Benzene Molecule." Chemical Physics Letters **192**(1): 5-13.

[Sai92] Saito, R., M. Fujita, et al. (1992). "Electronic-Structure of Graphene Tubules Based on C-60." Physical Review B **46**(3): 1804-1811.

[Sai93] Saito, Y., T. Yoshikawa, et al. (1993). "Interlayer Spacings in Carbon Nanotubes." Physical Review B **48**(3): 1907-1909.

[Sap06] Sapmaz, S., P. Jarillo-Herrero, et al. (2006). "Tunneling in suspended carbon nanotubes assisted by longitudinal phonons." Physical Review Letters **96**(2).

[Sch01] Schleyer, P. V. (2001). "Introduction: Aromaticity." Chemical Reviews **101**(5): 1115-1117.

[Sei90] Seibert, K., G. C. Cho, et al. (1990). "Femtosecond Carrier Dynamics in Graphite." Physical Review B **42**(5): 2842-2851.

[Spa04] Spataru, C. D., S. Ismail-Beigi, et al. (2004). "Excitonic effects and optical spectra of single-walled carbon nanotubes." Physical Review Letters **92**(7).

[Spa05] Spataru, C. D., S. Ismail-Beigi, et al. (2005). "Theory and ab initio calculation of radiative lifetime of excitons in semiconducting carbon nanotubes." Physical Review Letters **95**(24).

[Sta00] Stahl, H., J. Appenzeller, et al. (2000). "Intertube coupling in ropes of single-wall carbon nanotubes." Physical Review Letters **85**(24): 5186-5189.

[Tan92] Tanaka, K., K. Okahara, et al. (1992). "Electronic-Properties of Bucky-Tube Model." Chemical Physics Letters **191**(5): 469-472.

[Tat82] Tatar, R. C. and S. Rabii (1982). "Electronic-Properties of Graphite - a Unified Theoretical-Study." Physical Review B **25**(6): 4126-4141.

[Ter94] Tersoff, J. and R. S. Ruoff (1994). "Structural-Properties of a Carbon-Nanotube Crystal." Physical Review Letters **73**(5): 676-679.

[Van53] Van Hove, L. (1953). "The Occurrence of Singularities in the Elastic Frequency Distribution of a Crystal." Physical Review **89**(6): 1189 LP - 1193.

[Vol04] Volkhard, M. and O. Kuhn (2004). "Charge and Energy Transfer Dynamics in Molecular Systems." Wiley-VCH.

[Vuk02] Vukovic, T., I. Milosevic, et al. (2002). "Carbon nanotubes band assignation, topology, Bloch states, and selection rules." Physical Review B **65**(4).

[Wal47] Wallace, P. R. (1947). "The Band Theory of Graphite." Physical Review **71**(9): 622 LP - 634.

[Wan05] Wang, F., G. Dukovic, et al. (2005). "The optical resonances in carbon nanotubes arise from excitons." Science **308**(5723): 838-841.

[Wan06] Wang, Z. J., H. Pedrosa, et al. (2006). "Determination of the exciton binding energy in single-walled carbon nanotubes." Physical Review Letters **96**(4).

[Wil65] Wilcox, D. H. and Greenbau.Fr (1965). "Kekules Benzene Ring Theory - a Subject for Lighthearted Banter." Journal of Chemical Education **42**(5): 266-&.

[Xu96] Xu, S., J. Cao, et al. (1996). "Energy dependence of electron lifetime in graphite observed with femtosecond photoemission spectroscopy." Physical Review Letters **76**(3): 483-486.

[Yar01] Yarkony, D. R. (2001). "Conical intersections: The new conventional wisdom." Journal of Physical Chemistry A **105**(26): 6277-6293.

[Yan07] Yan, J., Y. B. Zhang, et al. (2007). "Raman scattering and tunable electron-phonon coupling in single layer graphene." Solid State Communications **143**(1-2): 39-43.

[Zha04] Zhao, H. B. and S. Mazumdar (2004). "Electron-electron interaction effects on the optical excitations of semiconducting single-walled carbon nanotubes." Physical Review Letters **93**(15).

CHAPTER II

EXPERIMENTAL TECHNIQUES USED TO INVESTIGATE CHARGE AND ENERGY TRANSFER

The experimental techniques used to investigate charge carrier dynamics in single-wall carbon nanotubes in this dissertation are presented. Instrument details are explained along with theoretical considerations in experimental analysis. Linear spectroscopic techniques including ground state absorption and photoluminescence excitation are overviewed in terms their application to carbon nanotube analysis. Dynamical studies are carried out using ultrafast pump-probe spectroscopy and provide information on ground state recovery as well as excited state lifetimes.

A. Ground State Absorption Spectroscopy and Dephasing

Absorption spectra are acquired using the Varian Cary 5000, which an accessible wavelength range from 175-3300 nm. Absorption spectra recorded with this instrument simply reflect the wavelength λ dependence of the absorbance $A(\lambda)$. Note, that the term optical density $OD(\lambda)$ is often used synonymously for absorbance. According to the Beer-Lambert law the absorbance is defined as $A(\lambda)=\alpha(\lambda)lC$, where α is the absorption coefficient defined in chapter 1, l is the optical path length, and C is the concentration of the absorbing species. In order to obtain the optical density $OD(\lambda)$ of a

sample, one measures the intensity of the light transmitted sample through the sample, $I_s(\lambda)$, and the intensity of the incident light, $I_0(\lambda)$. Then by using the relation,

$$OD(\lambda) = \log\left(\frac{I_0(\lambda)}{I_S(\lambda)}\right), \tag{1}$$

the optical density of the sample is found. If the material of interest is dissolved in solution then a reference spectrum of the solvent must be taken and its absorbance be subtracted from the solution spectrum.

A discussion focused on a simple two-level model under the dipole approximation is instructive to explain the concept of the absorption of electromagnetic radiation and emission from a bound entity such as an exciton. The system is described by a ground state, $|S_0\rangle$, and an excited state given by, $|S_1\rangle$, where as in chapter 1 these are singlet states. The excited state is dipole coupled to the ground state and the quantum yield of fluorescence is unity. Following the formalism outlined by Loudon [1983], a time-dependent electromagnetic field with a frequency ω, $\vec{E}_\omega(t)$ will induce a polarization on an ensemble of systems such that,

$$\vec{P}_\omega(t) = 1/2\,\varepsilon_0 \vec{E}_0\left\{\chi(\omega)e^{-i\omega t} + \chi(-\omega)e^{i\omega t}\right\}, \tag{2}$$

where ε_0 is the permittivity of free space, $\vec{E}_0$ is the field strength, and $\chi(\omega)$ is the frequency depended susceptibility which is related to the absorption coefficient by $\alpha(\omega) = [\omega/cn(\omega)]\mathrm{Im}\,\chi(\omega)$ [Lou83]. Here the index of refraction, $n(\omega)$, is usually assumed to vary slowly with ω and can be treated as a constant. The time dependent polarization determines the susceptibility and the dynamics of the system determine the time dependent dipole moment $\vec{d}$ which is proportional to the time dependent

polarization. The dynamics of the system are governed by the optical Bloch equations [Lou83]. Including radiative γ and environmental damping γ_{env}, an incident electromagnetic field $\vec{E}_0$ with a frequency ω, the Bloch equations are given by,

$$\begin{aligned} \frac{d\rho_{11}}{dt} &= -\frac{1}{2}i\zeta * e^{i(\omega_{01}-\omega)t}\rho_{01} + \frac{1}{2}i\zeta e^{-i(\omega_{01}-\omega)t}\rho_{10} - 2\gamma\rho_{11} \\ \frac{d\rho_{01}}{dt} &= \frac{1}{2}i\zeta e^{-i(\omega_{01}-\omega)t}(\rho_{00}-\rho_{11}) + [i(\omega_{01}-\omega)-\gamma']\rho_{01} \end{aligned}, \qquad (3)$$

where ρ_{11} is the population in $|S_1\rangle$, ρ_{01} is the coherence between $|S_1\rangle$ and $|S_0\rangle$, $\hbar\omega_{01}$ is the transition energy between from $|S_0\rangle$ and $|S_1\rangle$, $\zeta = \frac{e}{\hbar}\langle S_0|\vec{E}_0\cdot\vec{d}|S_1\rangle$ is the dimensionless transition dipole moment, and $\gamma' = \gamma + \gamma_{env}$ is the dephasing rate.

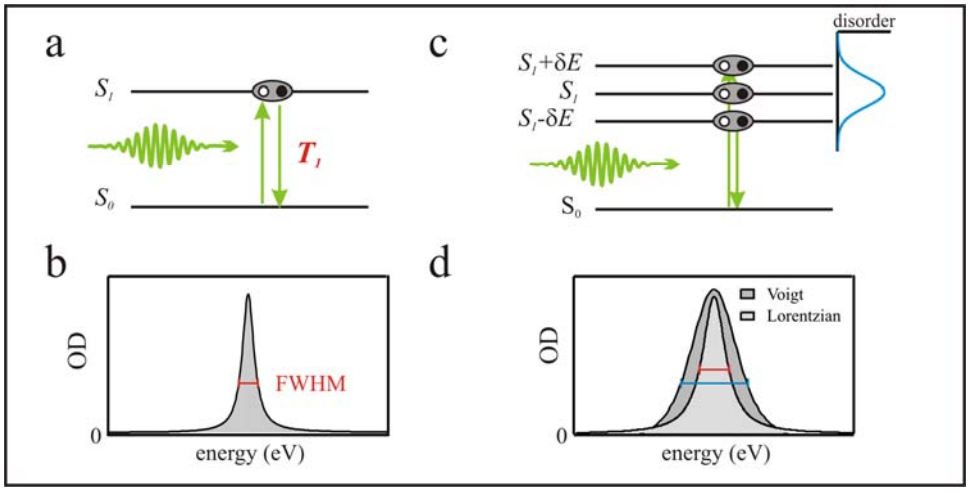

Figure 1 a. Schematic of a two level system absorbing a photon, which takes the system from the ground state (S_0) to an excited state (S_1). **b.** Absorption spectra of the hypothetical system in a**.** If the system is ideal, the only broadening would be due to the finite lifetime of the photoexcitation and this would be reflected in the full width half maximum of a Lorentzian profile. Such a system is said to be homogeneously broadened. **c.** The same two level system under the presence of static disorder that smears out the discrete energy level S_0 by a Gaussian of width 2δE. **d.** The effect of the disorder is said to inhomogeneously broaden the spectra and the resulting absorption spectra is a convolution of both a Lorentzian and Gaussian profile which is called a Voigt profile.

The dephasing rate determines the time over in which the polarization decays. If the system is initially in its ground state $|S_0\rangle$, $\rho_{11}(0)=0$ and $\rho_{01}(0)=0$, then the solutions to equations 3 to the lowest order in $|\zeta|$ are,

$$\begin{aligned}\rho_{11} &= \frac{1}{4}|\zeta|^2\left\{C_1 + C_2 e^{-2\gamma t} - C_3\cos[(\omega_{01}-\omega)t] - C_4\sin[(\omega_{01}-\omega)t]\right\}e^{-\gamma t} \\ \rho_{01} &= \frac{i\zeta}{2i(\omega_{01}-\omega)-\gamma'}\left\{e^{-\gamma t} - e^{-i(\omega_{01}-\omega)t}\right\}\end{aligned}, \qquad (4)$$

where,

$$C_1 = \frac{\gamma'/\gamma}{(\omega_{01}-\omega)^2+(\gamma')^2}, C_2 = \frac{(2\gamma-\gamma')/\gamma}{(\omega_{01}-\omega)^2+(2\gamma-\gamma')^2},$$
$$C_3 = \frac{2\left[(\omega_{01}-\omega)^2+\gamma'(2\gamma-\gamma')\right]}{\left[(\omega_{01}-\omega)^2+(\gamma')^2\right]\left[(\omega_{01}-\omega)^2+(2\gamma-\gamma')^2\right]}, \text{ and}$$
$$C_4 = \frac{4\left[(\omega_{01}-\omega)(\gamma'-\gamma)\right]}{\left[(\omega_{01}-\omega)^2+(\gamma')^2\right]\left[(\omega_{01}-\omega)^2+(2\gamma-\gamma')^2\right]}.$$

The time dependence of the dipole moment is given by,

$$\vec{d}(t) = -e\left\{\rho_{10}\langle S_0|\vec{d}|S_1\rangle e^{-i\omega_{01}t} + \rho_{01}\langle S_1|\vec{d}|S_0\rangle e^{i\omega_{01}t}\right\}, \qquad (5)$$

and by comparing with the time dependent polarization the susceptibility is found and the absorption coefficient can be written as,

$$\alpha(\omega) = C\left|\langle S_0|\vec{d}|S_1\rangle\right|^2 \frac{\omega\gamma'}{(\omega_{01}-\omega)^2+\gamma'^2+\frac{\gamma'|\zeta|^2}{2\gamma}}, \qquad (6)$$

where C is a constant describing the concentration of the ensemble of two level systems, the second term is the oscillator strength, and the last term the line profile homogeneously broadened by the saturation of the transitions and by both radiative and environmental damping [Van77]. The last term determines the lineshape of the

absorption spectrum and is denoted by $F_L(\omega)$, where *L* stands for a Lorentzian lineshape. The full width half maximum (FWHM) of the absorption spectrum in this model is given by $2\sqrt{\gamma' + \gamma'|\zeta|^2/2\gamma}$, and in the limit that the transitions are not saturated $2\gamma + 2\gamma_{env}$. The radiative lifetime expressed in terms of the radiative rate is $T_1 = 1/2\gamma$ and dephasing time as $T_2 = 1/(\gamma + \gamma_{env})$. In the absorption experiment one measures the FWHM of a specific transition which – in the case of a homogeneously broadened transition can be used to determine the pure dephasing time τ if the radiative lifetime is known from $\tau = (1/T_2 - 1/2T_1)^{-1}$, Fig. 1 a and b. In carbon nanotubes each subband will have a series of excitons with only one of them being dipole allowed [And97, Spa04, Per04, Cha04]. Therefore, the absorption spectra will contain a series of peaks like in figure 1, one associated with each subband. Dephasing and life times of the optically allowed states will be discussed in chapter 4.

In almost all circumstances the interaction of excitons with the environment will shift and/or broaden the excitonic energy levels.. This can be considered due to a disordered dielectric environment and will introduce inhomogeneous broadening into the spectra. Broadening of this type is considered to cause a smearing of the energy levels δ over a normal distribution, $F_G(\omega)$, centered at the resonance, Fig. 1 c. A convolution of the inhomogeneous and homogeneous linewidths can be calculated by,

$$F(\omega) = \frac{\gamma}{\delta\sqrt{2\pi^3}} \int_{-\infty}^{\infty} \frac{e^{-\frac{(\omega-\nu)}{2\delta^2}^2}}{(\omega-\nu)^2 + \gamma} \, d\nu \,, \tag{7}$$

which is referred to as the Voigt lineshape and can be used to estimate the amount of inhomogeneity in an ensemble. In carbon nanotube ensembles an estimate of the

contribution of inhomogeneous broadening to the linewidth will be important for a determination of the pure and total dephasing times.

B. Photoluminescence Excitation Spectroscopy

Photoluminescence (PL) and photoluminescence excitation (PLE) spectroscopy is performed with a Jobin Yvon FluoroLog-3 equipped with a Electro-Optical Systems liquid nitrogen cooled InGaAs photodiode and a xenon lamp. The photocurrent measured when a fluorophore emits light is detected as a function of wavelength an provides information about η, the fluorescence quantum yield, the degree of coupling to the environment, and the nature of the relaxation to the ground state. This technique provides a powerful tool for the analysis of charge and energy transfer and will be used extensively throughout this dissertation. In particular the fluorescence stokes shift can provide information on the finer structure of excitonic levels even when the level splitting Δ is small with respect to room temperature [Efr96], Fig. 2 a and b.

Solvents may also influence fluorescence stokes shifts by changing the local dielectric function, an effect known as solvatochromism. This effect is important for using optical techniques for detection and characterization of the interaction of chemical species with a fluorescent species. Specifically in polar solvents the excitation of a chromophore leads to an induced dipole moment that can in turn induce an polarization of the solvent [Mar91, Mar93]. If the solvent responds slowly with respect to the radiative lifetime then no shift may be present, but if the solvent responds quickly then time dependent shifts are almost always present and can be probed experimentally with

ultrafast or continuous wave spectroscopy [Fle96]. If an additional Stokes shift is present do to the solvent, the shift is directly related to the interaction between the excited state and the solvent bath.

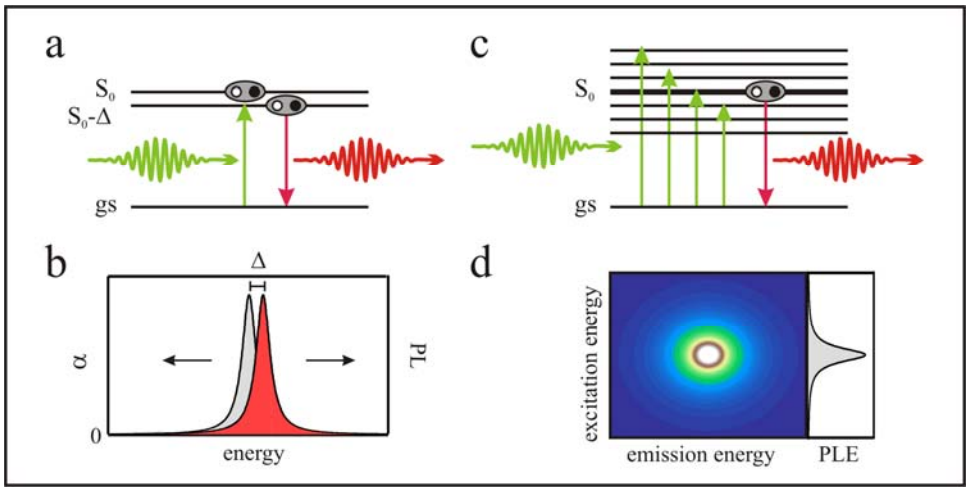

Figure 2 a. Schematic of a two level system with fine structure undergoing spontaneous emission after photoexcitation. **b.** Absorption and photoluminescence spectra of the system in **a**. The small energy difference between the absorption and photoluminescence is known as a Stokes shift. **c.** Schematic of the same system, but with the excitation source varied across the resonance. **d.** False color plot of a photoluminescence excitation spectrum. The maximum PL intensity is given in white, and vertical cuts are so called excitation spectrum.

Adding another dimension to fluorescence spectroscopy by tuning the excitation source allows one to further investigate the excited state, Fig. 2 c and d. This technique is commonly referred as photoluminescence excitation spectroscopy (PLE) and is especially useful for identifying spectral correlations in polydisperse samples. It is serves as a complimentary tool to absorption spectroscopy by reducing ambiguities due to spectral congestion, and also be used to detect single molecules [Amb91]. PLE spectroscopy has been very useful in characterizing nanotube samples and allowed for the first

spectroscopic assignment of polydisperse samples [Bac02, Wei03]. Moreover, sidebands associated with phonon replicas are apparent in this type of spectra that are not as apparent in absorption spectra [Ple05, Miy06]. Also, PLE has recently been used to identify an energy-transfer process from one tube species to another [Tor06].

C. Multidimensional Pump-probe Spectroscopy

1. Experimental Setup

In addition to continuous-wave spectroscopy, ultrafast pump-probe spectroscopy is used to probe the dynamics of the excited states and the recovery of the ground state (Section C2). Pump–probe experiments are performed with a regenerative amplifier driven optical parametric amplifier (Coherent Inc., RegA 9000 and OPA 9450) at 250 kHz repetition rate. The parametric amplifier provides tuneable sub 50 fs laser pulses in the visible range of the spectrum (470 nm–730 nm) or the infrared with the idler signal (800 nm–2000 nm) with pulse fluences of up to 0.2 μJ. The instrument also generates a white-light continuum which can be used as broadband probe from 1.6 μm up to 420 nm. The pump beam is focused into a spectrophotometer cell with 10 mm light path using a lens of 75 mm focal length (see Fig. 3). The broadband probe beam is likewise focused into this cell using spherical 100 mm focal length reflective optics. Pump and probe beams at the focus are estimated to be 250 μm and 100 μm in diameter respectively. In combination with the skew angle between pump and probe beams this gives rise to an increase of the pulse cross-correlation width of less than 30 fs. Unless noted otherwise,

pulse fluences from the pump are kept at or below 2.0×10^{14} photons/cm^2. The pump-beam delay is adjusted using a computer-controlled delay stage (Physik Instrumente, PIM521.DD) with a bi-directional reproducibility of positions of 0.1 μm = 0.66 fs. The white-light probe beam is dispersed in an imaging spectrograph (Jobin Yvon, Triax 320) and detected by a thermoelectrically cooled Si/InGaAs sandwich detector. Optical transients $\Delta T/T_0$ or $\Delta I/I_0$ (differential transmission), or $\Delta\alpha$ (differential absorption) can be recorded with a sensitivity of up to 2×10^{-6} using phase-sensitive detection as facilitated by chopping the pump beam, typically at 1 kHz.

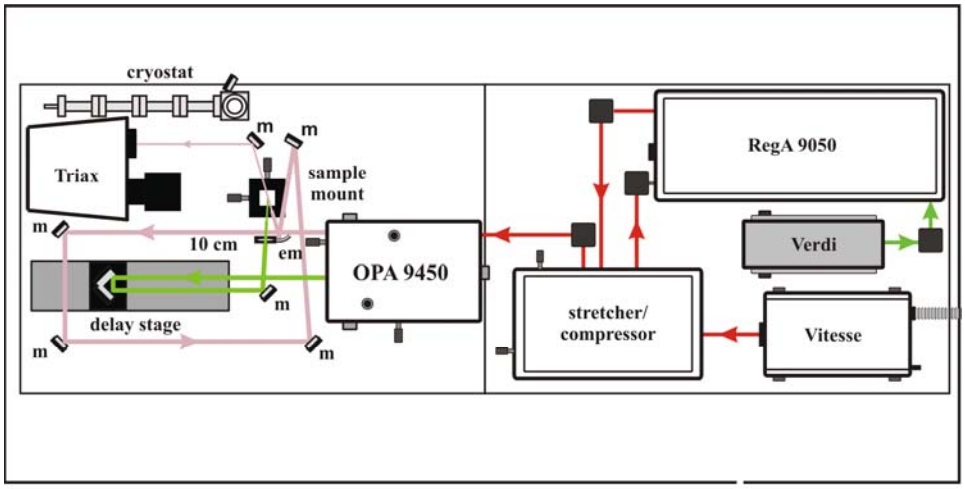

Figure 3. Schematic of the experimental setup for the pump-probe experiment. An 50 fs 100 mW 800 nm titanium safire oscillator (Vitesse) and a continuous wave 10 W 532 nm pump lser are used to drive a regenerative amplifier (RegA 9050) which produces sub 50 fs (after compression) 800 nm pulses with an average power of 1.8 W. An optical parametric amplifier (OPA 9450) is used to obtain pump pulses which can be tuned from 470-2000 nm and probe pulses are obtained from a broadband continuum that ranges from 420-1600 nm. The pump is sent through a delay stage and focuses onto the sample mount with a 10 cm lens, and the probe is fixed and focused onto the sample mount using an elliptical mirror (em). The probe beam is image in a spectrograph (Triax) equipped with a sandwiched thermoelectrically cooled Si/InGaAs photodiode. The detector signal is fed into a lock-in-amplifier which allows for differential transmission measurements. The pump and probe can also be focused into a cryostat for low temperature measurements.

At the wavelengths used in this study, photoabsorption cross sections of sp^2 hybridized polyaromatic hydrocarbon compounds on the order of 1×10^{-17} cm^2/atom [Tsy07] and for fluences used in this work would lead to roughly one absorbed photon per 10 nm of tube length or less. The associated temperature increase of the tube lattice is on the order of 1 K or less. Power-dependent measurement of optical transients confirmed that saturation occurs at significantly higher pulse fluences in which effects of Auger recombination may alter the dynamics [Wan04].

2. Theory of Exciton Phase Space Filling and the Nonlinear Response

In single-wall carbon nanotubes the dominant photoexcitations with the highest oscillator strengths are excitonic in nature due to reduced screening of the Coulomb interaction between electrons and holes [And97, Spa04, Per04, Cha04]. Excitons are composite bosons and must obey the exclusion principle due to their Fermionic constituents [Sch85]. As shown in section A the linear optical response of a two level system can be approximated as a Lorentzian,

$$\alpha(\omega) = C \frac{f}{(\omega_{01} - \omega)^2 + \gamma_{eff}^2}, \tag{8}$$

where f is the oscillator strength, C is a constant, ω_{01} is the transition frequency, and γ_{eff} is an effective broadening factor, Fig. 4 a and b. In SWNT the absorption spectrum can be modeled a series of Lorentzians associated with each interband transition. For excitons, the oscillator strength is proportional to the probability of finding the electron

and hole in the same unit cell $|\eta(r_h = r_e)|^2$ and the square of the electron and hole dipole moment $|\mu_{e-h}|^2$ [Hau04]. Following the derivation by Schmitt-Rink [Sch85], the nonlinear signal induced by the pump probe experiment (transient absorption) is due to a change in any of the three quantities f, γ_{eff}, or ω_{01}. Upon excitation, a density of *N* excitons will be promoted from the ground state into the excited state, and as long as $N \neq N_S$ where N_S is the density of excitons needed to saturate the transitions, the broadening γ_{eff} will only be due to environmental and radiative damping. A change of the transitions frequency ω_{01} would result in a shift of the resonance which will be discussed later. If the change in the absorption is considered to be due to a renormalization of the oscillator strength such that,

$$\frac{\delta f}{f} = -\frac{N}{N_s}, \tag{9}$$

then the physics behind the non-linear signal will be due to blocking of transitions due to the Pauli principle or change in the exciton wavefunction due to changes in the Coulomb interaction due to the present of other excitons (which is also due to the Pauli principle). The former is an effect of phase space filling and the latter due to the exchange interaction. As shown in reference [Sch85] the exchange effects are similar to the phase space filling in 2D quantum wells and here it will be assumed the same is for the 1D nanotube.

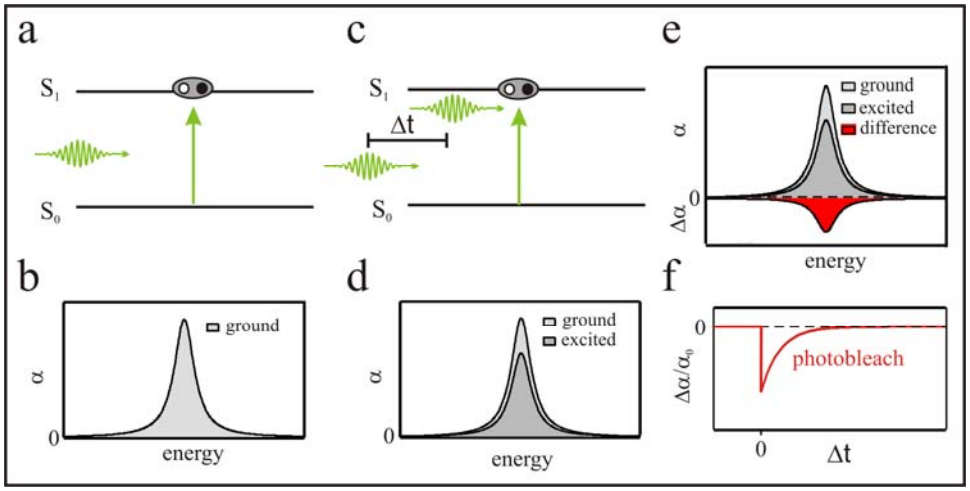

Figure 4 a. Schematic of a two-level system in which the ground state is fully populated, and the corresponding ground-state absorption spectrum in **b.** The pump-probe experiment consist of exciting the system with an ultrafast pulse and probing the changes in the populations of both the ground and excited states as a function of pump-probe delay, as in **c.** The resulting transient absorption spectrum is the difference of the ground state and excited state spectrum **d.** and **e.** The number of carriers in the ground state is reduced by photoexcitation and the sample is photobleached. The photobleach signal can be monitored as a function of pump-probe delay **f.**, and the dynamics of the ground-state recovery is obtained.

The generation of an exciton gas of density N will lead to distribution g of electrons and holes in phase space that is related to the Fourier transform of the exciton envelope wavefunction,

$$g_e(k) = g_h(k) = \frac{N}{2}\left|\eta(k)\right|^2 \quad . \tag{10}$$

For excitons in carbon nanotubes the exciton wavefunction can be approximated by a Gaussian of width σ and is written as,

$$\psi(\vec{r}_e, \vec{r}_h) = C\sum_{c,v} A_{c,v}\varphi_c(\vec{r}_e)\varphi_v^*(\vec{r}_h)e^{-\left[(z_e - z_h)/\sqrt{2}\sigma\right]^2}, \tag{11}$$

where φ is the e-h single particle wavefunctions, $A_{c,v}$ are interference factors between pair excitations determined by symmetry, C is a normalization factor, and the Gaussian

envelope function η describes the correlated motion of the electron and hole [Cap06]. In order to incorporate the effects of filling phase space on the renormalization of the oscillator strength, the relative change in size of the exciton must be weighted by the distribution of electrons and holes such that,

$$\frac{\Delta f}{f} = -\sum_k \left[g_e(k) + g_h(k)\right] \frac{\eta(k)}{\eta(z_e = z_h)} \ . \tag{12}$$

The normalized envelope of the real space wavefunction is given by $\eta(z_e, z_h) = \left(1/\sqrt{\sigma\pi^{1/2}}\right)\exp\left[-(z_e - z_h)^2/2\sigma^2\right]$ and its Fourier transform is given by $\eta(k) = \sqrt{2\sigma\pi^{1/2}}\ \exp\left[-(k\sigma)^2/2\right]$. Therefore, by integrating over all *k* in equation 12 equation 9 becomes $\delta f / f = -2\sqrt{\pi/3}\sigma N$, which is directly related to the nature of the e-h interaction in SWNT which simplifies the distributions in phase space. Therefore the density of excitons needed to saturate the transition or completely fill the phase space is $N_s = 1/2\sigma\sqrt{3/\pi}$. For a exciton size of 3 nm this would correspond to a density of approximately one exciton every 6 nm. As stated earlier fluences used in this work create roughly one exciton per every 10 nm or less in order to neglect effects of saturation. Phase-space filling effects on the renormalization of the oscillator strength can now be incorporated into the instantaneous normalized transient-absorption spectrum such that $\Delta\alpha/\alpha_0 = \delta f / f \approx -2\sqrt{\pi/3}\sigma N$. Upon excitation a negative transient absorption signal will be observed whose magnitude depends on the excitation density relative to the saturation density, Fig. 4 c, and d. One can then perform a power-dependent measurement, which correlates with a change in the excitation density if the absorption cross section is known, and determine the exciton size within this linear regime.

In addition to phase-space filling which causes a bleaching of the ground state spectrum there can be excited state absorption which can lead to so called photoabsorption, Fig. 5. An additional spectral feature may appear that is not related to absorption from the ground state. In J-aggregates, which involve coherent exciton motion among many molecules of the aggregate, effects such as this are usually phenomenologically assigned to a state in which a two-exciton manifold is accessed. A blue shift in the spectrum is described in terms of the energy penalty paid by the aggregate to share two excitons coherently.

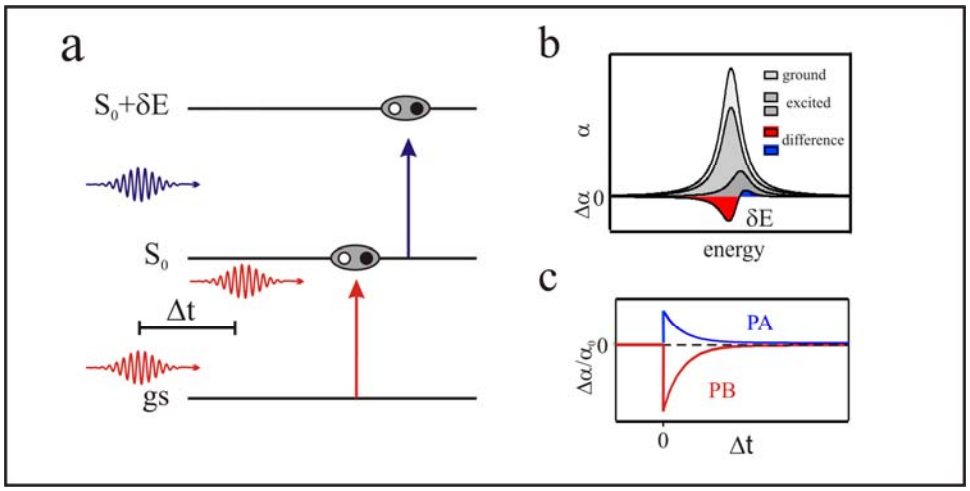

Figure 5 a. In some instances the excited state can be shifted with respect to its original position. This causes the excited state spectrum to be shifted with respect to the ground state spectrum as in **b.** The resulting transient absorption spectrum will contain both a negative signal due to the ground state depletion and a positive signal due to excited state absorption **c.** They are respectively know as photobleach (PB) and photoabsorption (PA) and can be monitored as a function of pump-probe delay and contain the dynamics of the ground state recovery as well as the dynamics of the environmental fluctuations.

Therefore with the magnitude of the blueshift one can obtain the number of molecules in which the two exciton entity is coherent if the interaction between molecules is known [Min94]. Conversely, in PbSe quantum dots photoabsorption is observed below the band gap and is assigned to intraband transitions [Weh02]. In essence, when the quantum dot is in the excited state selection rules that are found in the ground state are relaxed in the excited state and formerly optically forbidden states become optically allowed. In SWNT the photoabsorption effect has been observed previously but is not very well understood due to poor sample quality [Cho05, Yan05].

So far only the instantaneous transient spectrum has been discussed and the dynamics must be accounted for. The optical Bloch equations were used in section A to describe the linear optical properties of a two-level bound system such as an exciton. It was shown that the absorption coefficient is relate to the imaginary part of the linear susceptibility, which is also proportional to the imaginary part of the dielectric function $\varepsilon_2(\omega)$. Any time-dependent change in the absorption coefficient $\alpha(\omega)$ is going change the dielectric function and the index of refraction such that,

$$\Delta\alpha(\omega) = \frac{\omega}{c}\frac{\Delta\varepsilon_2(\omega)n(\omega) - \varepsilon_2(\omega)\Delta n(\omega)}{n^2(\omega)}. \tag{13}$$

The imaginary part of the dielectric function can be approximated for Fermi's golden rule as,

$$\varepsilon_2(\omega) = \frac{2\pi e}{m\omega} f(\omega)\rho(\omega), \tag{14}$$

where f is the oscillator strength describe above and ρ is the exciton density of states. Therefore equation 13 becomes,

$$\Delta\alpha(\omega)=\frac{2\pi e}{mc}\frac{f(\omega)\Delta\rho(\omega)n(\omega)+\Delta f(\omega)\rho(\omega)n(\omega)-f(\omega)\rho(\omega)\Delta n(\omega)}{n^2(\omega)}\ , \qquad (15)$$

which describes the full evolution Δ of the frequency dependent absorption coefficient in terms of change in the oscillator strength, the index of refraction, and the density of states. When normalized to the unperturbed absorption spectrum α_0 the transient absorption spectrum is,

$$\frac{\Delta\alpha}{\alpha_0}=\frac{\Delta\rho}{\rho_0}+\frac{\Delta f}{f_0}-\frac{\Delta n}{n_0}\ . \qquad (16)$$

In the case of low excitation density the change in the density of states is going to be negligible with respect to density of states i.e. $\Delta\rho/\rho_0\approx 0$. Moreover, a low excitation density implies a small impinging field and changes in the index of refraction will small with respect to the index of refraction i.e. $\Delta n/n_0\approx 0$. Therefore, the transient absorption spectrum is fully captured in the phase space filling model in the limit of low excitation density as,

$$\frac{\Delta\alpha}{\alpha_0}(t)\approx -2\sqrt{\frac{\pi}{3}}\sigma N(t). \qquad (17)$$

The time dependence of the excitation density reflects the time dependence of the ground state filling for a two level system by $N(t)=1-N_{gs}(t)$. For pure two level system cross-correlations of the transient spectrum will decay mono-exponentially as in figure 4 f. A consequence of this is that in pump-probe experiments of a two level system one is always probing the recovery of the ground state or equivalently the depletion of the exited state. If one is confronted with a system that contains more than one level, for example a very slowly decaying intermediate state between the ground and excited state, the time dependence of the ground state density will be change such that

$N_{gs}(t) = 1 - N(t) - N_i(t)$. This will change the transient spectrum into, $\Delta\alpha/\alpha_0(t) \approx -2\sqrt{\pi/3}\sigma\left[1 - N_{gs}(t) - N_i(t)\right]$, and cross correlations associated with the transient spectrum will not decay mono-exponentially. Moreover, if one could do an experiment in which solely the ground state filling is being probed, the filling of the intermediate state could be found which is the excited state lifetime. This could be done by normalizing the cross-correlations of a degenerate excited state pump-probe experiment with an experiment that is pumping the excited state but probing off resonance at a higher energy, and at some time τ, much longer than the lifetime of the excited state, subtracting the two yielding time dependence of the filling of intermediate state,

$$\delta[\Delta\alpha(t)] = C_{res}\left[\frac{\Delta\alpha}{\alpha_0}(t)\right]_{res} - C_{offres}\left[\frac{\Delta\alpha}{\alpha_0}(t)\right]_{offres} = CN_i(t)\ , \qquad (18)$$

where C_{res} and C_{offres} are normalization factors equal to C. The filling of the intermediate state is exactly the exited state lifetime for times much smaller than τ and this principle will be used to find the excited state lifetime of the E_{11} exciton in SWNT.

D. References

[Amb91] Ambrose, W. P., T. Basche, et al. (1991). "Detection and Spectroscopy of Single Pentacene Molecules in a Para-Terphenyl Crystal by Means of Fluorescence Excitation." Journal of Chemical Physics **95**(10): 7150-7163.

[And97] Ando, T. (1997). "Excitons in carbon nanotubes." Journal of the Physical Society of Japan **66**(4): 1066-1073.

[Bac02] Bachilo, S. M., M. S. Strano, et al. (2002). "Structure-assigned optical spectra of single-walled carbon nanotubes." Science **298**(5602): 2361-2366.

[Cap06] Capaz, R. B., C. D. Spataru, et al. (2006). "Diameter and chirality dependence of exciton properties in carbon nanotubes." Physical Review B **74**(12).

[Cha04] Chang, E., G. Bussi, et al. (2004). "Excitons in carbon nanotubes: An ab initio symmetry-based approach." Physical Review Letters **92**(19).

[Cho05] Chou, S. G., M. F. DeCamp, et al. (2005). "Phonon-assisted exciton relaxation dynamics for a (6,5)-enriched DNA-wrapped single-walled carbon nanotube sample." Physical Review B **72**(19).

[Efr96] Efros, A. L., M. Rosen, et al. (1996). "Band-edge exciton in quantum dots of semiconductors with a degenerate valence band: Dark and bright exciton states." Physical Review B **54**(7): 4843-4856.

[Fle96] Fleming, G. R. and M. H. Cho (1996). "Chromophore-solvent dynamics." Annual Review of Physical Chemistry **47**: 109-134.

[Lou83] Loudon, R. (1983). The Quantum Theory of Light.

[Mal04] Malloci, G., G. Mulas, et al. (2004). "Electronic absorption spectra of PAHs up to vacuum UV - Towards a detailed model of interstellar PAH photophysics." Astronomy & Astrophysics **426**(1): 105-117.

[Mar91] Maroncelli, M. (1991). "Computer-Simulations of Solvation Dynamics in Acetonitrile." Journal of Chemical Physics **94**(3): 2084-2103.

[Mar93] Maroncelli, M. (1993). "The Dynamics of Solvation in Polar Liquids." Journal of Molecular Liquids **57**: 1-37.

[Min94] Minoshima, K., M. Taiji, et al. (1994). "Femtosecond Nonlinear-Optical Dynamics of Excitons in J-Aggregates." Chemical Physics Letters **218**(1-2): 67-72.

[Miy06] Miyauchi, Y. and S. Maruyama (2006). "Identification of an excitonic phonon sideband by photoluminescence spectroscopy of single-walled carbon-13 nanotubes." Physical Review B **74**(3).

[Per04] Perebeinos, V., J. Tersoff, et al. (2004). "Scaling of excitons in carbon nanotubes." Physical Review Letters **92**(25).

[Ple05] Plentz, F., H. B. Ribeiro, et al. (2005). "Direct experimental evidence of exciton-phonon bound states in carbon nanotubes." Physical Review Letters **95**(24).

[Sch85] Schmitt-Rink, S., D. S. Chemla, et al. (1985). "Theory of Transient Excitonic Optical Nonlinearities in Semiconductor Quantum-Well Structures." Physical Review B **32**(10): 6601-6609.

[Spa04] Spataru, C. D., S. Ismail-Beigi, et al. (2004). "Quasiparticle energies, excitonic effects and optical absorption spectra of small-diameter single-walled carbon nanotubes." Applied Physics a-Materials Science & Processing **78**(8): 1129-1136.

[Tor06] Torrens, O. N., D. E. Milkie, et al. (2006). "Photoluminescence from intertube carrier migration in single-walled carbon nanotube bundles." Nano Letters **6**(12): 2864-2867.

[Van77] Vanvleck, J. H. and D. L. Huber (1977). "Absorption, Emission, and Linebreadths - Semi-Historical Perspective." Reviews of Modern Physics **49**(4): 939-959.

[Wan04] Wang, F., G. Dukovic, et al. (2004). "Observation of rapid Auger recombination in optically excited semiconducting carbon nanotubes." Physical Review B **70**(24).

[Weh02] Wehrenberg, B. L., C. J. Wang, et al. (2002). "Interband and intraband optical studies of PbSe colloidal quantum dots." Journal of Physical Chemistry B **106**(41): 10634-10640.

[Wei03] Weisman, R. B. and S. M. Bachilo (2003). "Dependence of optical transition energies on structure for single-walled carbon nanotubes in aqueous suspension: An empirical Kataura plot." Nano Letters **3**(9): 1235-1238.

[Yan05] Yang, J. P., M. M. Kappes, et al. (2005). "Femtosecond transient absorption spectroscopy of single-walled carbon nanotubes in aqueous surfactant suspensions: Determination of the lifetime of the lowest excited state." Physical Chemistry Chemical Physics **7**(3): 512-517.

[Tsy07] Tsyboulski, D.A., J.D.R. Rocha, et al. (2007). "Structure-Dependent Fluorescence Efficiencies of Individual Single-Walled Carbon Nanotubes." Nano Letters **7**(10): 3080-3085.

CHAPTER III

PREPERATION OF COLLOIDAL SUSPENSIONS AND COMPOSITE FILMS OF SINGLE-WALL CARBON NANOTUBES

The preparation of both colloidal and composite film single-wall carbon nanotube samples for spectroscopic analysis is presented. Three different tube sources synthesized by different techniques were investigated. Spectroscopy of these samples is made possible by the preparation of colloidal suspensions that can be further processed using density gradient ultracentrifugation for structural or metallicity sorting and thin film fabrication. Nanotube crystallite engineering is used to investigate charge and energy transfer among like (n,m) species and gives details on the van der Waals interaction between tubes.

A. Single-wall Carbon Nanotube Sources

Single-wall carbon nanotubes synthesized by high pressure, 30-50 atm, high temperature, 900-1100 °C, gas phase catalytic decomposition of carbon monoxide, where the catalyst is formed in situ by decomposition of iron pentacarbonyl are known as HiPco tubes [Nik99, Bro01]. During their synthesis SWNTs already begin to form bundles due to van der Waals interactions. Scanning electron and transmission electron micrographs of this material are shown in figure 1 a. Detailed analysis of Raman spectra show they contain a broad diameter distribution ranging from 0.8 to 1.4 nm [Kuk02]. This broad

diameter distribution includes more than 40 (n,m) species of which about 1/3 are metallic [Jor05]. An absorption spectrum of HipCo tubes in a gelatin matrix is shown in figure 1 b. The polydisperse character of these samples is evident from the broad range of overlapping band gap transitions in the near infrared range of the spectrum, here from about 950 nm to 1600 nm. Spectroscopic analysis of samples with so many tube species is a daunting task due to strong spectral congestion.

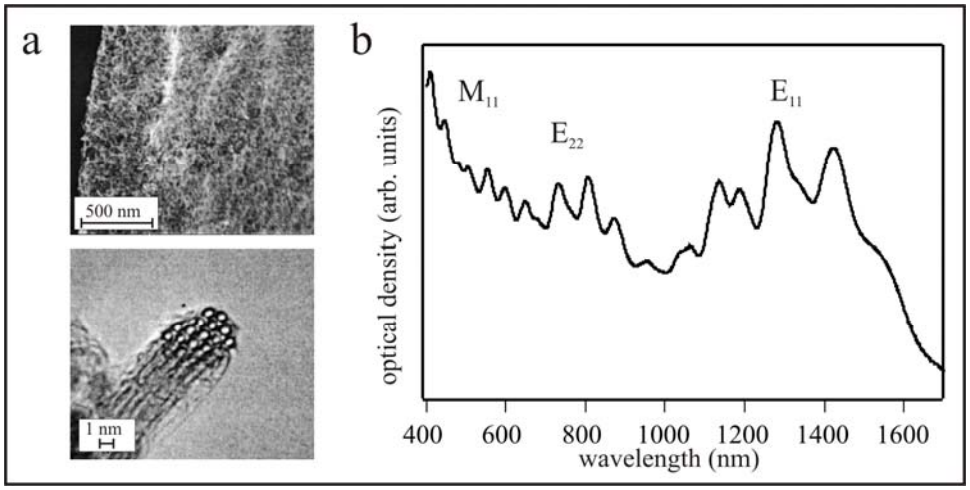

Figure 1 **a.** Scanning electron microscope and transmission electron microscope images of single-wall tubes grown by the HiPco method [Nik99]. **b.** Absorption spectra of Hipco tubes in a gelatin matrix.

Growth of SWNTs with a narrow diameter distribution is of great benefit for their spectroscopic exploration and is achieved by altering growth conditions and catalyst composition in the chemical vapor deposition (CVD) process. Resasco and coworkers, for example, have greatly reduced the polydispersity of (n,m) indices using the CoMoCAT process [Jor05]. Here, carbon monoxide is catalytically decomposed in the presence of a solid cobalt molybdenum/silicon dioxide catalyst. If compared to the HiPco

synthesis this process utilizes lower temperatures on the order of 700-800 °C, and the supply of carbon feedstock is achieved by flowing CO over the catalyst in a range from 1-10 atm [Kit00]. Transmission electron micrographs of CoMoCAT material are shown in figure 2 a. Resasco et al found that by changing the Co to Mo stochiometry and by slightly varying the growth temperature they can tailor the nanotube diameter distribution [Lol06]. Absorption spectra of two CoMoCAT samples grown under different conditions are shown in figure 2 b. One of the samples is dominated by the (6,5) tube which makes up for about 2/5 of the material [Jor05] (see black line in Fig. 2 b). The more polydisperse sample (blue line in Fig. 2 b) contains a majority of (6,5) (7,5) (8,3) and (7,6) tubes.

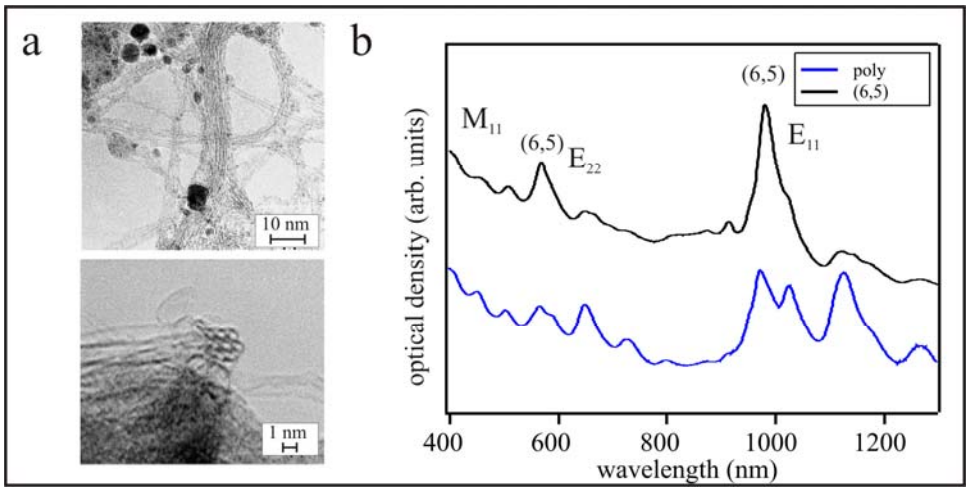

Figure 2 a. Transmission electron microscope images of CVD single-wall tubes grown by the CoMoCAT method [Kit00]. **b.** Absorption spectra of colloidal CoMoCAT tubes grown by different conditions.

CVD growth techniques such as the HiPco process produce tubes in the range from 0.6 nm to 1.4 nm centered at the most abundant diameter. Larger diameter tubes can be synthesized by pulsed laser vaporization of a graphitic target under the flow of an

inert gas and contain a distribution of diameters – with tunable with growth conditions - ranging from 1.1 to 1.7 nm [Rin98]. Scanning electron and transmission electron micrographs are shown in figure 3 a. as well as absorption spectra in 3 b. Despite a broad range of diameters, these tubes are well suited for electronic applications because variations of bandgap transition energies at these larger diameters are comparatively small [Kat99]. Also, recent advances in SWNT separation have shown that metallicity plays a role in the dispersion of tubes in various surfactants, a fact which can be used to separate metallic nanotubes from semiconducting nanotubes [Arn06]. This separation technology may facilitate the use of laser vaporization tubes for the fabrication of CNT based flexible conductive electrodes.

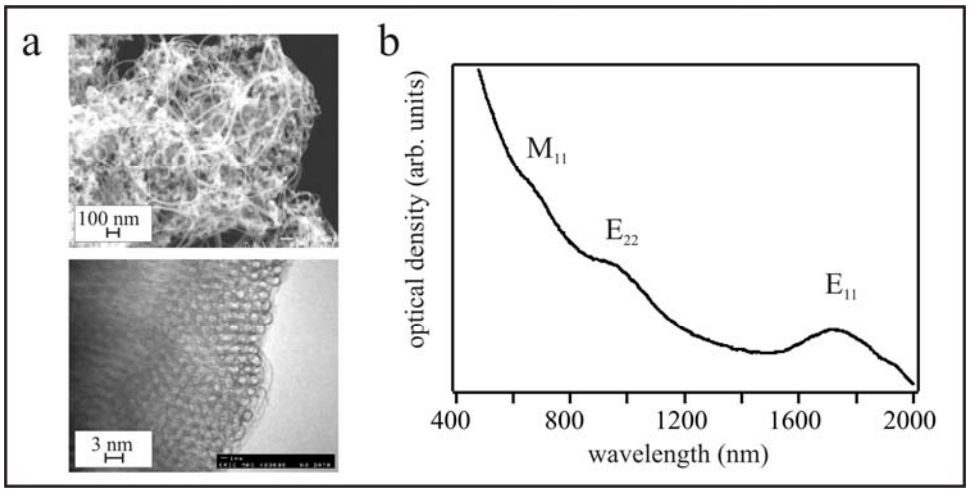

Figure 3 a. Scanning electron microscope and transmission electron microscope images of laser vaporization grown single-wall carbon nanotubes [Rin98]. **b.** Absorption spectra of laser vaporization tubes in a gelatin matrix.

B. Preparation Colloidal Suspensions by Surfactant Encapsulation

Ultrasonication in aqueous amphaphilic surfactants such as sodium cholate (SC), sodium dodecyl sulfate (SDS), and sodium dodecyl benzene sulfonate (SDBS) is here being used to break nanotube aggregates apart and to stabilize the resulting fragments including single tubes in aqueous suspensions [O'Co00, Rig00, Moo03]. This process yields suspension that can be used for spectrofluorometric investigations of semiconducting SWNT species [Bac02]. Alternatively, deoxyribonucleic acid (DNA) can be also used as surfactant which opens up the possibility to use nanotubes as biological probes and fluorescent markers. [Zhe03]. When the surfactant in solution reaches a critical concentration it is energetically favorable for it to form micelle structures that can encapsulate a particle if the surface energy between the particle and the surfactant is at a local minimum [Man95]. In the case of the graphitic surface, SDS had been shown to organize itself in periodic structures when the solution concentration exceeds 2.8 mM or 0.1% [Wan96]. Suspensions containing micelle encapsulated nanotubes are metastable and can aggregate over time due to the relatively weak binding energy ($>kT$) of the surfactant molecule to the surface.

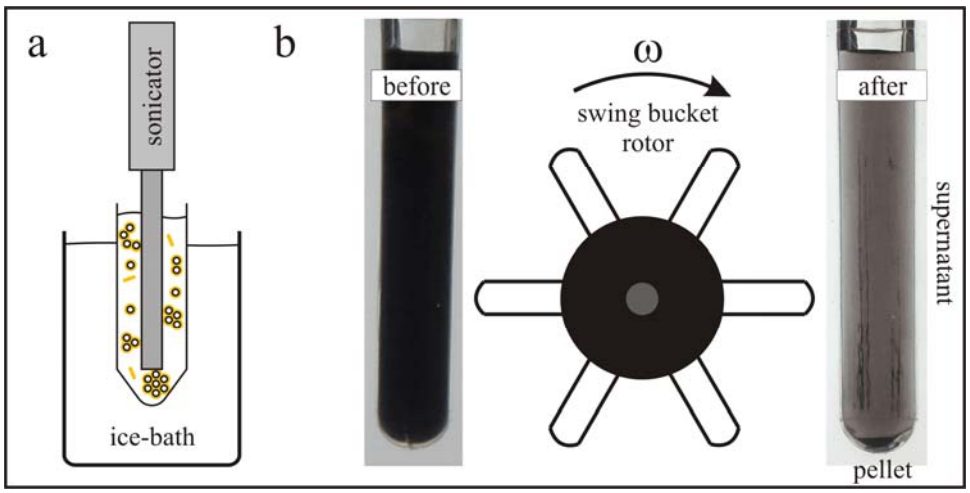

Figure 4 **a.** Schematic of surfactant encapsulation of isolated tubes and small tube bundles with ultrasonication. **b.** Colloidal suspensions are removed of insoluble material by ultracentrifugation in a swing bucket rotor.

In this work, several milligrams of raw nanotube soot are placed in 10 ml of high performance liquid chromatography (HPCL) water which – unless noted otherwise - contain 2.0% surfactant by weight. The mixture is then sonicated in an ice bath for two hours with a Branson 450 Sonifer at 30% duty cycle. The output power control is set to 3 on a full scale of 0-10. This corresponds to an effective sonication time of approximately 36 minutes. Previous studies on the length distribution of ultrasonically dispersed HipCO CNTs have shown that the average nanotube length under these conditions is approximately 400 nm [Hel04]. The resulting mixtures are then placed in Beckman Ultra-Clear 14x89 mm centrifuge tubes and centrifuged in a Sorvall ultracentrifuge with a TH-641 swing bucket rotor for 4 hours at speeds between 31 krpm. The top 75% of the supernatant is then decanted from the centrifuge tube and undergoes further processing or is analyzed spectroscopically, Fig. 4 a and b. The colloidal suspensions obtained by the method outlined above are fluorescent and are sufficient for determination of the composition of semiconductors within the sample using photoluminescence excitation

spectroscopy (PLE). A PLE spectrum of HiPco material encapsulated in 2% SDS and centrifuged for 4 hrs at 30 krpm is shown in figure 5. The (n,m) indices are assigned according to the tight binding model in which the E_{22} transition wavelengths are a function of the E_{11} transition wavelengths [Wei03].

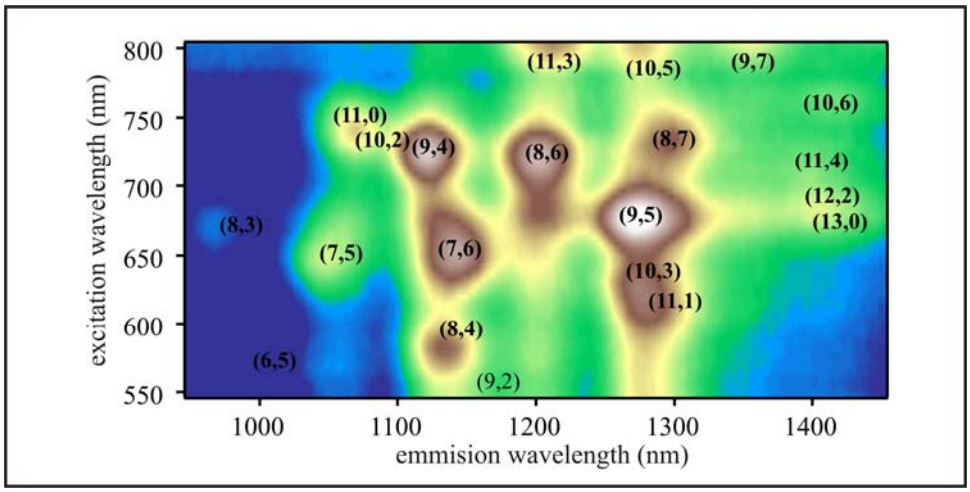

Figure 5. Photoluminescence excitation spectra of a colloidal Hipco with SDS used as a surfactant. The excitation range covers most of the E_{22} transitions.

C. Density Gradient Ultracentrifugation as a Sorting Tool

1. Structural Sorting of CoMoCAT Tubes

Density gradient ultracentrifugation (DGU) has been previously used to structurally sort hydrated proteins that have different buoyant densities [Red75]. This technique will here be used for processing of heterogeneous colloidal suspensions following an approach recently introduced by Arnold et al. [Arn05]. As outlined by

Schuck [Sch00], the sedimentation and diffusion of monodisperse particles in a spinning centrifuge vial with concentration profile $C(r,t)$ is found by solving the Lamm equation,

$$\frac{d}{dt}C(r,t)=\frac{1}{r}dr\left[rD\frac{d}{dr}C(r,t)-s\omega^2r^2C(r,t)\right], \tag{1}$$

where ω is the angular velocity of the rotating vial, D is the particle diffusion- and s its sedimentation coefficient, which both dependent on the particle size or molar mass *M*. The first and second terms on the right hand side determine the balance between diffusion and sedimentation which depends on the angular velocity. The Svedberg equation relates the sedimentation coefficient to the diffusion coefficient by,

$$s(M)=D(M)\frac{M(1-\nu_m\rho)}{RT}, \tag{2}$$

where *R* is the universal gas constant, *T* is the temperature, and ν_M is the particles partial specific volume. For a density gradient the solvent density ρ will depend on the gradient profile and is a function of the centrifugation coordinate *r*. If ν_M is known, an equivalent sphere of radius $\overline{R}$ can be calculated with the same volume of the particle and the frictional ratio $(f/f_0)_M$ will contain the shape information of hydrodynamic frictional coefficient. The diffusion coefficient for an equivalent spherical particle is then found by the Einstein-Stokes relationship as,

$$D(M)=\frac{kT}{6\pi\eta_0\eta_R(f/f_0)_M\overline{R}}, \tag{3}$$

where *k* is the Boltzmann constant, and η_0 and η_R are the standard and relative viscosities of the solution which both depend on the centrifugation coordinate *r* in a gradient. In figure 4 a. it is evident that the pellet in the bottom consists of large insoluble material in which diffusion was overcome by sedimentation and the solubalized

gray material had a large enough diffusion coefficient that sedimentation did not take place even at centrifugation forces of up to 200,000 g.

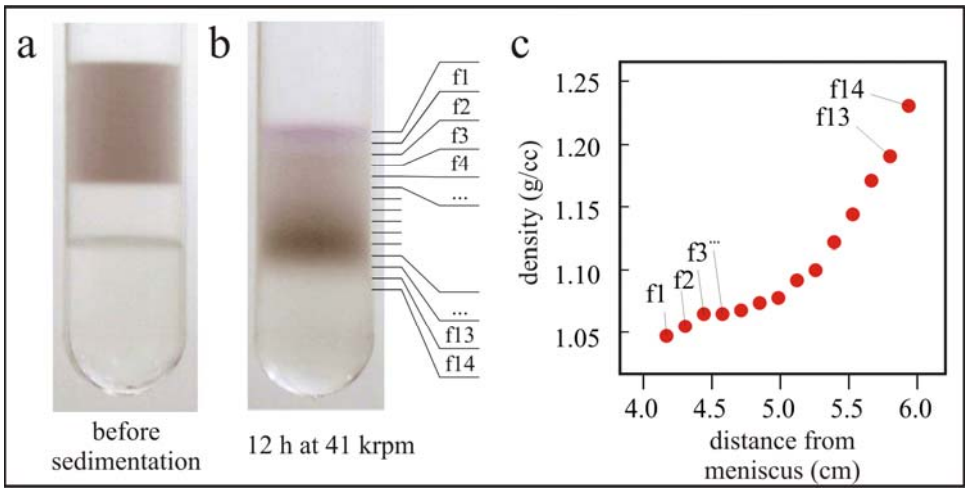

Figure 6 a. Centrifuge vial of before and **b.** after ultracentrifugation. **c.** Fraction density as a function of position from the meniscus.

In order to determine the structural composition of traditionally prepared colloidal suspension, DGU was used to sort the particulates of a suspension of (6,5) enriched CoMoCAT tubes [Cro07]. A water soluble density gradient material, Optiprep, which is composed of an aqueous solution of 60% iodixanol and has a density of 1.32 g/cc was prepared in a step gradient along with a supernatant of (6,5) enriched CoMoCAT SWNT suspended in 2% SC, Fig. 6 a. The step gradient consists of 5 layers with from bottom to top consisting of 2 ml of 60% iodixanol, 1.5 ml of 18% iodixanol, 2 ml of SWNT supernatant adjusted to 13.5% iodixanol, 1.5 ml of 9% iodixanol, and 3 ml of water. All layers contained 2% SC in order to keep the micelle concentration constant. In order to form a linear gradient, the step gradient was carefully tilted on its side allowing the steps to diffuse into each other for a period of two hours. The vial was then carefully tilted

upright and centrifuged for 12 hrs at 41 krpm. Separation of the supernatant into its constituents was achieved and fractionated into 12 200 μL fractions with a home built upward displacement fractionator using Fluorinert as a dense, 1.60 g/cc, chase medium , Fig 6 b. The density of each fraction was measured as function of position from the meniscus and ranged from 1.055-1.240 ± 0.005 g/cc.

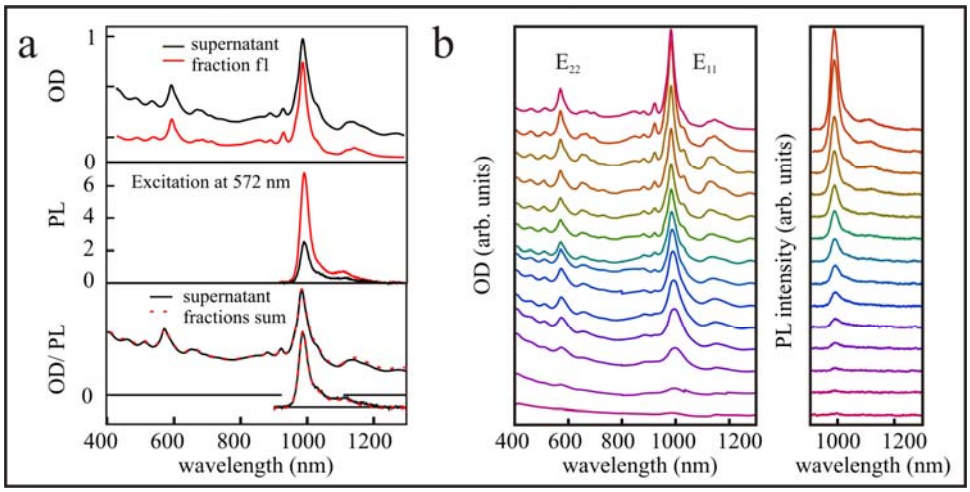

Figure 7 a. From top to bottom: Supernatant and fraction f1 absorption and photoluminescence spectra, and the sum of all fractions from **b** compared to the supernatant **b.** Absorption and photoluminescence spectra from the fourteen fraction in figure 6.

Absorption and fluorescence spectra of the supernatant and top most fraction f1 are shown in figure 7 a. The topmost fractions are characterized by a large decrease in the nonresonant background in the visible and a reduction in the inhomogeneously broadened linewidth of the (6,5) E_{22} and E_{11} transitions. Also the PL intensity of the fraction f1 is greater than the supernatants even thought the optical density in the visible is larger in the supernatant than fraction f1. Absorption and fluorescence spectra of all of the fourteen fractions are given in figure 7 b. There is a constant increase in the

nonresonant background with respect to the (6,5) E_{22} transition as well a redishift in the transition wavelengths. Additionally, the PL shows a constant decrease in intensity that is correlated with the increase in the nonresonant background and broadening in the lower fractions. This experiment has astounding effects on the interpretation of SWNT optical experiments using material like the supernatant because it contains such a wide variety of constituents ranging from highly florescent material to non fluorescing material. The density change from the top to bottom suggest that a wide range of isolated nanotubes and nanotube crystallites are present in the supernatant in accordance with the size dependent concentration effects modeled by the Lamm equation. These effects suggest structural sorting is taking place during the DGU procedure.

In order to investigate the validity of structural sorting, a CoMoCAT sample encapsulated in ss-DNA, gt-30, was prepared by DGU (courtesy of M. Arnold [Arn05]) and three fractions were imaged using tapping mode atomic force microscopy. The fractions were chosen such that on average each sample possibly contained isolated tubes, large crystallites that remained soluble, and one fraction in between the two. Analysis of the absorption spectrum including the magnitude of redshift from the top fraction, the magnitude of the non-resonant background, and feature linewidth were taken into consideration. Samples were prepared by drop casting 20 μL of 10 x diluted suspension on freshly cleaved mica that was functionalized with 10 mM NiCl and 100 mM trishydroxymethylaminomethane. The drop was allowed to stand for 10 minutes before blown off with dry nitrogen. The sample was then rinsed in HPCL water for 5 minutes in order to remove any excess DNA and iodixanol.

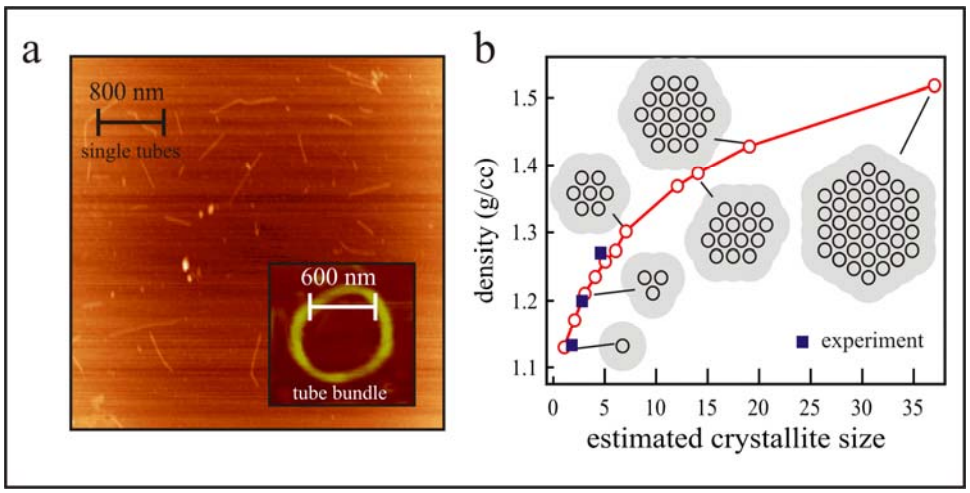

Figure 8 a. Tapping mode atomic force microscope images of CoMoCAT SWNT encapsulate in ss-DNA on a functionalized mica substrate. Isolate tubes have an average height of 1 nm and length of 400 nm while tube crystallites (inset) can be several microns in length and have an average height of 4 nm **b.** Model of the density of different size tube crystallites composed of 1 nm tubes and its solvation shell complex. The solvation shell is taken to be a constant thickness of 1 nm and density of 1.0 g/cc, while the tubes are placed 0.34 nm apart with a density of 1.3 g/cc. Experimental data using AFM heights and measured fraction densities is given in blue.

The first fraction had an average height of 1 nm with a density of 1.134 g/cc, the second an average height of 1.4 nanometers with a density of 1.2 g/cc, and the third an average height of 1.86 nm with a density of 1.27 g/cc. Images of the first and a close up of a representative crystallite in the last is shown in figure 8 a. Estimations of the number n of tubes within a crystallite were made by considering the total density $\rho(n)$ of an infinitely long DNA solvation shell /SWNT complex. This can be computed by,

$$\rho(n) = f_s(n)\rho_s + f_{SWNT}(n)\rho_{SWNT} \ , \qquad (2)$$

where $f_s(n)$ is the mass fraction of the solvation shell and $f_{SWNT}(n)$ is the mass fraction of the SWNT crystallite containing n tubes. The density of the solvation shell was estimated to be 1.0 g/cc and the density of the SWNT 1.3 g/cc. The mass fraction of the

solvation shell was computed by considering that the shell uniformly filled the space outside of the crystallite (schematically shown in figure 8 b) at a constant thickness of 1 nm and the area of each was computed using a Monte Carlo integration package in Igor, Fig. 8 b. For a crystallite of *n* tubes or diameter $D(n)$ the SWNT mass fraction was computed by $f_{SWNT} = 1 - f_s$. Crystallites were hypothetically constructed such that the contact area between tubes was maximized in order to emulate the maximization of the intertube van der Waals interaction. The density of the SWNT crystallite/solvation shell complex was found to increase as a function of the number of tubes within the crystallite. Measured fraction densities where compared to densities computed using average AFM heights as the diameter $D(n)$ of a crystallite/solvation complex, and the validity of the estimation within experimental error and theoretical accuracy is evident in figure 8 b. Additionally, for the fraction densities measured crystallites composing of up to seven tubes were found to be solubalized, while larger ones were sedimented.

2. Structural and Metallicity Sorting of Laser Vaporization Tubes

Vacuum filtrated thin films (VFTF) of Laser vaporization (LV) synthesized SWNT have demonstrated exceptional transport properties, and have found use in percolating network thin film field effect transistors and light emitting diodes [Mar06, Bo05] . With relatively small band gaps (~700 meV) and relatively small spreads in transition energies (~250 meV) as compared to HiPco with a mean band gap of approximately 1.1 eV with a spread of approximately 700 meV, large currents and

efficient percolation paths that are non-metallic can be obtained by tuning the thickness of the film. By using DGU one can reduce the spread in transition energies and investigate the transport properties of networks containing a certain diameter range of tubes. Here, LV tubes synthesized by Conseil de National Researches were suspended in 2% SC and centrifuged at 15 krpm for 2 hrs to remove insoluble material. A 2% SC step gradient was then made consisting of (from bottom to top): 2 mL 60% iodixanol, 1.5 mL 24% iodixanol, 2 mL of supernatant adjusted to contain 21% iodixanol, 1.5 mL of 18% iodixanol, and 3 mL of water.

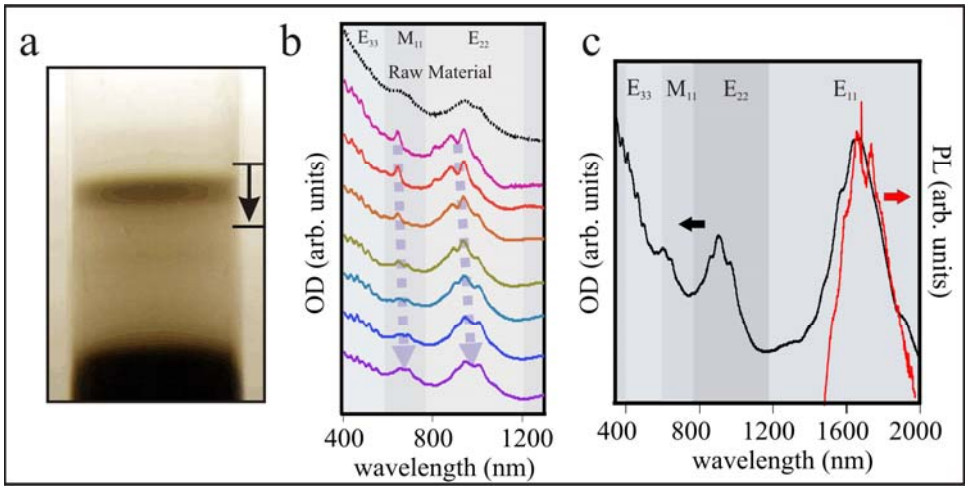

Figure 9 a. Centrifuge vial of structurally sorted laser ablation SWNT. **b.** Absorption spectra showing redshift of transitions with increasing fraction density. **c.** Absorption and fluorescence spectra of diameter enriched LA material in a gelatin matrix. The sample was excited at 980 nm for the fluorescence measurement.

After a linear gradient was formed by lying the tube on its side for 2 hrs, the suspension was centrifuged at 41 krpm for 12 hrs. A colored band was visible and fractionated into 100 μL fractions, and absorption spectra in the region of the E_{22} and M_{11} transitions show clear structural sorting by the continuous redshift in transition energies, Fig. 9 b. In order

to measure a fluorescence spectrum from the sorted material the top three fractions were mixed together and cast into a xerogel (details are given in section E). The film was excited at 980 nm with a Ti safire laser and fluorescence was measured with an extended InGaAs detector at 1750 nm, Fig. 9c.

Additional to the use of vacuum filtration thin films as semiconducting devices, flexible conductive electrodes can be fabricated by similar techniques as long as the film thickness is suitable for a metallic percolation path [Agu06, Pas05]. As a motivation, the replacement of ITO with metallic SWNT VFTF as a flexible conductive substrates could lead to devices with better efficiency and long term stability. Currently, ITO synthesized on flexible plastics have sheet resistances of a few hundred ohms per square and the flexibility is limited due to its glass-like structure. Metallic SWNT VFTF are a candidate for replacement of ITO due to their extreme flexibility and promise to have lower sheet resistances than ITO. In order for the sheet resistance to be reduced the metallic percolation path must be efficient and this can be done by removing the semiconducting tubes. As a post processing tool, DGU can be used to sort tubes by metallicity by the careful addition of co-surfactants that compete for adsorption sites on metallic tube surfaces and change the buoyant density.

Here, density gradients are prepared in the same manner as for the structural sorting of LV tubes but the gradient is loaded with 1.7% SDS and 0.3% SC instead of 2% SC. Moreover, the starting material is always sonicated with SC only. After centrifugation a blue band appears that is consistent with strong absorption in the red portion of the visible spectrum where the M_{11} transitions of LV tubes lie, Fig. 10 a. The

absorption spectrum show a clear separation by metallicity and the topmost fraction shows very little absorption from semiconducting tubes, Fig. 10 b.

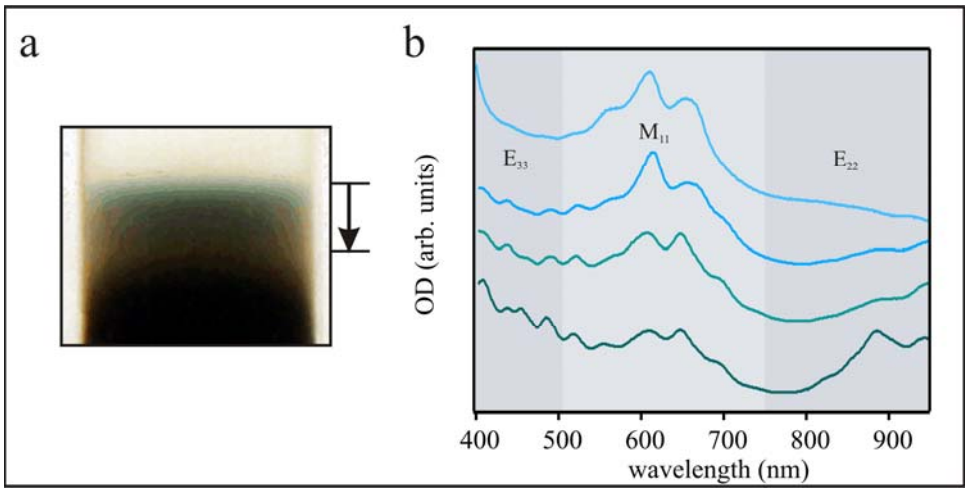

Figure 10 a. Centrifuge vial of laser ablation SWNT sorted by electronic structure. **b.** Absorption spectra showing the enhancement of the M_{11} transitions for the top most fraction.

D. Single-wall Carbon Nanotube Crystallite Engineering

The effects on intertube energy transfer and the nature of the van der Waals interaction in SWNT crystallites can best be investigated by controlling the tube composition. This can be done by first structurally or electronically sorting the tubes with DGU and aggregation by removal of the surfactant. Here, highly enriched samples of (6,5) SWNT were made by DGU with a 2% co-surfactant ratio of 4 SC: 1 SDS and a step gradient consisting of 1.5 mL of 60% iodixanol, 2.5 mL of 30% iodixanol, 1 mL of supernatant adjusted to 22.5% iodixanol, 2.5 mL of 15% iodixanol, and 3 mL of water. The resulting purple band was fractionated and placed in 3500 kD dialysis tubing and dialyzed for 24 hrs in HPCL water, Fig. 11 a. During the dialysis SWNT agglomerates

are left in the tubing as the SC and SDS is removed by osmosis. Absorption and emission spectra of the (6,5) enriched sample are shown before and after dialysis in figure 11 b. As in the case of the structurally sorted CoMoCAT from the previous chapter, the spectra are broadened and the nonresonant background is increased with respect tot the E_{22} transition which indicates crystallite formation.

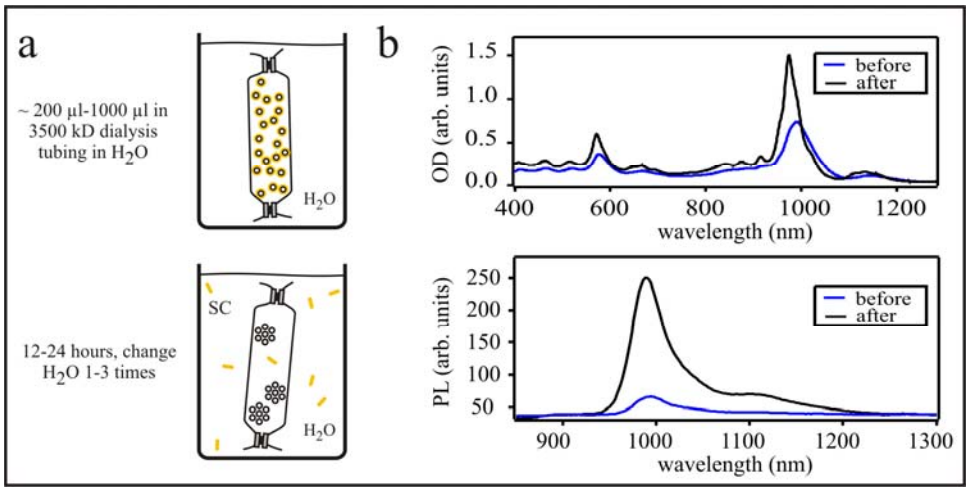

Figure 11 a. Schematic of dialysis and aggregation of tubes using dialysis tubing. **b.** Absorption (top) and photoluminescence (bottom) spectra before and after aggregation.

The newly selectively aggregated material is then re-suspended in 2% SC and placed in a step gradient identical to the staring one and centrifuged under the same conditions. A purple band reappears at the top, followed by a region similar to what was previously seen in the structural sorting of CoMoCAT (figure 6 a) , Fig. 12 a. Additionally, the absorption spectra are very similar as the spectra in figure 7 b, and are characterized by a continuous redshift in the transition wavelengths, an increase in the non-resonant background with respect to the E_{22} transition, and a broadening of the

spectral features. The uppermost fractions seemingly have an abundance of (9,1) tubes that are not present in the lower fractions. The (9,1) and (6,5) tubes has have identical diameters, therefore identical buoyant densities, but their chiral angles differ by more than 20°.

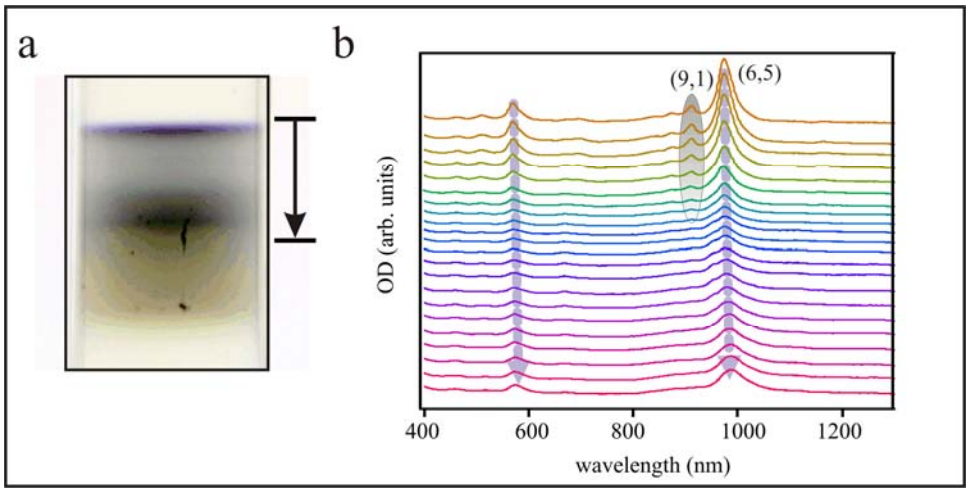

Figure 12 a. Centrifuge vial of re-suspended (6,5) enriched bundles from fig. 10. **b.** Absorption spectra of 22 fractions taken from the figure on the left with the (9,1) tube highlighted in gray.

The abundance of (9,1) tubes in the topmost fractions and its absence in the bottom can be qualitatively explained in terms the incommensurability of the two tube lattices. In simple terms, the energy per unit length $V(R,\theta,z)$ that binds two nanotubes in a crystallite is dependent on the orientation of the carbon atoms with respect to each other, where R is the magnitude of a vector describing the radial displacement from AB stacking, θ is the rotation away from AB stacking, and z is the interlayer spacing, Fig. 13. Two graphene sheets of AB stacking will maximize the binding energy at $\theta = 0$, $R = 0$, and $z = 0.344$ nm. Departures from AB stacking will lead to a change in the interlayer spacing and a corresponding reduction in the binding energy. In the case of a

perfect (6,5) crystallite the tubes can stack next to each other commensurately due to identical chiral angles which maximize the binding energy. On the other hand a (9,1) and a (6,5) tube will be incommensurate and the reduction in binding energy will not favor crystallite formation. Qualitatively, this argument explains why after re-sonication the (9,1) tubes are easier to break apart in the crystallites and why more (9,1) tubes seem to be isolated and more (6,5) tubes seem to be bundled.

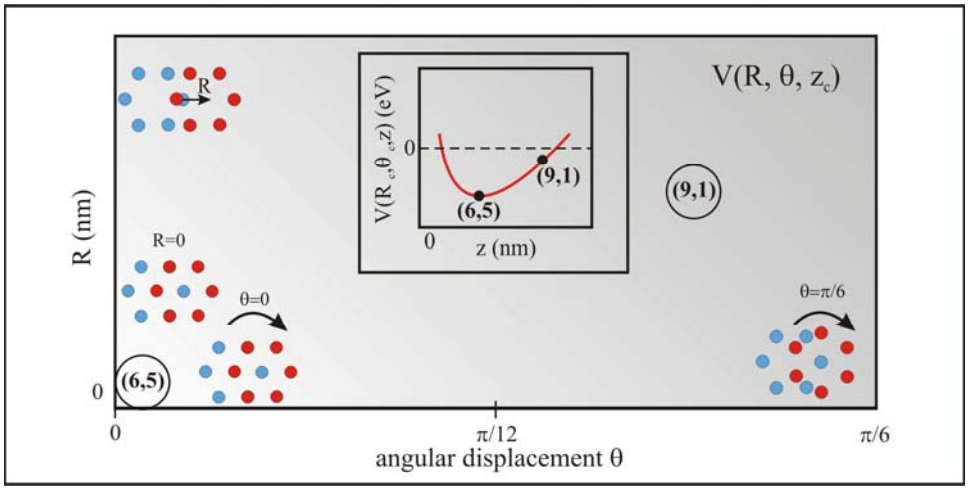

Figure 13. Schematic of the binding energy per unit length dependence on the rotational angle away from AB stacking and the radial distance away from AB stacking at a fixed intertube spacing for a tube in proximity to a (6,5) tube. The inset shows the energy dependence on intertube spacing at a fixed radial and angular displacement. The (6,5) tubes can stack together due to a maximum in the energy at (0,0) which optimizes the intertube spacing, and the (9,1) tube stacked with a (6,5) has a larger intertube spacing due to a reduced binding energy due to differing chiral angles.

E. Single-wall Carbon Nanotube Xerogels

Gelatin has been used for mechanical alignment, extended spectroscopic analysis, biological functionalization, and purification of SWNT [Kim05, Tak02, Tak04, Iak06].

This is due to its transparency from 200-3000 nm, flexible, biocompatibility, and stability under a wide range of temperatures. Here, SWNT nanotube suspensions are mixed in a ratio of 2:1 with 10% gelatin in water. The xerogels can be made with suspensions containing any of the ionic surfactants mentioned in section B. In the case of a DGU sample, the iodixanol is dialyzed away in 3500 kD dialysis tubing in a 2% surfactant bath for approximately three days. The gel is dissolved in HPCL water by heating to 100°C and cooled to above the gelation temperature (~40°C) and mixed with the SWNT suspension.

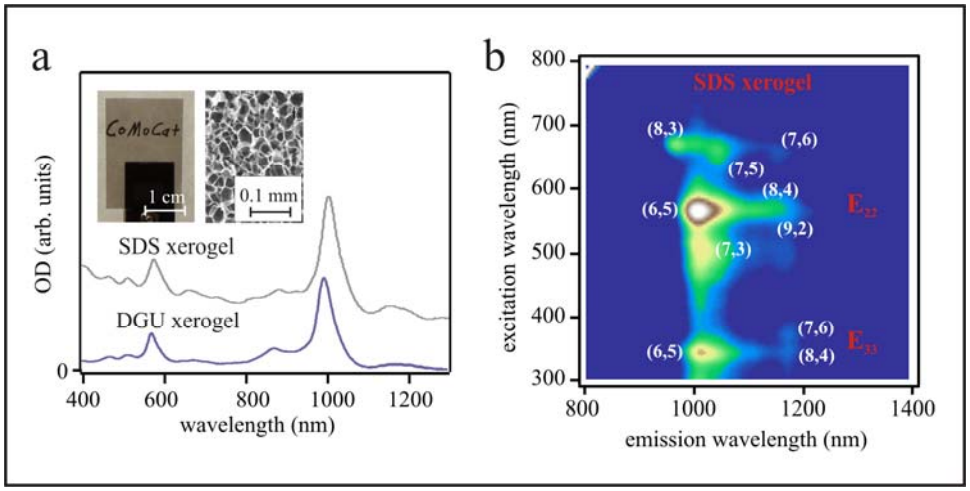

Figure 13 a. Absorption spectra of a CoMoCAT SDS suspension and the same suspension cast into a gel matrix. The bottom spectrum is from a (6,5) sample enriched by DGU. Inset: left image of a free standing CoMoCAT SDS xerogel. Right, SEM image showing the porosity of a nanotube gelatin complex [Nab05]. **b.** Photoluminescence excitation spectra of the free standing SDS xerogel on the left.

The resulting mixture is cast onto either a acetate substrate for removal or a microscope cover slide. When the SWNT/gelatin composite is allowed to dry it forms a xerogel that is semitransparent and consist of many pores that are embedded with tubes

[Nab05], Fig. 13 a inset. An absorption spectrum of a CoMoCAT SDS suspension cast into a xerogel along with a DGU enriched (6,5) xerogel is shown in figure 13 a. The xerogels are fluorescent, Fig. 13 b, and very stable unlike aqueous suspension that tend to flocculate over time. This allows for spectroscopic investigations of SWNT in vacuum or low temperatures and also can possibly used as a gas sensor due to the high porosity and surface sensitivity of carbon nanotubes [Li03, Mod03, Cho03].

F. References

[Agu06] Aguirre, C. M., S. Auvray, et al. (2006). "Carbon nanotube sheets as electrodes in organic light-emitting diodes." Applied Physics Letters 88(18).

[Arn06] Arnold, M. S., A. A. Green, et al. (2006). "Sorting carbon nanotubes by electronic structure using density differentiation." Nature Nanotechnology 1(1): 60-65.

[Arn05] Arnold, M. S., S. I. Stupp, et al. (2005). "Enrichment of single-walled carbon nanotubes by diameter in density gradients." Nano Letters 5(4): 713-718.

[Bac02] Bachilo, S. M., M. S. Strano, et al. (2002). "Structure-assigned optical spectra of single-walled carbon nanotubes." Science 298(5602): 2361-2366.

[Bo05] Bo, X. Z., C. Y. Lee, et al. (2005). "Carbon nanotubes-semiconductor networks for organic electronics: The pickup stick transistor." Applied Physics Letters 86(18).

[Bro01] Bronikowski, M. J., P. A. Willis, et al. (2001). "Gas-phase production of carbon single-walled nanotubes from carbon monoxide via the HiPco process: A parametric study." Journal of Vacuum Science & Technology a-Vacuum Surfaces and Films 19(4): 1800-1805.

[Cho03] Chopra, S., K. McGuire, et al. (2003). "Selective gas detection using a carbon nanotube sensor." Applied Physics Letters **83**(11): 2280-2282.

[Cro07] Crochet, J., M. Clemens, et al. (2007). "Quantum yield heterogeneities of aqueous single-wall carbon nanotube suspensions." Journal of the American Chemical Society 129(26): 8058-+.

[Hell04] Heller, D. A., R. M. Mayrhofer, et al. (2004). "Concomitant length and diameter separation of single-walled carbon nanotubes." Journal of the American Chemical Society 126(44): 14567-14573.

[Iak06] Iakoubovskii, K., N. Minami, et al. (2006). "IR-extended photoluminescence mapping of single-wall and double-wall carbon nanotubes." Journal of Physical Chemistry B 110(35): 17420-17424.

[Jor05] Jorio, A., C. Fantini, et al. (2005). "Resonance Raman spectroscopy (n,m)-dependent effects in small-diameter single-wall carbon nanotubes." Physical Review B 71(7).

[Jor05] Jorio, A., A. P. Santos, et al. (2005). "Quantifying carbon-nanotube species with resonance Raman scattering." Physical Review B 72(7).

[Kat99] Kataura, H., Y. Kumazawa, et al. (1999). "Optical properties of single-wall carbon nanotubes." Synthetic Metals 103(1-3): 2555-2558.

[Kim05]Kim, Y., N. Minami, et al. (2005). "Highly polarized absorption and photoluminescence of stretch-aligned single-wall carbon nanotubes dispersed in gelatin films." Applied Physics Letters 86(7).

[Kit00] Kitiyanan, B., W. E. Alvarez, et al. (2000). "Controlled production of single-wall carbon nanotubes by catalytic decomposition of CO on bimetallic Co-Mo catalysts." Chemical Physics Letters 317(3-5): 497-503.

[Kuk02] Kukovecz, A., C. Kramberger, et al. (2002). "A detailed Raman study on thin single-wall carbon nanotubes prepared by the HiPCO process." European Physical Journal B 28(2): 223-230.

[Li03] Li, J., Y. J. Lu, et al. (2003). "Carbon nanotube sensors for gas and organic vapor detection." Nano Letters **3**(7): 929-933.

[Lol06] Lolli, G., L. A. Zhang, et al. (2006). "Tailoring (n,m) structure of single-walled carbon nanotubes by modifying reaction conditions and the nature of the support of CoMo catalysts." Journal of Physical Chemistry B 110(5): 2108-2115.

[Man95] Manne, S. and H. E. Gaub (1995). "Molecular-Organization of Surfactants at Solid-Liquid Interfaces." Science 270(5241): 1480-1482.

[Mar06] Marty, L., E. Adam, et al. (2006). "Exciton formation and annihilation during 1D impact excitation of carbon nanotubes." Physical Review Letters 96(13).

[Mod03] Modi, A., N. Koratkar, et al. (2003). "Miniaturized gas ionization sensors using carbon nanotubes." Nature **424**(6945): 171-174.

[Moo03] Moore, V. C., M. S. Strano, et al. (2003). "Individually suspended single-walled carbon nanotubes in various surfactants." Nano Letters 3(10): 1379-1382.

[Nab05] Nabeta, M. and M. Sano (2005). "Nanotube foam prepared by gelatin gel as a template." Langmuir 21(5): 1706-1708.

[Nik99] Nikolaev, P., M. J. Bronikowski, et al. (1999). "Gas-phase catalytic growth of single-walled carbon nanotubes from carbon monoxide." Chemical Physics Letters 313(1-2): 91-97.

[O'Co02] O'Connell, M. J., S. M. Bachilo, et al. (2002). "Band gap fluorescence from individual single-walled carbon nanotubes." Science 297(5581): 593-596.

[Pas05] Pasquier, A. D., H. E. Unalan, et al. (2005). "Conducting and transparent single-wall carbon nanotube electrodes for polymer-fullerene solar cells." Applied Physics Letters 87(20).

[Red75] Redgrave, T. G., D. C. K. Roberts, et al. (1975). "Separation of Plasma Lipoproteins by Density-Gradient Ultracentrifugation." Analytical Biochemistry 65(1-2): 42-49.

[Rig00] Riggs, J. E., Z. X. Guo, et al. (2000). "Strong luminescence of solubilized carbon nanotubes." Journal of the American Chemical Society 122(24): 5879-5880.

[Rin98] Rinzler, A. G., J. Liu, et al. (1998). "Large-scale purification of single-wall carbon nanotubes: process, product, and characterization." Applied Physics a-Materials Science & Processing 67(1): 29-37.

[Sch00] Schuck, P. (2000). "Size-distribution analysis of macromolecules by sedimentation velocity ultracentrifugation and Lamm equation modeling." Biophysical Journal 78(3): 1606-1619.

[Tak02] Takahashi, T., K. Tsunoda, et al. (2002). "Isolation of single-wall carbon nanotube bundles through gelatin wrapping and unwrapping processes." Chemistry Letters(7): 690-691.

[Tak04] Takahashi, T., K. Tsunoda, et al. (2004). "Purification of single wall carbon nanotubes using gelatin." Japanese Journal of Applied Physics Part 1-Regular Papers Short Notes & Review Papers 43(3): 1227-1230.

[Wan96] Wanless, E. J. and W. A. Ducker (1996). "Organization of sodium dodecyl sulfate at the graphite-solution interface." Journal of Physical Chemistry **100**(8): 3207-3214.

[Wei03] Weisman, R. B. and S. M. Bachilo (2003). "Dependence of optical transition energies on structure for single-walled carbon nanotubes in aqueous suspension: An empirical Kataura plot." Nano Letters 3(9): 1235-1238.

[Zhe03] Zheng, M., A. Jagota, et al. (2003). "DNA-assisted dispersion and separation of carbon nanotubes." Nature Materials 2(5): 338-342.

CHAPTER IV

INTRATUBE ENERGY AND CHARGE TRANSFER

Photoexcitations in single-wall carbon nanotubes are one-dimensional due to the delocalization of the exciton wavefunction around the circumference of the tube and localization on the tube axis. Recent experiments show that the quantum yield of fluorescence is more than 1% and non-radiative decay channels dominate the return to the ground state. Here, spectroscopic studies of the return to the ground state are presented and shed light on the peculiarities of energy and charge transfer in one-dimensional system. Controlled defect formation suggests an ultrafast plasmon-assisted non-radiative decay channel competing with interband relaxation. In addition, the interband relaxation is found to be an efficient internal conversion that couples the E_{22} exciton to the E_{11} exciton involving a zone boundary phonon. The majority of E_{11} excitons undergo non-radiative decay through an ultrafast intersystem crossing that is facilitated through degeneracy of the lowest lying singlet exciton and its triplet counterpart. Triplets are found to return to the ground state dynamically with a power law that suggest triplet-triplet annihilation or sub-diffusive trapping.

A. (6,5) Enriched Isolated Tube Ensembles

1. Isolated Ensemble Quantum Yield and the Nonlinear Response

In order to remove spectral ambiguities associated with intertube coupling and sample inhomogeneities, spectroscopic investigations are performed on isolated (6,5) tube ensembles prepared by DGU. The quantum yield, η, of the (6,5) enriched samples are found by using LDS925, Radiant Dyes Laser & Accessories GmbH, as a dye reference. LDS925 has a quantum yield of 11% dissolved in methanol with an absorption maximum at 580 nm and emission maximum at 960 nm, Fig. 1. The (6,5) quantum yield is found to be 1.1% [Cro07] using the following relation,

$$\eta_S = \eta_R \frac{A_R}{A_S} \frac{E_S}{E_R} \frac{I_R}{I_s} \left(\frac{n_S}{n_R} \right)^2 , \tag{1}$$

where A is the absorbance, E is the corrected emission intensity, I is the excitation intensity, and n is the index of refraction of the host solvent [Wil83]. The subscripts R and S stand for reference and sample respectively. Since the excitation maximum of the (6,5) tube is at 571 nm and the excitation maximum of the LDS925 is at 580 nm the ratio of excitation intensities is taken to unity as well as the ratio of indices of refraction due to the very small difference between methanol and water in this wavelength range.

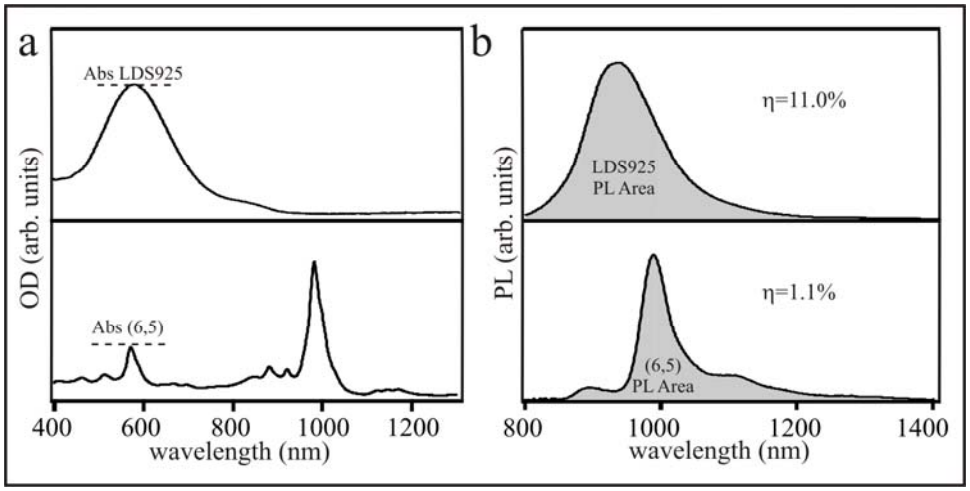

Figure 1. a. Absorption spectra of LDS925 and a DGU enriched (6,5) ensemble. **b.** Photoluminescence spectra for each sample exciting at 572 nm. The quantum yield η is calculated by comparing the relative absorbance and integrated PL intensities of each sample. The (6,5) enriched sample is found to have a quantum yield of over 1%.

The quantum yield of the DGU (6,5) enriched samples exceeds previous estimates of 0.01% by over two orders of magnitude [Wan04, O'Co02]. This improvement is due to sample homogeneity and removal of the majority of nanotube crystallites whose quantum yield is most likely reduced by additional non-radiative decay channels. A photoluminescence excitation spectrum is show in figure 2 a and illustrates the degree of homogeneity where the (6,5) tube accounts for approximately 55% of the ensemble average.

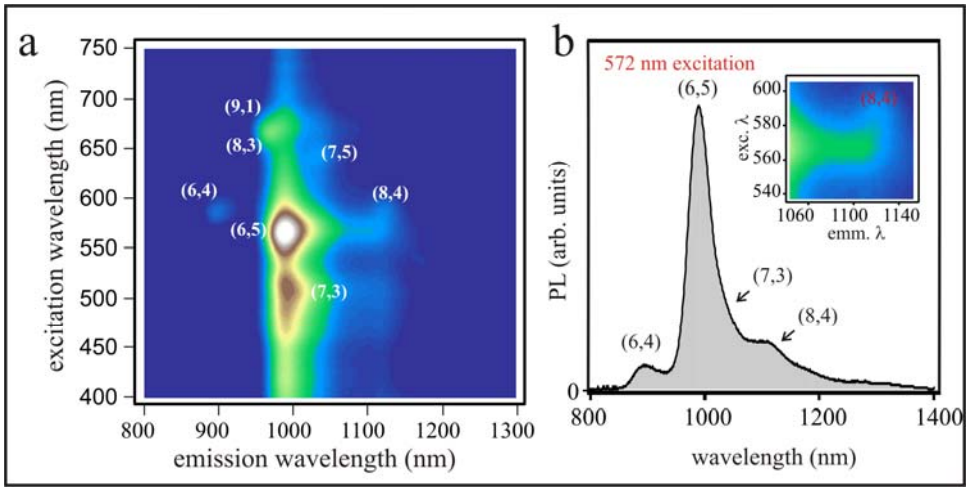

Figure 2 a. Photoluminescence excitation spectrum from the DGU (6,5) enriched sample in figure 1. The (6,5) tube makes up approximately 55% of the sample, the (7,3) approximately 20%, and the (8,3) and (6,4) approximately 15%. **b.** Emission spectrum for 572 nm excitation. The asymmetric lineshape is partly due to minority tube species, but may also contain emission from (6,5) excitons that are weakly coupled radiatively to the ground state. The inset is the region of the PLE spectrum that contains the tails of the (6,5) emission.

A quantum yield of 1% suggest that for every 100 excitons created 99 of them decay into non-radiative decay channels. These channels could be due to many different effects, such as traps associated with structural defects and the presence of dipole-forbidden states such as dark singlet and triplet excitons. An indication of the branching can be seen in the asymmetry in the line profile of the photoluminescence spectrum in figure 2 b. Minority tube species emitting at this excitation wavelength are partly responsible for the asymmetry, but can not account for the observed low energy feature. The (6,5) E_{11} emission at 988 nm is followed by a tail that extends out to 1400 nm that may be due to emission from traps, phosphorescence from triplets, or delayed fluorescence. Paired gap states arising from structural defects have been shown to have energies ranging from 20 to 480 meV depending on nature of the defect [Lee05].

Phosphorescence has not been reported to exist in SWNT, but with the advent of high quality-samples this may change.

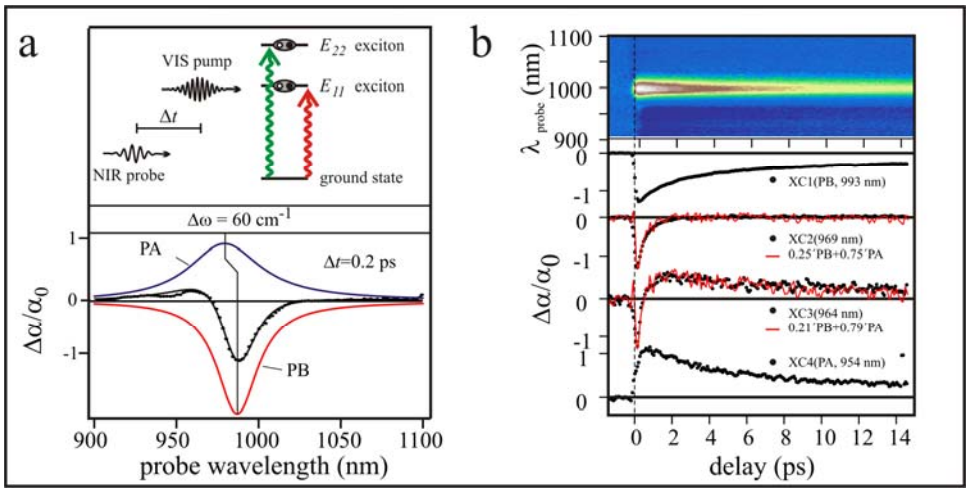

Figure 3 a. Schematic of visible pump infrared probe experiment and the transient absorption spectrum at pump probe delay of 1ps. The spectrum is a linear combination of a PB at the (6,5**)** E_{11} and a slightly blueshifted PA. **b.** Transient absorption spectra of a (6,5) DGU enriched ensemble. The E_{22} exciton is pumped resonantly and the E_{11} probed from 900-1000 nm. The top graph is a 2-D plot of transient absorption intensity versus pump probe delay and probe wavelength. The white/dark blue colors represent a negative/positive change in transmission known as a photobleach (PB)\ photoabsorption (PA). Cross correlations that are off resonance of the PA/PB can are linear combinations of the PA and PB, as shown in the bottom graphs. On resonance the PB can be attributed to a 600 fs rise time, a fast initial decay of 3.1 ps, and slow decay that last several ns. The PA has a 1 ps rise time, an initial fast decay of 5.5 ps, and a slow decay that last several ns.

Pump-probe spectroscopy of DGU (6,5) enriched samples provide an ideal platform to investigate the dynamics associated with the ground state recovery of photoexcited SWNT and the investigation of the interpretation of the pump-probe experiment. The typical conclusions drawn from two-color pump-probe experiments are based on fitting cross correlations with multi-exponentials and assigning each decay constant to a process involving intraband, interband, intertube, and excited state

relaxations [Lau03, Arn04, Kor04, Kon04, Ost04]. Additionally, most experiments are performed using HiPco material that contains many crystallites and (n,m) species. The standard interpretation is that the photobleach (PB) is recovered due to ground state filling in a combination of processes involving a fast intraband relaxation from E_{22} to E_{11} on the time scale of 1 ps and a slow interband recombination from E_{11} on the order of 10 ps. This interpretation may partially be true if excitonic effects were negligible, but to assign bulk semiconductor-like behaviors to a system whose ground state consist of a many-particle wavefunction of electrons and holes and whose excited state is molecular-like is flawed. Moreover, exciting excitons belonging to the E_{22} subband and probing excitons belonging E_{11} subband complicates the transient absorption experiment by including all possible branching possibilities from a state embedded in the e-h pair continuum of E_{11}. The photoabsorption (PA) has been interpreted to be due to either an optical Stark effect in which the exciton "feels" the free electrons and holes or a process involving two photon absorption [Mae06].

In order to compare previously published results on two-color experiments, here a DGU (6,5) enriched sample encapsulated in DNA is investigated [Zhu07]. The (6,5) tube is pumped resonantly at the E_{22} exciton and a white-light probe is used to take a two-dimensional cross correlation around the E_{11} exciton, Fig. 3. The transient spectrum at a delay of 200 fs is composed of a PB on the E_{11} exciton resonance and slightly blue-shifted PA as previously reported. The spectrum can be fit with two Voigt profiles as defined in chapter 2 , one at the resonance of 993 nm for the PB and the other blue-shifted to 954 nm. This implies that the spectrum arises from two distinct optical transitions. The dynamics are characterized by a linear superposition of PBs and PAs that

are intermediate in between the PA and PB maximum. At the PB maximum the cross correlation has a 600 fs rise time and decays in 3.1 ps into a power law relaxation of $t^{-1/2}$ that will be discussed further in section D. The PA has a 1 ps rise time and an initial decay of 5.5 ps which also relaxes into a power law recovery of $t^{-1/2}$. The differences in the rise time for the PB and PA is on the order of 400 fs and the initial decays differ by 2.4 ps, suggesting that the process responsible for the PB may be creating the state responsible for the PA. If excited-state absorption were responsible for the PA, then the interaction of the probe created excited state with the pump created excited state would produce a spectral shift. Specifically, in the case of the blue shift of the E_{11} exciton, the probe creates an exciton in which its ground state is no longer the same as the unexcited case due to the new configuration of the dielectric function in the presence of pump-created excitons. The new excitation takes approximately 400 fs to adjust to the presence of other excited states. Apart from the aforementioned speculations, the origin of the PA feature needs to be further investigated in order to shed light on its nature. In the rest of this chapter only PB effects will be used to investigate the excited state dynamics.

2. Length Enriched Quantum Yield and Defect Induced Decay Channels

The effect of defects on the optical properties of nanotubes is of scientific and industrial interest. Controlled defect formation can lead to a better understanding of how synthesis can be improved to produce high quality tube samples and how the excited state dynamics are affected by these defects. Size-exclusion chromatography is currently being used to fractionate SWNT by their length and provides the means to analyze defects in a

controlled manner [Hel04] . The end of a tube is most likely a symmetry-breaking defect originating from the presence of hydrogen passivated or oxidized dangling bonds created during sonication. Previous optical studies on length-fractionated tubes show that the non-resonant background tends to increase as the tube length gets shorter [Hua05]. The non-resonant background may be linked to tube defects or graphitic impurities that introduce a π plasmon broadening as seen in electron energy loss spectroscopy [Brz05]. Moreover, the ratio of the disorder-induced Raman peak to the tangential stretch mode increases with decreasing nanotube length, which further elucidates the role of ends in defect formation [Cho07].

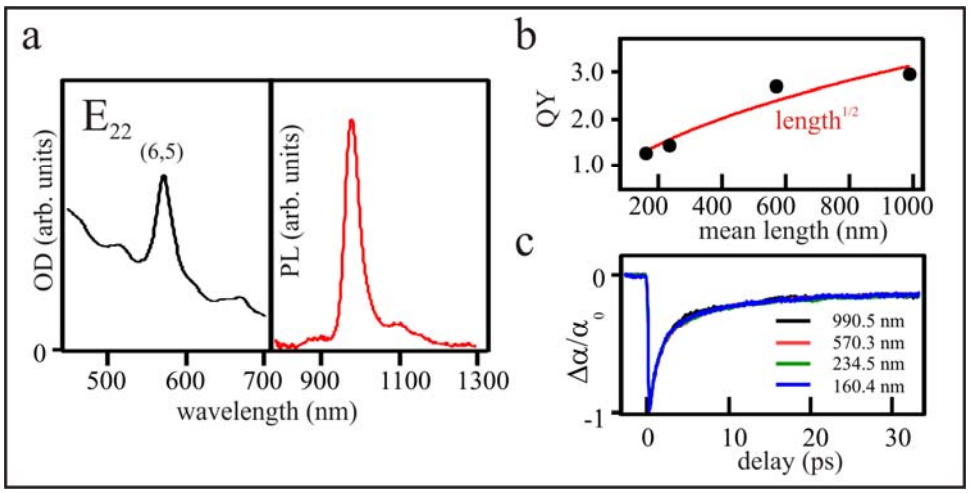

Figure 4 a. Typical visible absorption spectra for a length sorted CoMoCAT sample. **b.** The quantum yield as a function of mean length. **c**. Cross correlations of resonantly pumping the (6,5**)** E_{22} exciton and resonantly probing the (6,5**)** E_{11} exciton for each mean length in fig 4b. The dynamics attributed to a 430 fs rise time, an initial decay that of 1.9 ps, and power law long decay. Strikingly even though the quantum yield changes by nearly 50% form the shortest tubes to the longest the dynamics are unchanged.

Here, pump probe and continuous wave spectroscopy are used to investigate correlations between the photoluminescence quantum yield and the ground state recovery

of the (6,5) SWNT. Samples were prepared by size exclusion chromatography and characterized using atomic force microscopy courtesy of the M. Strano group at MIT. Four fraction were obtained that had a mean length ranging from 160.4 to 990.5 nm. A representative absorption spectra in the E_{22} range and fluorescence spectra are shown in figure 4 a. The fluorescence quantum yield was found to increase as a function of tube length and roughly scales as square root of the tube length, Fig. 4 b. The change in quantum yield is most likely due to the presence of a non-resonant background associate with a defect broadening of the π plasmon mentioned above. Therefore, a portion of absorbed light goes into the creation free electrons and holes associated with the plasmon and the rest into the E_{22} exciton. Normalized cross correlations of resonantly exciting the E_{22} exciton and probing the E_{11} exciton for each fraction, Fig. 4 c. Surprisingly, even though the quantum yield changes by over 50% from the shortest to the longest tubes the dynamics are independent of length within the experimental time resolution of 100 fs.

These findings suggest that the ground state filling on the ps time scale is not mediated by defects but an intrinsic relaxation pathway. Moreover, the effects of a broadened π plasmon are supported since the recovery time is much faster than the time resolution used in this experiment. In graphite at the excitation energy used here, 2.1 eV, the recovery is on the order of 20 fs [Xu96]. This scenario supports that the plasmon becomes an efficient non-radiative decay channel when the defect density is large and that branching of free carries into the continuum competes with exciton interband relaxation. The free carriers can decay within an upper limit of 100 fs and the interband relaxation in the form of a phonon assisted internal conversion will be discussed in the next section.

B. Internal Conversions and Free Carrier Decay Channels

In the previous section it was shown that defects reduce the quantum yield by increasing the plasmon response and introduce an efficient non-radiative decay channel. A percentage of absorbed photons will create E_{22} excitons which undergo an interband relaxation to the E_{11} exciton. Here, the microscopic mechanism responsible for the relaxation was investigated by measuring the E_{22} exciton linewidths in a HiPco sample enriched in isolated tubes by DGU. An absorption an photoluminescence excitation spectra with 23 semiconducting tube species are shown in figures 5 a and 5 b. The E_{22} exciton linewidths were analyzed by fitting the excitation spectra (vertical cuts) in the PLE spectrum with a Voigt profile using a mulitpeak fitting routine in Igor Pro 5.0.

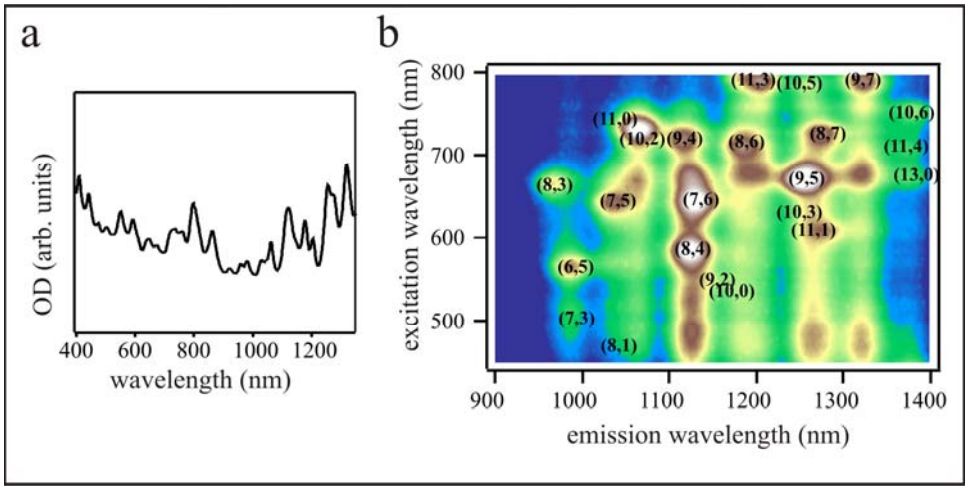

Figure 5. a. Absorption spectra of a Hipco sample enriched in isolated tubes by DGU. **b.** PLE map of the same sample with 23 species E_{22} to E_{11} transitions labeled.

The diameter and E_{22} energy dependence of the FWHM is plotted in figure 6 a. The widths range from 20-90 meV and show a clear correlation with both the tube diameter

and the E_{22} energy, which suggest a diameter dependent decay mechanism. A fraction of the linewidth is inherently to inhomogeneous broadening and is estimated to be on the order of 10 meV when the E_{11} emission data is compared to a recent study of single tubes in vacuum [Ino06].

The microscopic mechanism responsible for the diameter dependence of the linewidths was investigated with two different models of ideal infinitely long tubes: the first - an electronic mechanism in which E_{22} excitons scatter into the free e-h pair continuum of E_{11}, and the second - E_{22} excitons undergoing an internal conversion by scattering with a zone boundary phonon into the manifold of E_{11} excitons [Her07]. In the first scenario the rate of the electronic mechanism W_{el} can be approximated using the golden rule,

$$W_{el} \propto \left|\left\langle \psi_{22} \left| V_{el} \right| \psi_{e-h} \right\rangle\right|^2 \rho_{e-h}\left(h\nu_{22}\right), \tag{2}$$

where ψ_{22} is the E_{22} exciton wavefunction, ψ_{e-h} is the E_{11} e-h continuum wavefunction in which the E_{22} exciton decays, V_{el} is the electronic coupling, and ρ_{e-h} is the joint density of states of the E_{11} e-h continuum which is dependent of the excitation energy $h\nu_{22}$. If one assumes that the matrix element is independent of the tube diameter and that the rate is solely dependent of the joint density of states of the E_{11} e-h continuum at the E_{22} exciton energy, then the diameter dependence of the rate should be depend on the energy in the continuum at which the exciton is embedded. The measure of the energy in the continuum can be defined as an alignment parameter,

$$\mathrm{A} = h\nu_{22} - \Delta_{11}, \tag{3}$$

where Δ_{11} is the free e-h band gap. Recent calculations suggest that the E_{11} exciton binding energy scales linearly with the free e-h quasiparticle band gap [Cap06]. Similarly, the E_{11} exciton binding energy scales linearly with E_{11} exciton optical transition energies, and by using experimental data from two photon fluorescence [Wan05, Mau05] compared with the theoretical scaling [Cap06] the exciton binding energy scales as $E_{b,11} = 0.31 h\nu_{11}$ and the free particle gap as $\Delta_{11} = 1.31 h\nu_{11}$. Therefore, the alignment parameter is known for any species within the photoluminescence excitation spectra in figure 5. Moreover, the E_{22} exciton transition energies lie within the E_{11} free particle gap as shown in figure 6 b. Unlike the clear correlation of the E_{22} linewidth with the tube diameter the alignment parameter shows no clear correlation and suggest very little coupling of E_{22} excitons to the free carrier continuum.

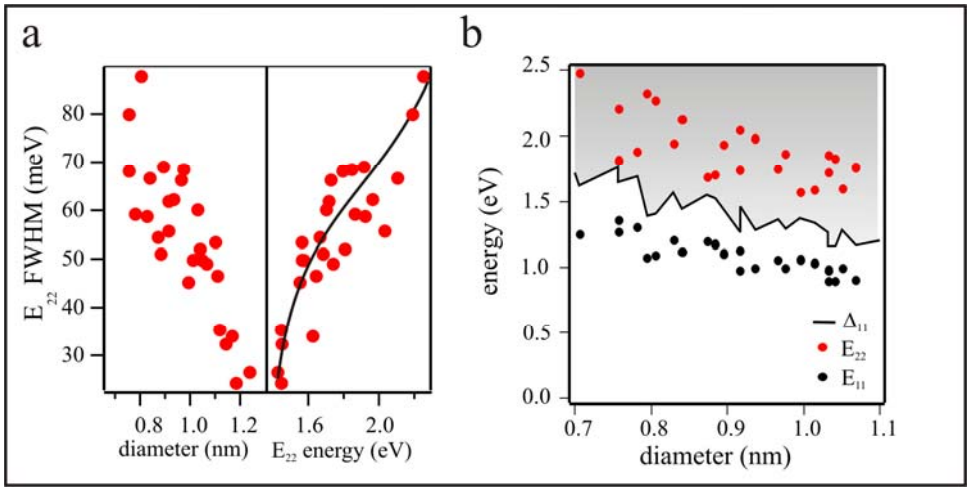

Figure 6. a. E_{22} Voigt full width half maximums as a function of tube diameter and E_{22} energy, both show clear correlations. The line is a guide to the eye. **b.** Experimental E_{11} exciton emission energy, experimental E_{22} exciton excitation energy, and theoretical E_{11} free particle gap using experimental data of line positions and theoretical data on exciton binding energies. All of the E_{22} excitons lie within the E_{11} free particle gap.

Here, the E_{22} wavefunction and are calculated using the BSE within the tight binding basis with a hopping integral $t = 3.0\,\text{eV}$. This allows for the modeling of the linewidths of the E_{22} transitions by calculating the imaginary part of the dielectric function [Per04]. It is found that the E_{22} exciton is made up of several states and a unit cell of 500 nm is used to spectrally resolve the width of the transition. In the case of the electronic relaxation, schematically given in the right side of figure 7 b, the Lorentzian linewidths show no significant correlation with experiment and are a factor of 10 narrower, Fig. 7 a. This supports the non dependency of the alignment parameter on the experimental linewidth.

The second mechanism involves scattering with a phonon that couples the E_{22} exciton to the manifold of E_{11} excitons. Involvement of a phonon lifts the momentum restriction found in the electronic mechanism that forces the initial and final states to have the same longitudinal and angular momentum. Therefore, the phonon can scatter the E_{22} exciton at the gamma point into an E_{11} exciton of finite momentum. The Su-Schriefer-Heeger model for the electron-phonon interaction is employed, with matrix element $t - g\delta R_{c-c}$, where δR_{c-c} is the change in the nearest neighbor carbon distance [Su79]. The coupling constant g is taken to be 53 eV/nm, and the exciton phonon coupling is calculated using exciton wavefunctions found from the BSE. The golden rule is then used to calculate the lifetime of each BSE state including the exciton phonon coupling [Per05-1]. The calculated spectrum is then fit with a Lorentzian and compared to the experimental data, Fig 7 a. All possible phonon modes are included and it is found the E_{22} exciton primarily decays into the doubly degenerate E_{11} exciton via a finite momentum zone boundary K optical phonon [Per05-2]. The theoretical linewidths are about 30% smaller than the experimental linewidths and may be due to thermal

broadening by acoustic phonons on the order of a few meV, but there is a clear correlation between experiment and the model, Fig. 7 a. Within the accuracy of this model and the correlation with experimental data it s found the branching ratio of E_{22} excitons that scatter into the E_{11} continuum as to the phonon assisted interband relaxation to an E_{11} dark exciton is roughly 1:10.

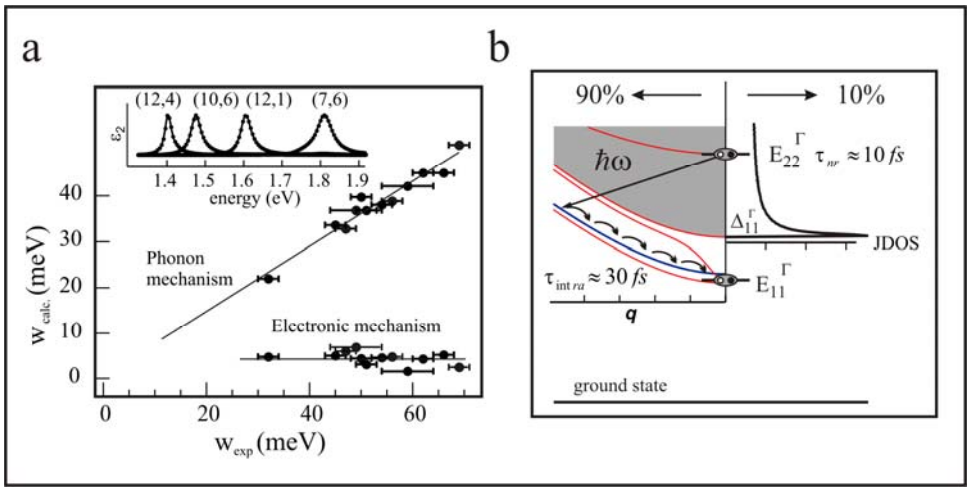

Figure 7. a. Calculated FWHM versus experimental FWHM. The phonon assisted mechanism shows a clear correlation with experiment. The inset is a plot of the calculated FWHM for a set of tubes, which illustrates the diameter dependence. **b.** A schematic of the two possible mechanisms for the internal conversion of E_{22} to E_{11} exciton. The left shows the likely process in which a zone boundary phonon is involved in scattering the E_{22} bright state into the E_{11} doubly degenerate dark state within 10 fs and the E_{11} dark state undergoes intraband relaxation within 30 fs until it thermalizes with the E_{11} bright state. The other unlikely scenario is the E_{22} bright state scatters with free e-h pairs in the E_{11} continuum and relaxes down to the E_{11} bright state by thermalization.

To put these findings in perspective, the interband relaxation found here is on the order of 10 fs , and a recent ultrafast pump probe experiment with 10 fs time resolution found the E_{22} exciton decays and the E_{11} bright exciton is photobleached within 40 fs [Man05]. This implies that after the interband relaxation to a dark exciton with finite momentum, a 30 fs intraband relaxation must take place in order for the bright exciton to

be filled with zero momentum excitons. This gives a theoretical description of the two processes that compose the 40 fs internal conversion of E_{22} energy into E_{11} bright state energy. In a molecular description, S_2 (E_{22}) undergoes an internal conversion into S_1 (E_{11} bright exciton). Moreover, the 30% difference in the linewidths calculated here and the ones found in experiment may be due to anharmonic coupling between the acoustic radial breathing mode and the tangential optical G mode [Gam06]. This in turn distorts the tube in the presence of the exciton and has been shown independently to occur in the absorption spectrum approximately 200 meV above both the E_{22} and E_{11} resonances as a phonon sideband. The same feature is found in the DGU (6,5) samples in the E_{11} range, but is not clear in the E_{22} due to the presence of other tube species.

C. Ultrafast Intersystem Crossing in One Dimension

The 40 fs internal conversion described in the previous section leads to a 90% filling of the E_{11} exciton manifold in which the two lowest lying states are in thermal equilibrium with each other [Met07]. Decay mechanisms from E_{11} can include a radiative decay γ_r and a non-radiative decay γ_{nr}. The total room temperature photoluminescence decay, $\gamma_{PL} = \gamma_r + \gamma_{nr}$, has been measured by time resolved fluorescence in both ensemble and single tubes and varies depending on the sample preparation. In the case of the ensembles, to date no one has performed an experiment to determine the PL lifetime on DGU enriched samples which have a quantum yield of orders of up to two orders of magnitude large. In spite of this, for samples containing a

mixture of majority small tube crystallites and a minority of isolated tubes, lifetimes of on the order of 10 ps have been measured [Wan04, Her05]. If one knows the quantum yield of the sample the radiative decay time can be found using $\eta = \tau_{PL}/\tau_R$. At the time of the measurement made above the quantum yields of typical sample were on the order of 0.1% to 0.01% which gives a radiative lifetime on the order of 10 to 100 ns. This also implies that the non-radiative decay of the E_{11} exciton, which can be found from $\eta = \tau_{nr}/(\tau_r + \tau_{nr})$, for these samples is on the order of 10 ps. In the case of isolated tubes on substrates PL lifetimes have been measured to be similar to that of suspensions with an increase of a factor of 2 or 3 [Hag05]. Theory has also predicted an intrinsic room temperature radiative lifetime on the order of 1 to 10 ns including the thermalization of the lowest lying dark state with the bright state [Per05-2, Spa05]. In the DGU (6,5) enriched sample used in this study the quantum yield is approximately 1% and by using the calculated intrinsic radiative lifetimes the non radiative decay should be approximately 10 ps in accordance with [Per05-2] and approximately 100 ps in accordance with [Spa05].

Here, the investigation of the non-radiative decay is determined by pump probe spectroscopy of a DGU (6,5) enriched sample. In the discussion on the theory of analyzing pump probe data in chapter 2 it was shown that the absorption coefficient is related to the filling of phase space by excitons. The dynamics of the transient absorption spectrum is proportional to the change in the absorption coefficient due to a variable delay between the pump and probe pulses. These changes are due to filling of both the ground state N_{gs} and intermediate state N_i densities $\Delta\alpha/\alpha_0 \propto -\left[1 - N_{gs}(t) - N_i(t)\right]$.

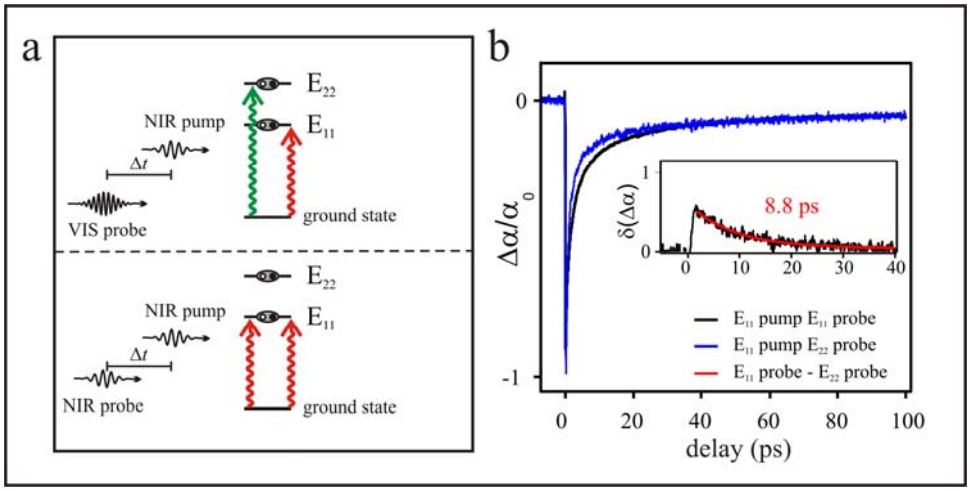

Figure 8 a. Schematic of pump probe scheme used to determine the time sale of the non-radiative lifetime of the E_{11} exciton. The filling of the ground state is determined by exciting the E_{11} exciton and probing the PB of the E_{22} exciton. A convolution of ground state filling and excited state dynamics is determined by exciting the E_{11} exciton and probing the PB of the E_{11} exciton. By the subtracting the two cross correlations that are normalized at time scale in which the exited state has decayed gives the non-radiative lifetime of the E_{11} exciton. **b.** Cross correlations observed in a DGU (6,5) enriched sample for the scheme in **a**. The non-radiative lifetime found by subtraction is in the inset.

Resonantly pumping the E_{11} exciton and probing E_{22} exciton at low fluences, $8x10^{13}$ photons/cm^2, the dynamics of the ground state filling is probed due to the absence of carriers produced by the pump pulse at the E_{22} energy, top of Fig. 8 a. Therefore the transient absorption reduces to $\Delta\alpha/\alpha_0 \propto -\left(1 - N_{gs}\right)$, and the cross correlation for this pump-probe configuration is given in figure 8 b in blue. Degenerately pumping and probing the E_{11} exciton the dynamics of the ground state filling and the excited E_{11} exciton are probe since the filling intermediate state in equation 3 is due to the lifetime of the E_{11} exciton. The cross correlation for the degenerate configuration is shown in black in figure 8 b. Both cross correlations are characterized by an initial fast decay and a slow power law decay that is identical in both.

If one assumes that after the initial decay of both of the cross correlations follow the same dynamics, which is evident for the identical dynamics at pump-probe delays greater than 40 ps, then by normalizing the cross correlations at large delays and subtracting the two should give direct access to the lifetime of the E_{11} exciton. The normalization at long times is valid in the realm that one and the same decay mechanisms are responsible for the slow recovery of the ground state and therefore the populations should be identical in each pump probe configuration. After normalization from 80 to 100 ps the slow tail of the cross correlations are identical from approximately 40 ps , Fig 8 b, to 1 ns, not shown. Using the difference of the two transient spectrum $\delta(\Delta\alpha) = CN_i$ the decay of the E_{11} exciton is found to be 8.8 ps, shown in the inset of figure 8 b. Since the quantum yield of this sample is only 1% this decay must reflect the non-radiative decay since it is on the order of what one would expect for a radiative lifetime of 1 ns. Additionally, if the quantum yield is used along with the experimental decay time the radiative lifetime approximately 870 ps which is in agreement with Perbeinos [Per05-2].

This ultrafast decay shown here is not surprising since the bright exciton is in thermal equilibrium with the lower lying dark exciton which is energetically degenerate with its triplet counterpart, and the bright exciton singlet-triplet splitting is on the order of 70 meV [And06, Spa06, Cap07], Fig. 9 a. Moreover, $\pi - \sigma$ hybridization in SWNT may be responsible for the large changes in the free particle gap from the π electron model and even though spin orbit coupling is small relatively short spin diffusion lengths can be accounted for by spin orbit coupling [And00, Chi04]. Assuming that the non-radiative decay is facilitated by an ISC between the bright exciton as $|S_1\rangle$ and its triplet counterpart $|T_1\rangle$ the rate of ISC can be calculated using the Golden rule,

$$W_{ISC} = \frac{2\pi}{\hbar}\left|\langle T_1 | H_{SO} | S_1 \rangle\right|^2 \rho_T(E_{11}), \tag{3}$$

where H_{SO} is the spin orbit operator with an expectation value of Δ_{SO} and ρ is the density of triplet states at the energy of E_{11} bright exciton. The singlet and triplet spatial wavefunctions are identical except for their spin component which in the singlet case is $|\uparrow\downarrow\rangle - |\downarrow\uparrow\rangle$ and with an electron or hole spin flip by H_{SO} the triplets can either be $|\uparrow\uparrow\rangle$ or $|\downarrow\downarrow\rangle$.

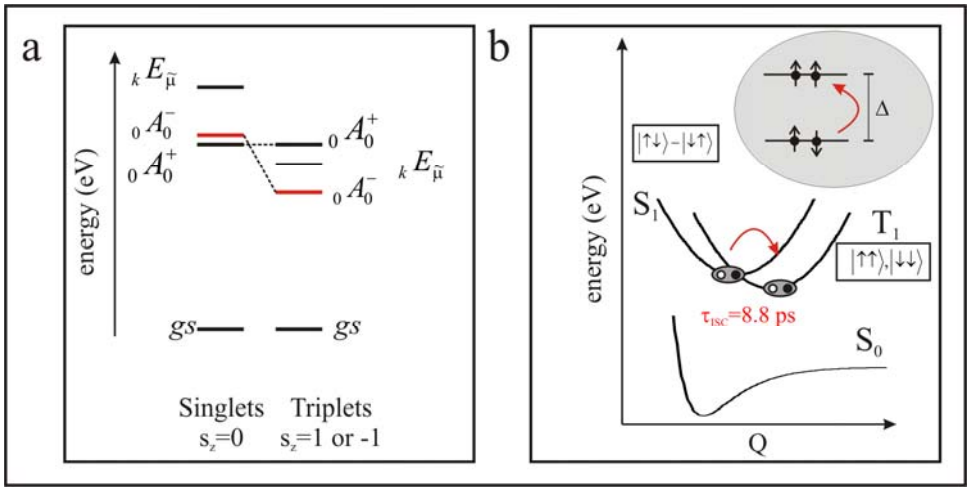

Figure 9 a. Ordering of the singlet and triplet states in chiral SWNT. Triplets that are formed by a flip of either an electron or hole spin can either have a spin projection of +1 or –1. In the (6,5) tube the bright singlet-triplet splitting is approximately 70 meV and the dark singlet-triplet are degenerate . The splitting between the lowest bright and dark singlets is on the order of a few meV and therefore they are in thermal equilibrium with each other. **b.** Schematic of the mechanism responsible for the observed ultrafast intersystem crossing. The spin orbit coupling facilitates an allowed crossing between the potential energy surfaces associated with each exciton.

The joint density of states associated with the triplets at the E_{11} exciton energy can be estimated from the consideration that the E_{11} free particle band structure of carbon nanotubes is derived from slicing the Dirac cone such that $\varepsilon_k = \pm\hbar v_F \left(k^2 + k_0^2\right)^{1/2}$. The

Fermi velocity v_F is approximated from a recent measurement on graphene as 1 $\mu m/s$ [Zha05], and k_0 is a momentum offset related to the band gap by $\varepsilon_g = 2\hbar v_F k_0$. By cutting the Dirac cone the density of states of a tube of length *L* including the 4 fold degeneracy associated with K and K′ is,

$$\rho(\varepsilon) = \frac{dN}{d\varepsilon} = \frac{4L}{\pi|\nabla_k \varepsilon|}, \tag{5}$$

where $\nabla_k \varepsilon = \hbar v_F k / \left(k^2 + k_0^2\right)^{1/2}$. Substituting the momentum with energy leads to the well know Van hov Singularities in the DOS such that $\rho(\varepsilon) = 4L\varepsilon / \left(\hbar \pi v_F \sqrt{\varepsilon^2 - \varepsilon_g^2/4}\right)$. The energy ε is then evaluated at $\varepsilon_g/2 + \delta_{S-T}$, where $\delta_{S-T} = 70\,\text{meV}$ [Cap07], which gives approximately 1.8 excitons/meV. With this JDOS and the ISC time measured of 8.8 ps implies the strength of the spin orbit interaction is found to be approximately 0.95°K. An error of 10% can be associated with this value due to the uncertainty in the DOS that comes from assuming 100% of the e-h pairs contribute to the exciton DOS when in reality approximately 90% do. This value is larger than the value of the intrinsic spin-orbit interaction calculated in graphene including π and σ orbitals, $\Delta_{\text{int}} \approx 10°\text{mK}$, but what is estimated as the interaction strength in nanotubes, $\Delta_R \approx 1°\text{K}$, where π and σ hybridization may be even more important due to curvature effects [Min06, Hue06].

In terms of a molecular picture the potential energy surfaces associated with the excited singlet and triplet states cross in configuration space at the conical intersection. The crossing is facilitated by and the flipping of a spin of the electron or hole that makes up the exciton in the presence of spin-orbit coupling, Fig. 9 b. Moreover, the large density of states of the triplets at E_{11} promotes the ISC in spite of a relatively small spin-

orbit coupling. With these effects in consideration, triplet formation overcomes the radiative decay by almost a factor of 100 and leads to tubes with many long lived states which have been experimentally observed but not assigned as triplets [Gad06].

D. Triplet Excitons and the Ground State Recovery

Following the 8.8 ps decay in figure 9 the ground state recovery follows a power law decay of $t^{-1/2}$. This power law decay is the same for all configurations of the pump probe experiment including excitation at E_{22} or E_{11} and probing E_{11} or E_{22} or vice versa, Fig. 10 a. The fast ISC crossing time results in tubes with many triplet states that have either +1 or -1 spin projections due to a spin flip of an electron or hole that affect the return to the ground state. Triplet-triplet annihilation has been studied in conjugated polymers and leads to delayed fluorescence that accounts for a small fraction of the total emission [Par99]. To date their has been no report of phosphorescence from SWNT, but with the advent of high quantum yield samples this may change.

The nature of the power law decay can be determined by considering different types of diffusion limited reactions in one dimension [Tou83]. The delocalization of the exciton wavefunction along the circumference of the tube and the high aspect ratio provides the grounds for a one dimension space [Spa04, Per04]. In the case of similar species that react to form another species such that $A + A = B$ the survival probability scales as $t^{-1/4}$, which is not found here. Another possibility is that a particle and antiparticle, given by the spin up and spin down triplets, react to form a new species such that $A + \overline{A} = C$. If the potential that causes the interaction between the triplets is of the

form of a double well localized on the tube then the survival probability scales as $t^{-1/2}$, and if it is periodic along the tube then survival probability scales as $t^{-1/4}$. Therefore, in SWNT +1 and -1 triplets may locally deform the tube [Per05-1] and attract each other through a double well deformation potential. The triplets may then annihilate each other and form an excited singlet or triplet state and repopulate the singlet ground state such that, $T_1^{\uparrow} + T_1^{\downarrow} = T_n / S_1 + S_0$, Fig. 10 b. If a newly created singlet exciton was present after such a reaction a weak delayed fluorescence signal may arise and there is some evidence of this from a recent time-correlated single photon counting experiment [Jon05].

Additional to triplet-triplet annihilation, the survival probability of a particle in a one dimensional disordered systems undergoing sub-diffusive trapping scales as $t^{-\gamma}$ where $0 < \gamma < 1$, and t^{-1} would correspond to Fickian diffusion [Yus04]. This scaling can also explain the observed dynamics where the mean square of the displacement of a triplet exciton encountering static traps would be $\left\langle r^2(t) \right\rangle \propto t^{-1/2}$. Once the triplet is trapped it must decay within 10 ps in order to preserve the non-exponential behavior of the ground state recovery. The nature of the traps could be anything from the presence of molecular oxygen to lattice defects. If oxygen was responsible, SWNT could be important for the production of singlet oxygen through triplet quenching of native oxygen in its triplet ground state. The oxygen may collide with the dense triplet exciton tube surface and through electron exchange the oxygen may be excited to its singlet excited state demoting the exciton to its singlet ground state [Kaw67]. Moreover, it has been shown that singlet oxygen can bind to nanotube surface forming an endoperoxide which can cause photobleaching when protonated due to hole doping that introduces an additional non-radiative decay channel [Duk04].

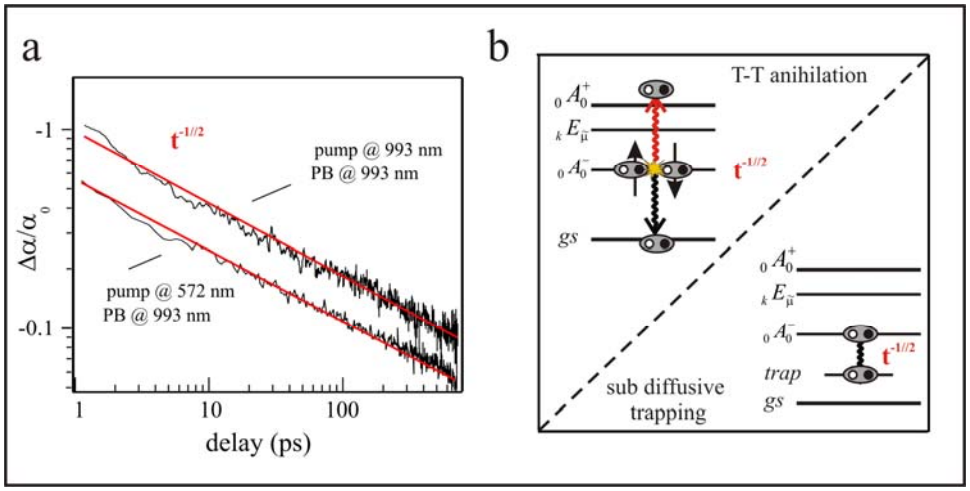

Figure 10 a. Cross correlations from 10 ps-700 ps for pumping either resonance with the E_{11} or E_{22} exciton and probing the E_{11} exciton. The ground state recovery scales with time as a power law of $t^{-1/2}$ after the initial non-radiative decay. **b.** Possible mechanisms responsible for the observed dynamics include triplet-triplet annihilation and sub-diffusive trapping. In one dimension both processes scale as $t^{-1/2}$.

E. Summary of the Intratube Relaxation Mechanisms

The investigation of intratube energy transfer has revealed the peculiarity of exciton dynamics in isolated SWNT and their one dimensional nature, Fig. 11. Upon creation 90% of the E_{22} excitons undergo an internal conversion within 10 fs by scattering into the E_{11} exciton manifold by the emission of an optical phonon. The other 10% scatter into the E_{11} continuum of electrons and holes then decay non-radiatively. Branching of the E_{22} exciton is the first evidence of how a SWNT are in the middle of the extremes of aromaticity. In benzene higher lying excitations undergo internal conversions by the emission of phonons, while in graphene allowed optical transitions scatter off of the free e-h pair continuum. The large oscillator strength of the E_{11} exciton allows for most of the E_{22} excitons to populate the E_{11} manifold which is unique to the

dimensionality of the tube. It takes approximately 30 fs for an intraband relaxation to occur from the dark exciton with finite momentum to the zero momentum thermalized lowest lying dipole allowed and forbidden excitons..

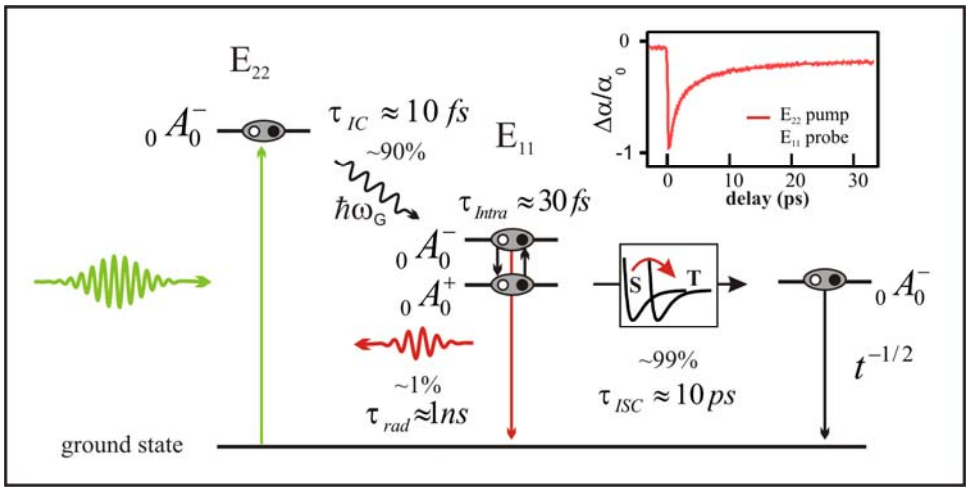

Figure 11. Summary of the relaxation pathway after excitation of the E_{22} exciton. The E_{22} exciton undergoes an internal conversion via a zone boundary phonon within 10 fs into the E_{11} dark exciton. After a 30 fs interband relaxation the E_{11} dark exciton thermalizes with the E_{11} bright exciton. Approximately 1% of the thermal zed dark/bright excitons undergo radiative decay while the other 99% are coupled to the symmetric triplet partner of the dark singlet state by a spontaneous intersystem crossing that takes place in 10 ps. The triplets then decay by sub-diffusive trapping or +1 triplet and –1 triplet annihilation that scales as $t^{-1/2}$. The inset is a cross correlation of an E_{22} pump E_{11} probe that contains a convolution of all of the processes mentioned.

Of the 90% of initially created excitons only 1% decay radiatively and the other 99% undergo an intersystem crossing to the symmetric triplet partner of the lowest lying dark exciton. The radiative decay is on the order of 1 ns and the non-radiative decay on the order of 10 ps. The ISC is facilitated by the large density of states of the triplet excitons due to reduced dimensionality and a spin-orbit coupling strength of

approximately 1 °K. Finally, the newly formed triplet excitons decay by triplet-triplet annihilation or sub-diffusive trapping indicative of the power law decay of $t^{-1/2}$.

Moreover, here the interpretation of the visible pump infrared probe experiment is much different then previous notions of multiple processes leading to multi-exponential fits, Fig. 10 inset. According to previous interpretations one would not even observe a signal while pumping in the infrared and probing in the visible. It was shown that a typical visible pump infrared probe experiment contains information on all of the processes mentioned above, and furthermore for length fractionated material that showed a change in the quantum yield of over 50% from the shortest to the longest the dynamics of the two color experiment were identical. The visible pump infrared probe experiment can be used to place an upper bound on a decay times and possible investigate solvation dynamics, but exact microscopic decay mechanism must be probed in the simplest configuration that elude intermediate decay channels. In the next chapter the amplitude of the transient absorption signal along with correlations between quantum yield and initial decays will shed light on the nature of additional non-radiative decay channels induced by intertube interactions.

F. References

[And00] Ando, T. (2000). "Spin-orbit interaction in carbon nanotubes." Journal of the Physical Society of Japan **69**(6): 1757-1763.

[And06] Ando, T. (2006). "Effects of valley mixing and exchange on excitons in carbon nanotubes with Aharonov-Bohm flux." Journal of the Physical Society of Japan **75**(2).

[Arn03] Arnold, M. S., J. E. Sharping, et al. (2003). "Band gap photobleaching in isolated single-walled carbon nanotubes." Nano Letters **3**(11): 1549-1554.

[Brz05] Brzhezinskaya, M. M., E. M. Baitinger, et al. (2005). "Investigation of the initial stages of defect formation in carbon nanotubes under irradiation with argon ions." Physics of the Solid State **47**(4): 772-777.

[Cap06] Capaz, R. B., C. D. Spataru, et al. (2006). "Diameter and chirality dependence of exciton properties in carbon nanotubes." Physical Review B **74**(12).

[Cap07] Capaz, R. B., C. D. Spataru, et al. (2007). "Excitons in Carbon Nanotubes: Diameter and Chirality Trends." Physica Status Solidi B **244**, 4016-4020.

[Cav96] Cavaleri, J. J., K. Prater, et al. (1996). "An investigation of the solvent dependence on the ultrafast intersystem crossing kinetics of xanthone." Chemical Physics Letters **259**(5-6): 495-502.

[Chi04] Chico, L., M. P. Lopez-Sancho, et al. (2004). "Spin splitting induced by spin-orbit interaction in chiral nanotubes." Physical Review Letters **93**(17).

[Cho07] Chou, S. G., H. Son, et al. (2007). "Length characterization of DNA-wrapped carbon nanotubes using Raman spectroscopy." Applied Physics Letters **90**(13).

[Cro07] Crochet, J., M. Clemens, et al. (2007). "Quantum yield heterogeneities of aqueous single-wall carbon nanotube suspensions." Journal of the American Chemical Society **129**(26): 8058-+.

[Duk04] Dukovic, G., B. E. White, et al. (2004). "Reversible surface oxidation and efficient luminescence quenching in semiconductor single-wall carbon nanotubes." Journal of the American Chemical Society **126**(46): 15269-15276.

[Gad06] Gadermaier, C., E. Menna, et al. (2006). "Long-lived charged states in single-walled carbon nanotubes." Nano Letters **6**(2): 301-305.

[Gam06] Gambetta, A., C. Manzoni, et al. (2006). "Real-time observation of nonlinear coherent phonon dynamics in single-walled carbon nanotubes." Nature Physics **2**(8): 515-520.

[Hag05] Hagen, A., M. Steiner, et al. (2005). "Exponential decay lifetimes of excitons in individual single-walled carbon nanotubes." Physical Review Letters **95**(19).

[Hel04] Heller, D. A., R. M. Mayrhofer, et al. (2004). "Concomitant length and diameter separation of single-walled carbon nanotubes." Journal of the American Chemical Society **126**(44): 14567-14573.

[Her05] Hertel, T., A. Hagen, et al. (2005). "Spectroscopy of single- and double-wall carbon nanotubes in different environments." Nano Letters **5**(3): 511-514.

[Her07] Hertel, T., V. Perebinos et al. (2007). "Intersubband decay of 1-D exciton resonances in carbon nanotubes." Nano Letters In press.

[Hua05] Huang, X. Y., R. S. McLean, et al. (2005). "High-resolution length sorting and purification of DNA-wrapped carbon nanotubes by size-exclusion chromatography." Analytical Chemistry **77**(19): 6225-6228.

[Hue06] Huertas-Hernando, D., F. Guinea, et al. (2006). "Spin-orbit coupling in curved graphene, fullerenes, nanotubes, and nanotube caps." Physical Review B **74**(15).

[Ino06] Inoue, T., K. Matsuda, et al. (2006). "Diameter dependence of exciton-phonon interaction in individual single-walled carbon nanotubes studied by microphotoluminescence spectroscopy." Physical Review B **73**(23).

[Jon05] Jones, M., C. Engtrakul, et al. (2005). "Analysis of photoluminescence from solubilized single-walled carbon nanotubes." Physical Review B **71**(11).

[Kaw67] Kawaoka, K., A. U. Khan, et al. (1967). "Role of Singlet Excited States of Molecular Oxygen in Quenching of Organic Triplet States." Journal of Chemical Physics **46**(5): 1842-&.

[Kon04] Kono, J., G. N. Ostojic, et al. (2004). "Ultra-fast optical spectroscopy of micelle-suspended single-walled carbon nanotubes." Applied Physics a-Materials Science & Processing **78**(8): 1093-1098.

[Kor04] Korovyanko, O. J., C. X. Sheng, et al. (2004). "Ultrafast spectroscopy of excitons in single-walled carbon nanotubes." Physical Review Letters **92**(1).

[Lau03] Lauret, J. S., C. Voisin, et al. (2003). "Ultrafast carrier dynamics in single-wall carbon nanotubes." Physical Review Letters **90**(5).

[Lee05] Lee, S., G. Kim, et al. (2005). "Paired gap states in a semiconducting carbon nanotube: Deep and shallow levels." Physical Review Letters **95**(16).

[Lia00] Liang, W. Z., X. J. Wang, et al. (2000). "Electronic structures and optical properties of open and capped carbon nanotubes." Journal of the American Chemical Society **122**(45): 11129-11137.

[Mae06] Maeda, A., S. Matsumoto, et al. (2006). "Gigantic optical stark effect and ultrafast relaxation of excitons in single-walled carbon nanotubes." Journal of the Physical Society of Japan **75**(4).

[Man05] Manzoni, C., A. Gambetta, et al. (2005). "Intersubband exciton relaxation dynamics in single-walled carbon nanotubes." Physical Review Letters **94**(20).

[Mau05] Maultzsch, J., R. Pomraenke, et al. (2005). "Exciton binding energies in carbon nanotubes from two-photon photoluminescence." Physical Review B **72**(24).

[Met07] Metzger, W. K., T. J. McDonald, et al. (2007). "Temperature-dependent excitonic decay and multiple states in single-wall carbon nanotubes." Journal of Physical Chemistry C **111**(9): 3601-3606.

[Min06] Min, H., J. E. Hill, et al. (2006). "Intrinsic and Rashba spin-orbit interactions in graphene sheets." Physical Review B **74**(16).

[Nan00] Nandi, N., K. Bhattacharyya, et al. (2000). "Dielectric relaxation and solvation dynamics of water in complex chemical and biological systems." Chemical Reviews **100**(6): 2013-2045.

[Nyg99] Nygard, J., D. H. Cobden, et al. (1999). "Electrical transport measurements on single-walled carbon nanotubes." Applied Physics a-Materials Science & Processing **69**(3): 297-304.

[O'co02] O'Connell, M. J., S. M. Bachilo, et al. (2002). "Band gap fluorescence from individual single-walled carbon nanotubes." Science **297**(5581): 593-596.

[Ost04] Ostojic, G. N., S. Zaric, et al. (2004). "Interband recombination dynamics in resonantly excited single-walled carbon nanotubes." Physical Review Letters **92**(11).

[Par99] Partee, J., E. L. Frankevich, et al. (1999). "Delayed fluorescence and triplet-triplet annihilation in pi-conjugated polymers." Physical Review Letters **82**(18): 3673-3676.

[Per04] Perebeinos, V., J. Tersoff, et al. (2004). "Scaling of excitons in carbon nanotubes." Physical Review Letters **92**(25).

[Per05-1] Perebeinos, V., J. Tersoff, et al. (2005). "Effect of exciton-phonon coupling in the calculated optical absorption of carbon nanotubes." Physical Review Letters **94**(2).

[Per05-2] Perebeinos, V., J. Tersoff, et al. (2005). "Radiative lifetime of excitons in carbon nanotubes." Nano Letters **5**(12): 2495-2499.

[She05] Sheng, C. X., Z. V. Vardeny, et al. (2005). "Ultrafast exciton dynamics in isolated single-walled nanotubes." Synthetic Metals **155**(2): 254-257.

[Spa04] Spataru, C. D., S. Ismail-Beigi, et al. (2004). "Quasiparticle energies, excitonic effects and optical absorption spectra of small-diameter single-walled carbon nanotubes." Applied Physics a-Materials Science & Processing **78**(8): 1129-1136.

[Spa05] Spataru, C. D., S. Ismail-Beigi, et al. (2005). "Theory and ab initio calculation of radiative lifetime of excitons in semiconducting carbon nanotubes." Physical Review Letters **95**(24).

[Su79] Su, W. P., J. R. Schrieffer, et al. (1979). "Solitons in Polyacetylene." Physical Review Letters **42**(25): 1698 LP - 1701.

[Tou83] Toussaint, D. and F. Wilczek (1983). "Particle Antiparticle Annihilation in Diffusive Motion." Journal of Chemical Physics **78**(5): 2642-2647.

[Wan04] Wang, F., G. Dukovic, et al. (2004). "Time-resolved fluorescence of carbon nanotubes and its implication for radiative lifetimes." Physical Review Letters **92**(17).

[Wan05] Wang, F., G. Dukovic, et al. (2005). "The optical resonances in carbon nanotubes arise from excitons." Science **308**(5723): 838-841.

[Wil83] Williams, A. T. R., S. A. Winfield, et al. (1983). "Relative Fluorescence Quantum Yields Using a Computer-Controlled Luminescence Spectrometer." Analyst **108**(1290): 1067-1071.

[Xu96] Xu, S., J. Cao, et al. (1996). "Energy dependence of electron lifetime in graphite observed with femtosecond photoemission spectroscopy." Physical Review Letters **76**(3): 483-486.

[Yan05] Yang, J. P., M. M. Kappes, et al. (2005). "Femtosecond transient absorption spectroscopy of single-walled carbon nanotubes in aqueous surfactant suspensions: Determination of the lifetime of the lowest excited state." Physical Chemistry Chemical Physics **7**(3): 512-517.

[Yus04] Yuste, S. B. and L. Acedo (2004). "Some exact results for the trapping of subdiffusive particles in one dimension." Physica a-Statistical Mechanics and Its Applications **336**(3-4): 334-346.

[Zha05] Zhang, Y. B., Y. W. Tan, et al. (2005). "Experimental observation of the quantum Hall effect and Berry's phase in graphene." Nature **438**(7065): 201-204.

[Zhu07] Zhu, Z. P., J. Crochet, et al. (2007). "Pump-probe spectroscopy of exciton dynamics in (6,5) carbon nanotubes." Journal of Physical Chemistry C **111**(10): 3831-3835.

CHAPTER V

INTERTUBE ENERGY AND CHARGE TRANSFER

Single-wall carbon nanotubes bind to each other due to relatively strong van der Waals interactions. These interactions cause nanotube crystallites to form, which can be composed of many different (n,m) species. Here, isolated tubes are shown to have a larger quantum yield than crystallites, and by controlling the composition through synthesis or crystallite engineering the mechanisms of intertube coupling can be investigated. The changes in quantum yield are found to be accompanied by an increase of the non-radiative decay, and it is also found that the dielectric environment within a crystallite changes the dimensionality of the screening of the Coulomb interaction between electrons and holes. Moreover, the intersystem crossing from the singlet to triplet manifold of excitons is also affected by this screening. In crystallites ultrafast electron transfer to semiconducting tubes and energy transfer to metallic tubes lead to a quenching of photoluminescence and in loosely bound aggregates exciton energy transfer leads fluorescence energy transfer. It is also shown that the ground-state recovery deviates from the pure one-dimensional models and sheds light on the mechanisms of triplet diffusion in nanotube crystallites.

A. Structurally Sorted (6,5) Enriched Crystallites

In chapter 3 it was shown that a majority of the particulates that are in the supernatant after ultracentrifugation are small tube crystallites that can contain anywhere from two to approximately seven tubes. Also, it was shown that density gradient ultracentrifugation can be used to sort crystallites by their structure, where a crystallite of seven tubes has the largest density and isolated tubes have the smallest density. The absorption spectra of the crystallites tend to have a non-resonant background that increases with crystallite size and simultaneously the photoluminescence gets weaker and crystallites containing more than approximately 5.5 tubes no longer fluoresce, Fig. 1 a. By measuring the optical density at the (6,5) E_{22} transition and the integrated photoluminescence intensity, the quantum yield as a function of crystallite size is found to decrease as the crystallite size increases, Fig. 1 b. The quantum yield changes from 1.1% in isolated tubes to 0%, within the instrumental resolution. Measured fraction densities along with the AFM data were used to calculate the estimated crystallite size for particular fraction, Fig. 1 c.

It was also shown in chapter 3 that by using highly purified (6,5) ensembles, crystallites composing mostly (6,5) tubes could be engineered and that other tube species tend to be more isolated due to the different van der Waals interactions between dissimilar SWNT lattices. The quantum yield of the highly enriched (6,5) crystallites as a function size also was found to decrease in a similar manner as in figure 1 b. The focus of the rest of this chapter is to try to understand why the quantum yield of a crystallite is lower than in isolated tubes, to determine the dynamics of intratube energy transfer, and

search for correlations between the observed dynamics and quantum yield for a particular crystallite structure.

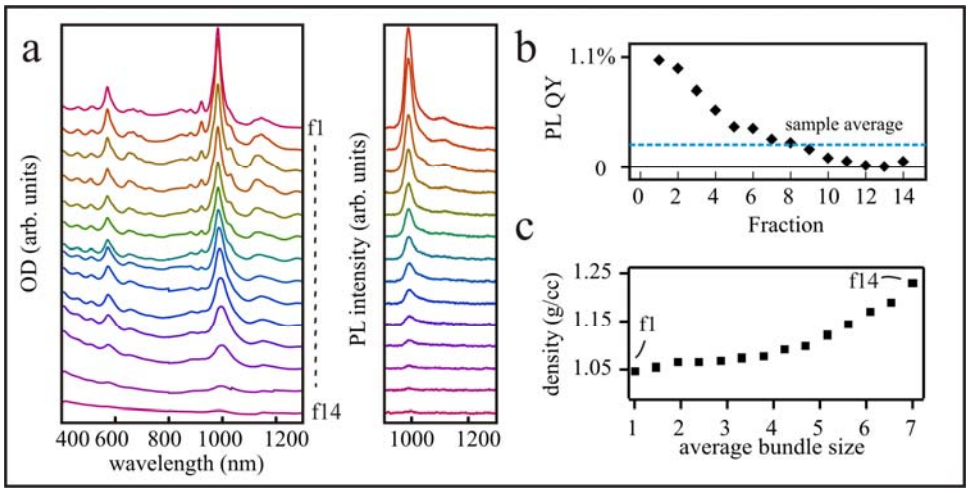

Figure 1 a. Absorption and fluorescence spectra of a DGU structurally sorted ensemble of (6,5) enriched CoMoCAT. The fractions are designated as f1-f14 from top to bottom. **b.** Absolute photoluminescence quantum yields as a function of fraction number. **c.** Measured fraction density versus estimated crystallite size. The crystallite sizes are calculated with the aid of AFM data from figure 8 a in chapter 3.

The visible pump-infrared probe experiment is not very well understood from an isolated tube level due to the branching of the E_{22} exciton into different decay channels. Therefore, the visible pump-infrared probe experiment should contain a convolution of the dynamics in E_{22}, E_{11}, and the ground state filling. By doing a systematic study of the change in dynamics of the E_{22} pump E_{11} probe experiment as compared to changes in the quantum yield more can be learned about the nature of this non-linear response. Here, the initial dynamics of the E_{22} pump-E_{11} probe experiment as a function of fraction density or equally crystallite size decrease with increasing density, Fig. 2 a. The first 5 ps of the cross correlations are fit with a single exponential and the decay times are plotted versus

fraction density in figure 2 b. The decay decreases linearly with density and suggest as stated before that the number of additional non-radiative decay channels increases with crystallite size. This gives insight to the visible-pump infrared probe experiment in which the initial decay most likely reflects the non-radiative decay. The exact mechanisms will be addressed in later sections where the amplitude of the transient absorption spectrum, and other pump probe configurations reflect the presence of sub 100 fs decay channels, changes in the intersystem crossing time of the E_{11} exciton, and triplet state diffusion through a crystallite.

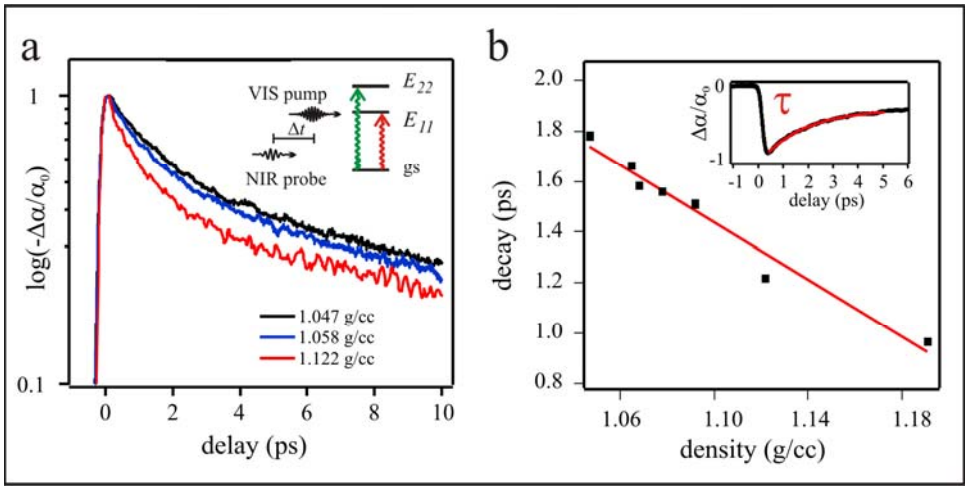

Figure 2 a. Cross correlations of E_{22} pump E_{11} probe for three different fractions from Fig. 1. a. **b.** Decay times found from fitting the first five ps with a mono-exponential fit (inset). The decay time decreases with increasing fraction density, which suggest increasingly larger bundles, which have a smaller quantum yield than isolated tubes, have a shorter excited state lifetime. The line is a guide to the eye.

B. Dielectric Environment, Delocalization, and Free Carriers

The absorption and emission spectra from figure 1 are red-shifted with respect to the isolated tube spectra as a function of crystallite size. The magnitude of the red-shift from the isolated tubes to an average tube crystallite size of approximately 5, figure 1 c, is on the order of 10 meV or 1%. An analysis of the line positions show that there is a correlation between absorption and emission with a Stokes shift that varies from approximately 5 meV in isolated tubes to 2 meV in crystallites, Fig. 3 a. The isolated tube Stokes shift is similar to recently reported shifts in individual (6,5) tubes of 5 meV [Ber07]. The correlation suggest that small tube crystallites do emit but it may only be a minority due to the large optical density in this size range, therefore the rest of the discussion in this section and section C will focus on the minority of emitters and the majority of non-emitters will be disused in section D. Size dependent Stokes shifts have been experimentally and theoretically shown to occur in CdSe nanocrystals in which the lowest exciton is dipole forbidden [Efr96]. The thermalization of the lowest dark and bright exciton lead to a Stokes shift which is dependent on nanocrystal size and in turn the dark-bright exciton splitting. It is found that the smaller the crystal the larger the splitting.

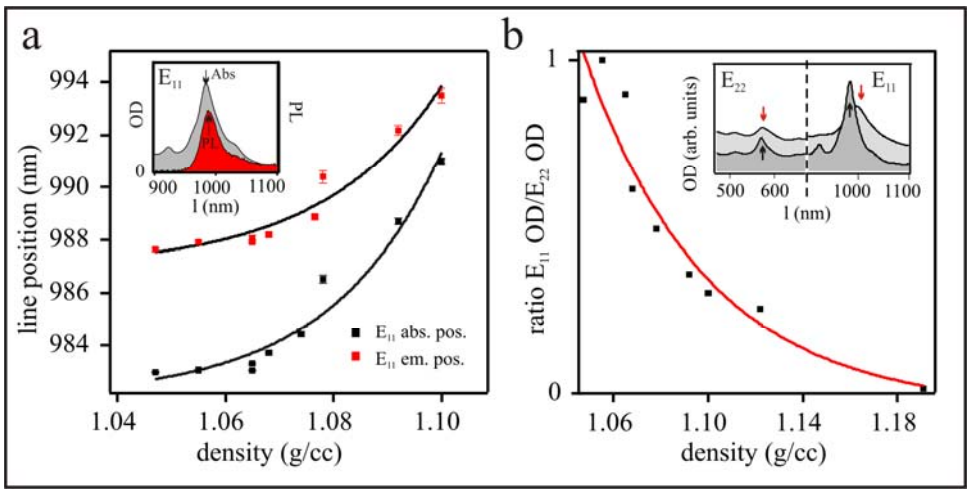

Figure 3 a. Line positions for both the E_{11} absorption and E_{11} emission features versus fraction density from the sample in Fig. 1. The correlations between the features suggest small tube bundles fluoresce. **b.** Ratio of the optical density at the E_{11} transition and the optical density at the E_{22} transition versus fraction density, the line is a guide to the eye.

In SWNT the energetically lowest exciton is also dipole forbidden and in thermal equilibrium with the bright exciton. Moreover, recent temperature dependent time resolved fluorescence studies show that the (8,3) tube which has a diameter very similar to the (6,5) tube has a dark-bright splitting of 5.3 meV [Mor07] which is in agreement with the stokes shift found here. In order to account for the change in the Stokes shift, the change in the exciton splitting may be responsible as in CdSe. The dark exciton in SWNT is different from the bright exciton due to the vanishing exchange interaction which is fundamentally due to the wavefunction symmetry [Cap06]. Since the exchange interaction is not screened the change in the Stokes shift measured here in directly related to the screened Coulomb interaction.

As shown here for a crystallite composing of approximately five tubes, a change in the Stokes shift of approximately 50% implies the Coulomb interaction is reduced by 50% which in turn increases the size of the exciton, decreases the binding energy, and

decreases the oscillator strength. The screening of Coulomb interaction, which depends on the dielectric function determined by the number of tubes in a crystallite and what (n,m) species they are, should manifest itself in the Sommerfeld factor of the system [Oga91]. The Sommerfeld factor is a measure of the ratio of the absorption intensities of the free carriers associated with band-to-band transitions and the absorption intensity of the exciton associated with the band. In figure 3 b the ratio of the optical density at E_{22} and the optical density at E_{11} is plotted verses fraction density. It is found that this ratio decrease with crystallite size and what would be expected for an increase in the Sommerfeld factor. Since the E_{22} exciton is embedded in the E_{11} continuum, an increase in the optical density at E_{22} due to a nonresonant background reflects an increased response from the E_{11} continuum. Moreover a change in the E_{11}/ E_{22} ratio from isolated tubes to where a crystallite of approximately five tubes is approximately 50% which is in agreement with the changes in the Stokes shift.

The E_{11} exciton becomes delocalized in the presence of other tubes, because the screening of the Coulomb interaction modifies the dimensionality of the exciton. Delocalization most likely does not involve the formation of a dispersion perpendicular to the tube axis due to momentum mismatches, and recent Rayleigh scattering studies of the E_{33} and E_{44} transitions on single suspended tubes show that intratube interactions induce dielectric screening but the states are just superpositions of the individual component of the crystallite [Wan06]. However, when excitonic effects are important as in the lowest two subbands dispersion may become important and needs to be addressed at the single tube level. The effects of the screening can best be understood by investigating two

separate models of the Coulomb interaction one including the change in dimensionality and the other the strength.

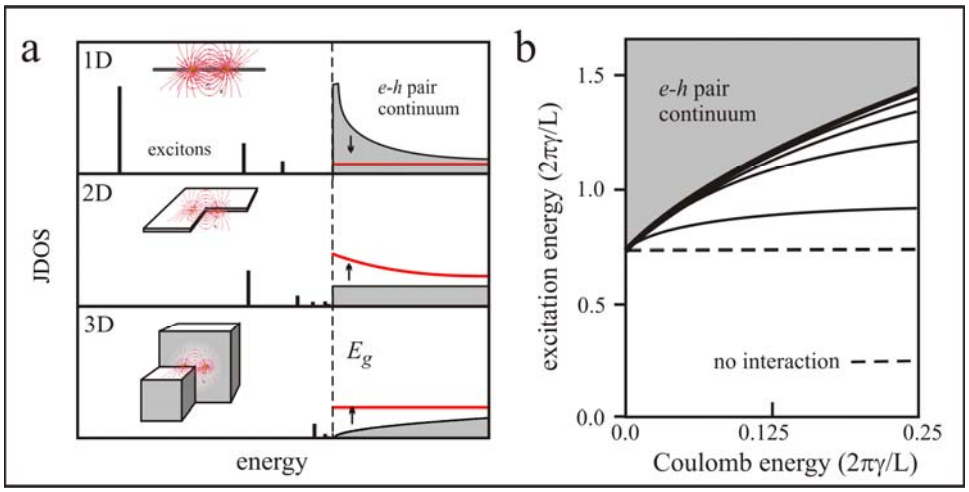

Figure 4 a. The joint density of states in 1,2, and 3 dimensions for both ionized and bound excitonic states using the Wannier formalism. The increased absorption from the continuum as the dielectric dimensionality of the system changes accounts or the trend of the decreased ratio of the optical density at the E_{11} transition and the optical density at the E_{22} transition versus fraction density in Fig. 4. b. **b.** The excitation energy of excitons within a chiral tube versus the effective strength of the Coulomb interaction for both electron-electron interactions and electron-hole interactions [And97]. As the Coulomb interaction is increased more excitonic states appear and there is a blueshift in the excitation energy. Even though the exciton binding energy is increased by the interaction, the opening of the free particle gap dominates this effect.

Solving the phenomenological Wannier equation in d=1,2, and 3 dimensions for both bound and ionized excitons can be used to qualitatively explain the effects of the change in dimensionality of the Coulomb interaction between electron and holes [Hau04], Fig. 4 a. As the interaction changes from three to one dimensions the free carrier response is reduced and the excitonic effect become significant. Also, the binding energy and oscillator strength is affected by the dimensionality. The effects of the free carrier response and the oscillator strength are apparent in figure 1, but the reduced

binding energy is inconsistent with the observed red shifts. By including the electron-electron interaction within the Hartee-Fock approximation and the $\vec{k} \cdot \vec{p}$ scheme it was shown that even though a weaker interaction reduces the binding energy of the exciton, the free carrier gap is reduced to overcome this and produces a red shift in the excitation energy, Fig. 4 b. Additionally, as the interaction is increased there is a blue shift of the excitation spectra and more and more excitonic states appear, and if the interaction is very weak no excitons are apparent at all [And97]. The excitation energy in units of $2\pi\gamma/L$, where γ is a band parameter in eV and L is the tube length, is plotted versus Coulomb energy in units of $2\pi\gamma/L$. For a change in the strength of the interaction from 0.25 to 0.125 or 50% the excitation energy is red shifted by approximately 1% which is in agreement with the shift of the E_{11} in the absorption and emission spectra. By including the interpretation of both of these models, the effect of the dielectric environment on the change in dimensionality of the Coulomb interaction can qualitatively explain the observed changes in the spectra. The dynamics of the excited states will be disused in the next two chapters.

C. Intertube Coupling Effects on Intersystem Crossing

In chapter 4 the radiative decay of isolated SWNT ensembles prepared by DGU was found to be approximately 800 ps by considering the experimental values of the quantum yield, 1%, and the non-radiative decay, 8.8 ps. Moreover, the changes in the quantum yield as a function of fraction density or crystallite size in figure 1b along with the E_{22} pump E_{11} probe decay times in figure 2 b suggest that the non-radiative rate is

increased by intertube interactions. Since the optical density at the E_{22} exciton in crystallites is larger than in isolated tubes it can also be inferred that only a minority species of crystallites fluoresce while the majority are quenched by additional non-radiative decay channels. The crystallites that do not fluoresce must have states that decay very fast as in grapheme, which would be expected in a crystallite containing metallic tubes.

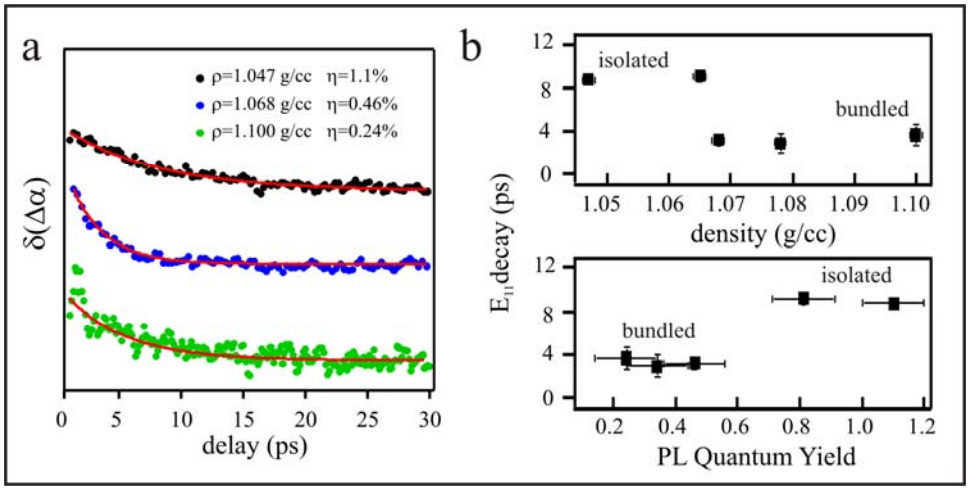

Figure 5 a. Non-radiative lifetime cross correlations of the E_{11} exciton of the (6,5) tube in different bundle configurations found by subtracting the cross correlation of the ground state filling, E_{11} pump E_{22} probe, from the ground state filling plus E_{11} excited state lifetime, E_{11} pump E_{11} probe. **b.** The non-radiative lifetimes of the (6,5) E_{11} exciton versus fraction density and photoluminescence quantum yield.

Here, the investigation of the role of the change in dimensionality of the Coulomb interaction on the non-radiative decay of the E_{11} exciton is carried out using infrared pump and both visible and infrared probe experiment. Similar to the isolated tube case the transient are characterized by an initial decay that differs in both experiments and a power law decay that persist for nanoseconds. The E_{11} pump E_{22} probe cross correlation

is normalized to the E_{11} pump E_{11} probe cross correlation and subtracted to get the excited state lifetime of the E_{11} exciton, Fig. 5 a. The non-radiative decay of five different fractions which range from isolated tubes to crystallites of an estimated size of 5 is shown versus density and quantum yield in figure 5 b. In chapter 4 the isolated tubes non-radiative decay was assigned to be an 8.8 ps intersystem crossing from the thermalized lowest energy excitons to a triplet exciton. The spin orbit coupling was found to be approximately $\Delta_R \approx 1°\text{K}$ and efficiently scatters bright singlet exciton into the triplet exciton manifold.

If the intersystem crossing was affected by the change in dimensionality of the Coulomb interaction as the absorption and emission spectra suggest, then tubes with like quantum yields should have similar non-radiatve decay times. This is exactly what is found here and suggest that the spin-orbit coupling, the triplet density of states, or both are simultaneously changed due to screening. Since the free-carrier contribution of the optical response is increased by roughly 50% for a 5 tube crystallite according to the ratio measured in figure 3 b, this implies the density of states of the triplet excitons should also change by approximately 50%, Fig 6 a. Therefore, according to the golden rule the spin-orbit interaction would have to increase by approximately 50% from the isolated tubes in order decrease the ISC time. The increased strength of the SO interaction may be due both the intrinsic spin-orbit interaction found in isolated tubes and another term due to the disordered dielectric environment produced by intertube coupling such that $\Delta = \Delta_R + \Delta_{env}$, Fig. 6 b. The spin-dephasing time due to the disordered dielectric environment may be decreased which in turn decreases the time it takes to flip a spin.

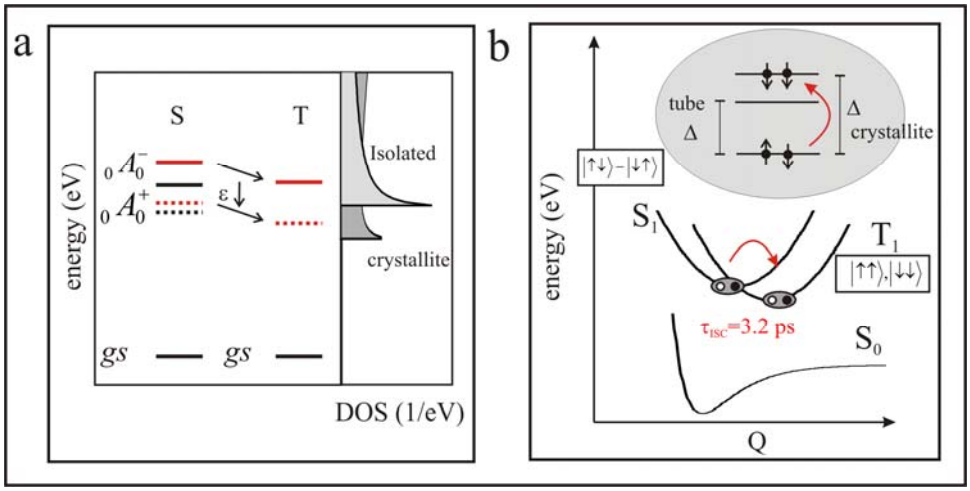

Figure 6 a. Schematic of the ordering of the exciton states and triplet density of states for an isolated and tube under the influence of a dielectric environment. The local dielectric environment reduces the coulomb interaction and causes a redshift of the states as in Fig. 4. b, and level splitting between the bright and dark states is reduced from the isolated tube case. Also, the density of states is changed by the change in dimensionality of the Coulomb interaction. **b.** Schematic of the intersystem crossing process for the bright singlet state and its triplet counterpart in the presence of a dielectric environment. The spin-orbit coupling is increased which decreases the ISC time.

D. Electron and Exciton Energy Transfer

The understanding of electron and exciton energy transfer in SWNT crystallites is important for applications in optics and electronics. Transport experiments shed light on transfer phenomena when excitonic effects are negligible due to the injection of electrons or holes from an electrode. When contacts are placed on opposite ends of a random network the inherent statistical mixture of 2/3 semiconductor and 1/3 metallic may lead to conduction pathways that bypass the semiconducting tubes. Devices such as this can be tailored to be below or above the metallic percolation threshold for field-effect transistor or conductive-electrode applications [Bra03, Sno03, Sno04, Sno05, Hu04, Shi04, Oze05, Byo06]. The current notion is that intertube conduction is greatly reduced

at the metal/metal and semiconductor/semiconductor interface due to momentum mismatches and small tunneling amplitudes [Boc97, Maa00]. Moreover, metal/semiconductor junctions introduce Schottky barriers that have even higher resistances than the metal/metal or semiconductor/semiconductor junctions [Sta04]. In terms of photexcitations, it is not very well understood how the complication of excitonic effects affect energy and charge transfer.

It is well known from classical electromagnetic theory that when an oscillating dipole is placed next to a metal surface the surface plasmons couple to the near field of the dipole and transfer energy non-radiatively [Cha75]. A distance dependent non-radiative decay rate constant is found $k_{me} = k_0 (x_0 / x)^3$ where k_0 is the dipole decay rate and x_0 is the characteristic distance of energy transfer describes the process. Additionally, singlet exciton energy transfer (EET) in light harvesting polymers and bacteria is described in terms incoherent EET or Förster's theory [Web90, Koe96]. The EET transfer rate from donor (D) to acceptor (A) is given by $k_{DA} = k_0 (x_F / x)^6$,where k_0 is the radiative decay of D and x_F is the distance at which the radiative decay rate is equal to the transfer rate. Förster transfer is only valid for systems with a homogeneous linewidth that is greater than the intermolecular interaction and intermolecular distances on the order of 1nm. Under these criteria the excitons are able to migrate diffusively throughout the network until a minimum in energy is reached, while the converse leads to coherent exciton motion that couples neighboring molecules. Additionally for small intermolecular spacings, the exchange interaction may have to be taken into account and electron or hole transfer may be encountered [May04].

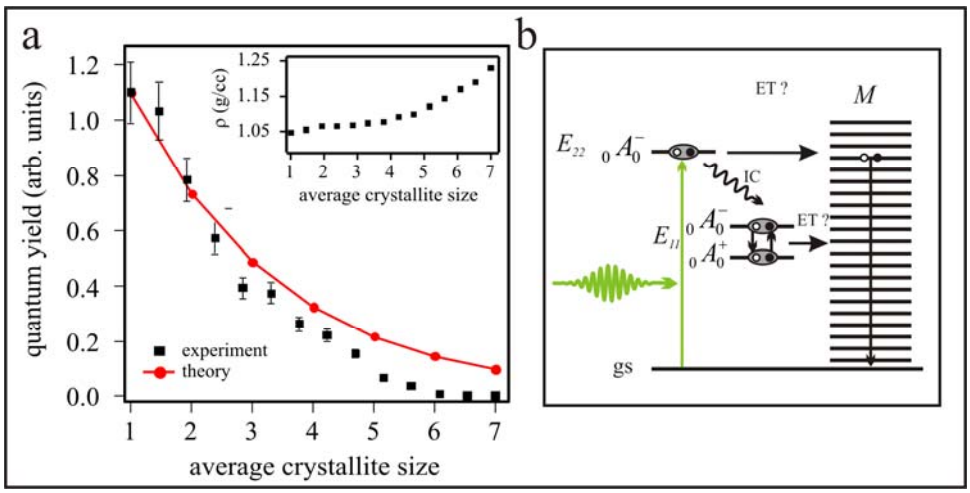

Figure 7 a. Experimental quantum yield versus average crystallite size computed from the experimental fraction density (black) and theoretical quantum yield versus bundle size considering the quantum yield is proportional to the probability of a bundle of a certain size to contain at least one metallic tube (red). The fraction of metallic tubes within an ensemble is assumed to be the statistical average of 1/3. The inset is the calculated average crystallite size for a given fraction density. **b.** Schematic of the coupling of a semiconducting tube to a metallic tube and the quenching of the photoluminescence by energy transfer (ET) from the E_{11} or E_{22} exciton to a continuum of e-h pairs. This scheme works for bundles of a few tubes but their must be additional non-radiative decay channels activated by intertube interactions that can explain the deviation from the model for larger crystallites.

In the case of SWNT crystallites, the intertube interaction (which is estimated to be on the order of the interplane dispersion of grapheme) is approximately 200 meV for chiral tubes [Rei02]. Moreover, the homogeneous linewidth of the E_{11} exciton in isolated SWNT in this diameter range is on the order of 15 meV and the E_{22} exciton 80 meV [Ino06, Chapter 4]. Energy transfer between semiconductors in this regime can be described by coherent exciton energy transfer or by photoinduced electron or hole transfer also known as Dexter transfer. This can take place on a time scale of $t_{el} = \hbar/|V_{AD}|$ where $|V_{AD}|$ is the intermolecular interaction. The rate of electron/hole transfer is formally given by,

$$k_{ET} = -\lim_{t\to\infty} \frac{1}{t} \ln P_D(t), \tag{1}$$

where $P_D(t)$ is the population of the electron/hole donor. Electrons and holes can become bound between molecules in a so called charge-transfer exciton configuration which has been reported for crystalline C-60 [Ich98, Pac98].

The change in the quantum yields η of the fractions from figure 1 can be partially accounted for by considering that, $\eta(n) = \eta_0 (1-f)^{n-1}$, where η_0 is the quantum yield of the isolated tubes, f is the total fraction of metallic tubes in the sample, and *n* is the number of tubes in the crystallite. This relation is derived by considering that the fluorescence of a crystallite composing of *n* tubes can be quenched by at least one metallic tube that makes up *f* percent of the initial ensemble, and the statistical composition of a crystallite is given by the hypergeometric distribution. For fraction of metallic tubes *f*=1/3, $\eta(n)$ is plotted in figure 7 a. Non-emissive tubes make up the majority of the crystallites and this particular scenario is schematically shown in figure 7 b. Choosing a larger value of *f* =2/5 can give the best fit, while choosing f =1/12 in accordance with a recent Raman characterization of the abundance of tube species in CoMoCAT fails miserably [Jor05]. It is most likely, that the samples do not contain more than 1/3 metallic and 1/12 may be the lower bound. In both cases the model does not fit the data for the later fractions and the quenching of the PL must be from an additional intertube or intratube mechanism. Additionally, the branching from E_{22} to E_{11} may decreases from 90% as in the isolated tube case in chapter 4 due to the reduction of oscillator strength transferred to E_{11} resulting in more free e-h pairs that do not combine radiatively.

The transient absorption spectrum at zero pump probe delay reflects the instantaneous population change in the difference of the excited and ground states, $\left(\Delta\alpha/\alpha_0\right)_{t=0} \propto \left(\Delta\rho_{ii} - \Delta\rho_{00}\right)_{t=0}$. If this signal is normalized for the optical density at the corresponding probe wavelength, then the amplitude is directly related to the minority species who have not recovered their ground state within the time resolution. Here, this is emphasized by plotting the normalized transient absorption at the (6,5) E_{11} and E_{22} under resonant E_{11} excitation along with the normalized quantum yield and normalized optical density ratio from figure 3 b versus crystallite density, Fig. 8 a.

The correlations shown suggest that the majority species undergo a very fast recovery that is less the time resolution of the experiment. This is not very surprising due the strong interaction between tubes and the small intertube spacing that allow for possible wavefunction overlap. Moreover, if a metallic tube is in the crystallite it is likely the whole tube will be metallic and the ground state recovery of the tube being probed will be limited by transfer of energy to the metallic tube. Since the plasmon frequency for metallic tubes of 0.8 nm diameter is approximately 4.5 eV and the plasma frequency 0.15 fs, suggest free electrons and holes could damp the dipole associated with the E_{11} or E_{22} exciton that has a frequencies of approximately 0.5 fs and 0.3 fs. This would make energy transfer from the E_{11} or E_{22} exciton to the metallic continuum very efficient and explain the some of the observed changes in quantum yield and the normalized transient absorption. Additionally for a nearby semiconductor if a charge transfer exciton were to form at the E_{11} or E_{22} exciton among neighboring tubes within t_{el}=3.3 fs, non-radiative decay could take place within 100 fs due to dipole forbidden charge transfer states lower in energy, Fig. 8 b.

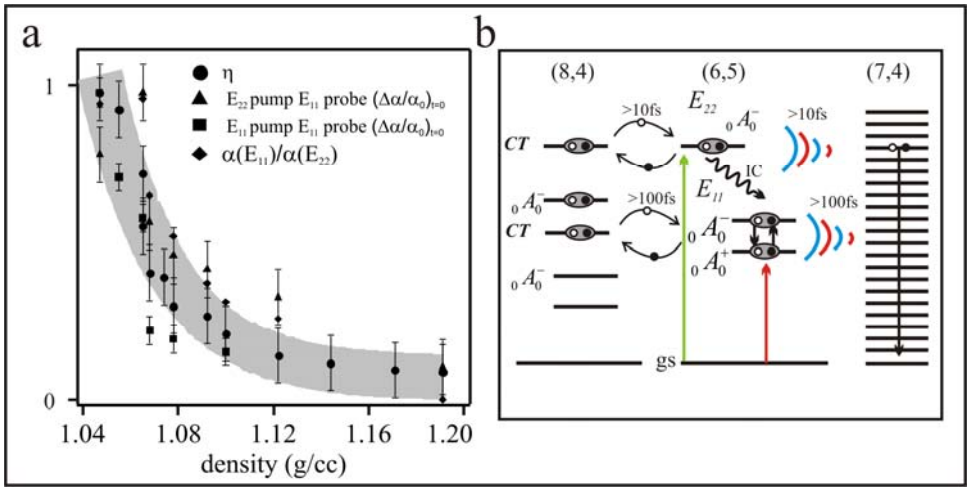

Figure 8 a. The relative quantum yield, ratio of the E_{11} optical density and the E_{22} optical density, transient absorption for E_{11} pump E_{11} probe at zero delay normalized for the E_{11} optical density, and transient absorption for E_{22} pump E_{11} probe at zero delay normalized for the E_{22} optical density versus fraction density for the (6,5) tube. The correlation between all of the data suggest the magnitude transient absorption signal for either pump probe configuration reflects the change in quantum yield along with the degree of continuum absorption for a specific crystallite size. **b.** Schematic of the possible processes and bounds on the time scales that intertube relaxation can take place. After E_{11} excitation in less than 100 fs E_{11} excitons relax by energy transfer to metallic tubes, smaller band gap semiconducting tubes, or similar tube species. The E_{22} exciton has a lifetime of 10 fs therefore all intertube processes must take place within this time scale in order for energy transfer to take place from E_{22}.

Non-emissive states due to intertube coupling between semiconductor tubes is more apparent in figures 9 a and b. Here, the top spectra are from a SDBS CoMoCAT supernatant that was aged for over two years and displayed fluorescence. Surprisingly this not only demonstrated the stability of SWNT suspension, but also revealed features that were not present initially. There is clear energy transfer from the (6,5) tube to the (8,4) tube in the PLE spectra and no clear energy transfer from fraction f8 from figure 1. Fraction f8 contains an estimated 5 tubes per crystallite and has a quantum yield of approximately 0.2%, and the SDBS sample contains an admixture of isolate tubes and tube crystallite with a quantum yield of also approximately 0.2%. Even though the

quantum yields are similar the absorption and PLE spectra indicate quite different processes are taking place. Fraction f8 shows a large background of fluorescence in between the (8,4) and (6,5) emission, and most likely to due the inhomogeneity of the sample. While, the SDBS sample has well defined peaks at the (6,5) and (8,4) along with a well defined peak emanating from (6,5) excitation and (8,4) emission.

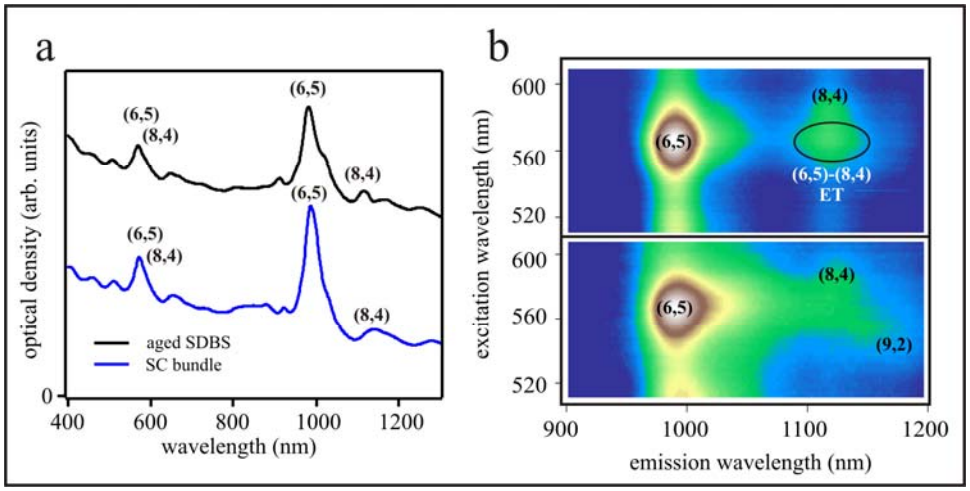

Figure 9.a. Absorption spectra from an aged SDBS encapsulated CoMoCAT (6,5) enriched sample and fraction f8 from Fig 1. The predicted average crystallites size for fraction f8 is 4.7, while the SDBS sample contains an ensemble of isolated tubes and crystallites of various sizes. **b.** Photoluminescence excitation spectra of the samples from the left. The top sample showed no signs of energy transfer when is was initially prepared. Fraction f8 shows no clear signs of ET as in the SDBS sample, which suggest the structure of the aggregate is different in each sample.

In the SDBS sample it is most likely that aging has produced loose bundles of tubes that have surfactant spacers in between them that reduce the van der Waals interaction significantly, while in the crystallite the tubes are packed in a hexagonal array and are strongly bound. The weak interaction in the former allows for Förster type transfer where excitons can diffuse throughout a network due to negligible overlap of

wavefunctions. Moreover, the transfer rate is proportional spectral overlap of the donor and emitter and as seen from the absorption spectra there is no spectral overlap between the (6,5) and (8,4) E_{11} excitons and significant overlap between the E_{22} excitons.

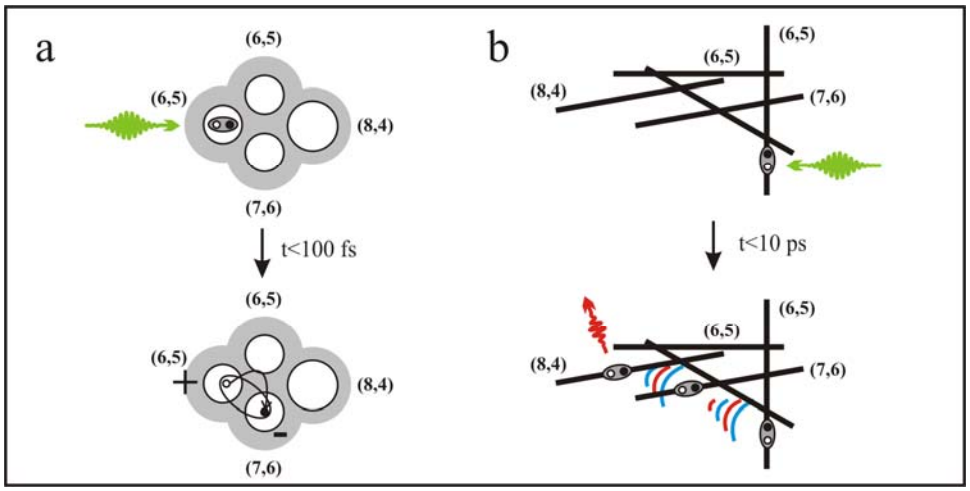

Figure 10 a. Schematic of a nanotube crystallite where the overlap of orbitals can lead to an ultrafast photoinduced charge transfer that leads to a pair of charged species and a charge transfer exciton. **b.** Schematic of a loose aggregate of nanotubes in which exciton energy transfer can take place through dipolar coupling as long as it is faster than the intersystem crossing time.

In order for transfer to occur from E_{22} it must be faster than 10 fs and is very unlikely for this type of mechanism which tends to be on the order of 10 ps in polymer blends [Dog99]. On the other hand funneling can occur by successively hopping from one tube to the other until the energy minimum is found where fluorescence can take place [Scho03]. In the crystallite Dexter transfer or coherent exciton energy transfer may lead to delocalized excitons that can quickly localize by scattering with phonons. Additionally, the number of excitons initially created may be less than in isolated tubes due to the enhanced free carrier response as a result of the change in the dimensionality of the Coulomb interaction. Non-radiative decay tends to dominate the dynamics in this

scenario and needs to be further investigated at the single crystallite level. A schematic of the two different length scales and types of transfer are shown in figures 10 a and b.

E. Ground State Recovery and Charge Migration

The transient absorption signal measured was shown in section C to be due to the minority species which can possibly fluoresce if intertube interactions do not cause non-radiative decay. Of the minority species that do fluorescence the branching will be similar to the isolated tubes as shown in chapter 4, but with a decrease in the number of excitons filling the E_{11} subband and a faster intersystem crossing time due to a reduction in the exciton density of states. Once triplets are formed on the exited tube they can persist for many ns and could migrate from one tube to another by charge or energy transfer. If this were to happen one would expect the ground state of the minority species to be filled at a slower rate due the migration of charges throughout the crystallite. By tracing the long decay of the photobleach associated with the E_{11} pump E_{11} probe experiment and fitting the dynamics to a power laws this can be exactly seen, Fig. 11 a and b. In isolated tubes it was shown that the ground state recovery was limited by triplet-triplet annihilation or sub-diffusive trapping of triplets described in 1-D by $t^{-1/2}$. As the crystallite size gets larger the exponent is reduced here from -1/2 and for the last tube that has non-zero quantum yield is approximately -2/5.

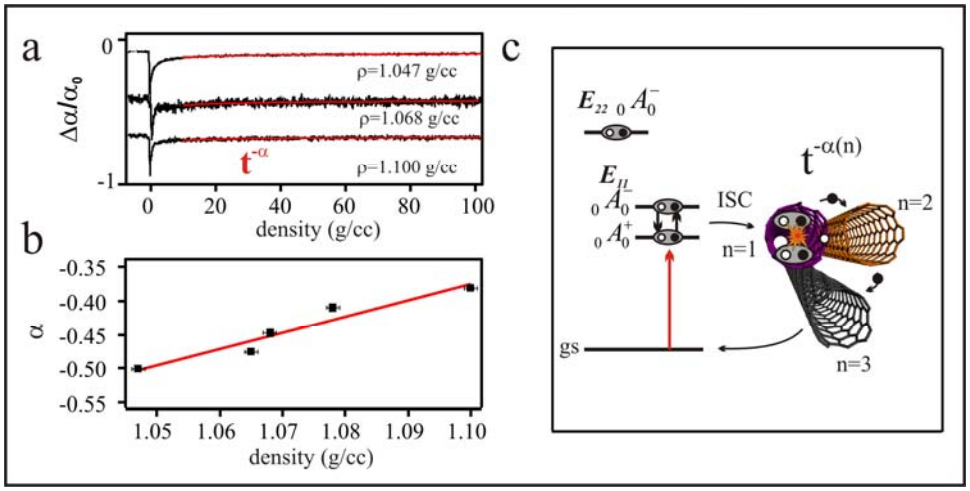

Figure 11 a. Cross correlations of resonantly pumping the E_{11} exciton of the (6,5) tube and probing resonantly the E_{22} exciton for three different fractions with increasing density or crystallite size. **b.** Power scaling for different fraction densities. The time dependence of the ground state recovery, given by α, increases with increasing crystallite size. **c.** Schematic of how intertube coupling increases the time it takes to recover the ground state of the (6,5) tube.

The exact mechanism responsible for the prolonged recovery of the ground state can be interpreted as long lived charged species, which has recently been reported for crystallites of HiPco tubes in a polymer matrix [Gad06]. Exciton dissociation may take place during a triplet-triplet annihilation process and leave behind a charge species who's ground state recovers more slowly due to charge migration within a crystallite, Fig 11 c. The change in the power law scaling suggest that exciton energy transfer is not responsible because this would show an opposite trend in the change of the exponent where diffusion would become more Fikian like and during the transfer the donor is left in the ground state. Moreover, since the free carrier response is enhanced due to the change in dimensionality of the Coulomb interaction free carriers may be created during photexcitation and migrate through out the crystallite.

F. Summary of the Intertube Relaxation Mechanisms

Intratube energy transfer can manifest itself in two ways dependent on the composition of the crystallite and the local environment of the exciton. If the environment is conducive, for example no metallic tubes are present or the local dielectric function prevents significant wavefunction overlap with a nearby semiconducting tube, for an E_{22} exciton to undergo an internal conversion to the E_{11} exciton manifold radiative recombination may take place. Only a fraction of the total population of a size sorted ensemble was shown to do this. The yield of this process is reduced by a factor 5 from the isolated tubes in crystallite of an average size of 4.7 tubes due to the change in dimensionality of the Coulomb interaction. This is partly due to the branching ratio is reduced to by 50% due to the decrease in the oscillator strength associated with the E_{11} exciton and a simultaneous increase free carrier response. Changes in the interaction also alter the spitting of the bright and dark excitons much like what is seen in the size dependent bright dark splitting in CdSe nanocrystals. Moreover, of the 50% of excitons that do enter the E_{11} manifold the intersystem crossing most likely becomes more efficient due to fluctuations in the dielectric function that allow for a spin to flipped. Recovery of the ground state is also affected by the change in the environment. If triplet-triplet annihilation accounts for the observed power law dependence of the long transients observed, then free carriers may be generated due to dissociation of one the excitons. The free carries could then scatter from tube to tube and prolong the recovery. Dexter transfer is most likely not the mechanism could this would

increase the recovery time by quenching the triplets on the tube being probed. A summary of the observed changes in the minority species is given in figure 12.

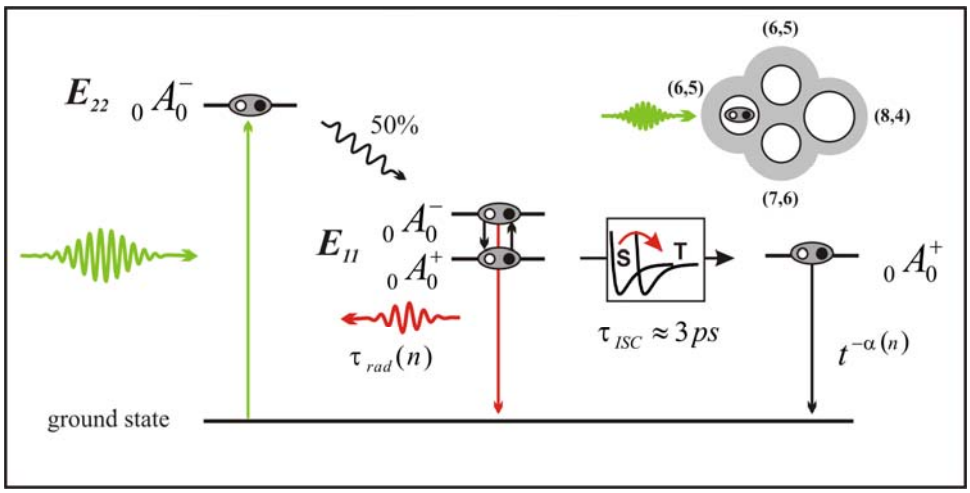

Figure 12. Schematic of the relaxation pathway for tubes that do fluoresce when they are under the influence of intertube coupling in crystallite of approximately 4 tubes. After relaxation from the E_{22} exciton the E_{11} excitons can live long enough to fluoresce, but it is strongly dependent on the local dielectric environment which is a function of the number of tubes within a bundle ***n***. The majority of states, just as in the isolated tubes, undergo an ultrafast internal conversion that is twice as fast as the isolated tubes. The triplet states then are subjected to a diffusive process in which again the number of tubes in a bundle dictates the dynamics of the ground state recovery. Such processes may involve the generation of free carriers that can diffuse throughout the crystallite after a triplet-triplet annihilation event.

Analysis of the spectroscopy indicates that the majority of crystallites do not fluoresce and the ground state of the tube being probed recovers very fast. If a metallic tube such as the (7,4) tube is next to a (6,5) tube then once a dipole is induced it can be damped on a time scale that is equivalent to the plasma frequency which has a period of approximately 0.15 fs. This suggest that E_{22} excitons could be quenched very efficiently with a lifetime of 10 fs, and if an internal conversion were happen to take place within the (6,5) tube quenching would take place from the E_{11} exciton. For the time resolution used in the

pump probe experiments an upper bound of 100 fs can be placed on energy transfer to metallic tubes. Additionally, similar changes in the quantum yield as a function of crystallite size was observed for (6,5) engineered crystallites suggest that when semiconductor tubes are packed into a crystallite similar quenching can take place. Since the tubes are bound together with rather strong van der Waals interactions and the distance between tubes is on the order of 0.3 nm the intertube exchange interaction can no longer be neglected. This can lead to charge transfer between tubes and ultimately charge transfer excitons that may or may not be optically active. A schematic of the non-radiative processes introduced by intertube energy transfer are shown in figure 13.

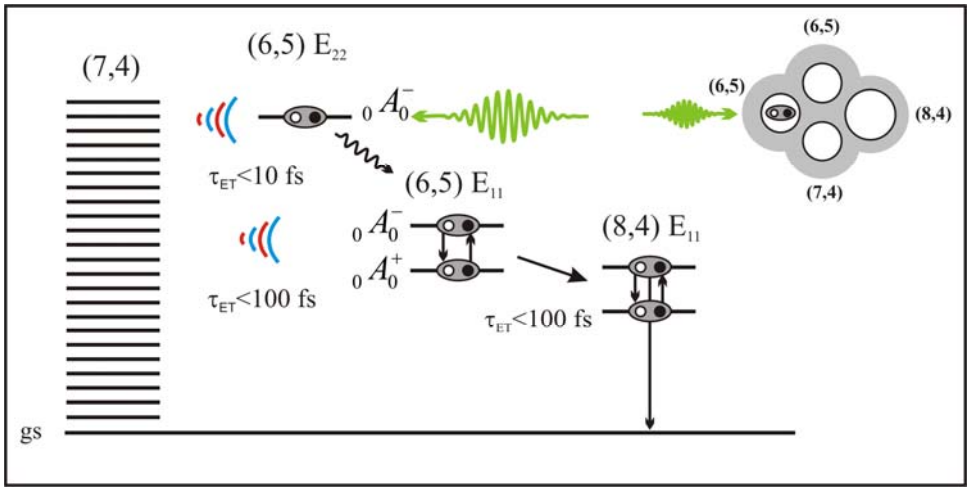

Figure 13. Schematic of the relaxation pathway for tubes that no longer fluoresce, but are responsible for electron or energy exchange with in a tube crystallite. The E_{22} exciton can be coupled directly to a continuum of electrons and holes associated with a metallic neighbor and result in energy transfer that is faster than the lifetime of the E_{22} exciton. Conversely, the very short lifetime of the E_{22} exciton result in a coupling between the E_{11} exciton and the metallic states. In the case there are no metallic tubes within the bundle, exciton energy transfer or ultrafast electron transfer can lead to an additional non-radiative decay channel. An upper bound on both processes can be assigned within the time resolution of the pump probe experiments.

G. References

[And97] Ando, T. (1997). "Excitons in carbon nanotubes." Journal of the Physical Society of Japan **66**(4): 1066-1073.

[Ber07] Berciaud, S., L. Cognet, et al. (2007). "Absorption spectroscopy of individual single-walled carbon nanotubes." Nano Letters **7**(5): 1203-1207.

[Boc97] Bockrath, M., D. H. Cobden, et al. (1997). "Single-electron transport in ropes of carbon nanotubes." Science **275**(5308): 1922-1925.

[Bra03] Bradley, K., J. C. P. Gabriel, et al. (2003). "Flexible nanotube electronics." Nano Letters **3**(10): 1353-1355.

[Byo06] Byon, H. R. and H. C. Choi (2006). "Network single-walled carbon nanotube-field effect transistors (SWNT-FETs) with increased Schottky contact area for highly sensitive biosensor applications." Journal of the American Chemical Society **128**(7): 2188-2189.

[Cap06] Capaz, R. B., C. D. Spataru, et al. (2006). "Diameter and chirality dependence of exciton properties in carbon nanotubes." Physical Review B **74**(12).

[Cha75] Chance, R. R., A. Prock, et al. (1975). "Comments on Classical Theory of Energy-Transfer." Journal of Chemical Physics **62**(6): 2245-2253.

[Dog99] Dogariu, A., R. Gupta, et al. (1999). "Time-resolved Forster energy transfer in polymer blends." Synthetic Metals **100**(1): 95-100.

[Duk04] Dukovic, G., B. E. White, et al. (2004). "Reversible surface oxidation and efficient luminescence quenching in semiconductor single-wall carbon nanotubes." Journal of the American Chemical Society **126**(46): 15269-15276.

[Efr96] Efros, A. L., M. Rosen, et al. (1996). "Band-edge exciton in quantum dots of semiconductors with a degenerate valence band: Dark and bright exciton states." Physical Review B **54**(7): 4843-4856.

[Gad06] Gadermaier, C., E. Menna, et al. (2006). "Long-lived charged states in single-walled carbon nanotubes." Nano Letters **6**(2): 301-305.

[Hu04] Hu, L., D. S. Hecht, et al. (2004). "Percolation in transparent and conducting carbon nanotube networks." Nano Letters **4**(12): 2513-2517.

[Ich98] Ichida, M., A. Nakamura, et al. (1998). "Observation of triplet state of charge-transfer excitons in C-60 thin film." Chemical Physics Letters **289**(5-6): 579-585.

[Ino06] Inoue, T., K. Matsuda, et al. (2006). "Diameter dependence of exciton-phonon interaction in individual single-walled carbon nanotubes studied by microphotoluminescence spectroscopy." Physical Review B **73**(23).

[Jia07] Jiang, J., R. Saito, et al. (2007). "Chirality dependence of exciton effects in single-wall carbon nanotubes: Tight-binding model." Physical Review B **75**(3).

[Jor05] Jorio, A., A. P. Santos, et al. (2005). "Quantifying carbon-nanotube species with resonance Raman scattering." Physical Review B **72**(7).

[Kaz01] Kazaoui, S., N. Minami, et al. (2001). "Electrochemical tuning of electronic states in single-wall carbon nanotubes studied by in situ absorption spectroscopy and ac resistance." Applied Physics Letters **78**(22): 3433-3435.

[Koe96] Koepke, J., X. C. Hu, et al. (1996). "The crystal structure of the light-harvesting complex II (B800-850) from Rhodospirillum molischianum." Structure **4**(5): 581-597.

[Maa00] Maarouf, A. A., C. L. Kane, et al. (2000). "Electronic structure of carbon nanotube ropes." Physical Review B **61**(16): 11156-11165.

[May04] May, V., O. Kühn, (2004). Charge and Energy Transfer Dynamics in Molecular Systems

[Mor07] Mortimer, I. B. and R. J. Nicholas (2007). "Role of bright and dark excitons in the temperature-dependent photoluminescence of carbon nanotubes." Physical Review Letters **98**(2).

[Oga91] Ogawa, T. and T. Takagahara (1991). "Optical-Absorption and Sommerfeld Factors of One-Dimensional Semiconductors - an Exact Treatment of Excitonic Effects." Physical Review B **44**(15): 8138-8156.

[Oze05] Ozel, T., A. Gaur, et al. (2005). "Polymer electrolyte gating of carbon nanotube network transistors." Nano Letters **5**(5): 905-911.

[Pac98] Pac, B., P. Petelenz, et al. (1998). "Charge-transfer exciton band structure in the fullerene crystal-model calculations." Journal of Chemical Physics **109**(18): 7923-7931.

[Rei02] Reich, S., C. Thomsen, et al. (2002). "Electronic band structure of isolated and bundled carbon nanotubes." Physical Review B **65**(15).

[Sch03] Scholes, G. D. (2003). "Long-range resonance energy transfer in molecular systems." Annual Review of Physical Chemistry **54**: 57-87.

[Shi04] Shiraishi, M., T. Takenobu, et al. (2004). "Single-walled carbon nanotube aggregates for solution-processed field effect transistors." Chemical Physics Letters **394**(1-3): 110-113.

[Sno05] Snow, E. S., P. M. Campbell, et al. (2005). "High-mobility carbon-nanotube thin-film transistors on a polymeric substrate." Applied Physics Letters **86**(3).

[Sno03] Snow, E. S., J. P. Novak, et al. (2003). "Random networks of carbon nanotubes as an electronic material." Applied Physics Letters **82**(13): 2145-2147.

[Sno04] Snow, E. S., J. P. Novak, et al. (2004). "Carbon nanotube networks: Nanomaterial for macroelectronic applications." Journal of Vacuum Science & Technology B **22**(4): 1990-1994.

[Sta04] Stadermann, M., S. J. Papadakis, et al. (2004). "Nanoscale study of conduction through carbon nanotube networks." Physical Review B **69**(20).

[Tas98] Tasaki, S., K. Maekawa, et al. (1998). "pi-band contribution to the optical properties of carbon nanotubes: Effects of chirality." Physical Review B **57**(15): 9301-9318.

[Wan05] Wang, F., G. Dukovic, et al. (2005). "The optical resonances in carbon nanotubes arise from excitons." Science **308**(5723): 838-841.

[Wan06] Wang, F., M. Y. Sfeir, et al. (2006). "Interactions between individual carbon nanotubes studied by Rayleigh scattering spectroscopy." Physical Review Letters **96**(16).

[Web90] Webber, S. E. (1990). "Photon-Harvesting Polymers." Chemical Reviews **90**(8): 1469-1482.

CONCLUSION

In this dissertation the linear and non-linear optical properties of structurally sorted single-wall carbon nanotube ensembles were investigated. The findings provide insight to the photo-physics involved in the relaxation of optically excited states and the dielectric sensitivity of the Coulomb interaction between charge carriers in one-dimension. This was enabled by the development of a technology based on the work by Arnold et al [Arn06] that allowed for the sorting of nanotube crystallites. As a consequence of the aforementioned structural sorting, it was found that isolated nanotubes make up for only a small fraction of traditionally prepared colloidal suspensions and that the fluorescence quantum yields of isolated CNTs in excess of 1% are 1-2 orders of magnitudes larger than previously reported for ensembles of structurally more heterogeneous samples. [Cro07, Tsy07]. Moreover, the reduction in ambiguities due to spectral congestion caused by sample inhomogeneities and small residual nanotube crystallites has allowed for detailed investigation of the microscopic mechanisms involved in intratube and intertube energy and charge transfer.

Intratube Energy and Charge Transfer:

When compared to common laser dyes such a fluorescein – whose quantum yield is approximately 100% - single-wall carbon nanotubes are not particularly efficient fluorophores. With quantum yields found here to be approximately 1% most of the absorbed energy from photons is dissapated through non-radiative decay. The non-

radiative decay mechanisms investigated in this work are supported by a resonance picture that includes very efficient internal conversion and intersystem crossings. Upon excitation of the S_2 state – more frequently referred to as E_{22} - exciton – 10% of the excitations will resonantly scatter into the free electron-hole pair continuum of the S_1 state – also known as E_{11} - exciton – and the remaining 90% undergo internal conversion into the S_1 manifold via a zone boundary optical phonon scattering [Her07]. The scattering and relaxation from the S_2 to the lowest momentum states of the S_1 manifold takes place on a time scale of 40 fs which is determined from the dephasing time of the S_2 transition found from the CW linewidth and a subsequent interband relaxation within the S_1 manifold [Man05]. Once the energetically lowest lying S_1 excitons are filled approximately only 1% of the excitons undergo radiative recombination. The energetically lowest lying S_1 excitons are composed of a energetically higher lying bright state and an energetically lower lying dark state that are in thermal equilibrium [Mor07, Ber07]. The remaining 99% of S_1 excitons are most likely coupled to the triplet exciton manifold T_1 through efficient intersystem crossing (ISC) that takes place within 10 ps. Moreover, with a theoretical spin exchange splitting of 70 meV [Cap07] a spin-orbit interaction strength of 1°K is found which is in good agreement with theoretical estimates including σ-π hybridization [Hue06]. The tube is then left with many triplet excitons that decay by triplet-triplet annihilation with a power law recovery of the ground state that scales as $t^{-1/2}$. The validity of the abovementioned intersystem crossing and triplet-triplet annihilations should be investigated by time resolved fluorescence in which a power law scaling of $t^{-3/2}$ should describe the kinetics of delayed fluorescence [Deb52].

Intratube Energy and Charge Transfer:

One of the key findings of the structural sorting mentioned above is that the quantum yield of small tube crystallites decreases monotonically as a function of crystallite size. As a consequence, only a minority of tube crystallites emit and the majority are quenched efficiently through intertube non-radiative decay mechanisms. It was shown in this thesis that if the statistical average of metallic tubes are responsible for the photoluminescence quenching then the observed changes can partially be accounted for but an additional intertube mechanism must be considered. Estimates of the strength of the intertube interaction due to van der Waals forces is on the order of 500 meV per micron of tube length, and the intertube spacing is on the order of 3 Å [O'co02]. In this regime of intermolecular interactions ultra-fast photoinduced electron transfer may be responsible for intertube charge transfer and the exchange interaction between neighboring tubes must be accounted for [Vol04]. This hypothesis is supported by previous studies on aromatic crystals- such as anthracene – where charge transfer excitons are important for the description of the electronic structure induced by the intermolecular interactions [Pop66]. Charge transfer excitons may become an important intertube excitation that should be further investigated on a single crystallite level where high resolution microsopy can resolve satellite peaks in photoluminesnece spectra.

The change in screening of the Coulomb interaction between charge carriers in semiconducting tubes due to the dielectric environment provided by the crystallite was also investigating in this thesis. This work provided preliminary information on microsopic decay mechanisms that deviate from the isolated tube case. The observed

photoluminescence Stokes shift along with changes in the Sommerfeld factors support the picture of an enhanced screening of the Coulomb interaction as the crystallite size is increased. Therefore, the branching ratio of S_2 exciton scattering into the free electron-hole pair continuum of S_1 and internal conversions to the S_1 exciton manifold is almost certainly increased as a function of crystallite size. Moreover, the decay times of the S_1 excitons were found to decrease as a function of crystallite size. Therefore, it is most likely the intersystem crossing observed in isolated tube ensembles becomes even more efficient in crystallites due to the additional spin-orbit interaction that arises from the disordered dielectric environment. These two processes presumably leave photoexcited tubes with more free electron-hole pairs and triplet excitons than in the isolated tube case. This is also evident in the observed prolonged ground state recovery where free charges and triplet excitons may migrate throughout a crystallite. A combination of coupling to metallic tubes, ultra-fast photoinduced electron transfer, and free charge/triplet exciton migration could all be responsible for intertube energy and charge transfer. Additionaly, with the advent of crystallite engineering developed in this work the importance of the above microscopic decay mechanisms may be further addressed by contolling the composition of the crystallites.

References

[And06] Ando, T. (2006). "Effects of valley mixing and exchange on excitons in carbon nanotubes with Aharonov-Bohm flux." Journal of the Physical Society of Japan **75**(2).

[Arn06] Arnold, M. S., A. A. Green, et al. (2006). "Sorting carbon nanotubes by electronic structure using density differentiation." Nature Nanotechnology 1(1): 60-65.

[Ber07] Berger, S., C. Voisin, et al. (2007). "Temperature dependence of exciton recombination in semiconducting single-wall carbon nanotubes." Nano Letters **7**(2): 398-402.

[Cro07] Crochet, J., M. Clemens, et al. (2007). "Quantum yield heterogeneities of aqueous single-wall carbon nanotube suspensions." Journal of the American Chemical Society **129**(26): 8058.

[Deb52] Debeye, P., J. Edwards, (1952). "Long-lifetime phosphorescence and the diffusion process." The Journal of Chemical Physics **20**(2): 236.

[Her07] Hertel, T.,V. Perebeinos, J. Crochet, et al. (2007) "Intersubband Decay of 1-D Exciton Resonances in Carbon Nanotubes," Nano Letters, In Press.

[Hue06] Huertas-Hernando, D., F. Guinea, et al. (2006). "Spin-orbit coupling in curved graphene, fullerenes, nanotubes, and nanotube caps." Physical Review B **74**(15).

[Man05] Manzoni, C., A. Gambetta, et al. (2005). "Intersubband exciton relaxation dynamics in single-walled carbon nanotubes." Physical Review Letters **94**(20).

[Mor07] Mortimer, I. B. and R. J. Nicholas (2007). "Role of bright and dark excitons in the temperature-dependent photoluminescence of carbon nanotubes." Physical Review Letters **98**(2).

[O'Co02] O'Connell, M. J., S. M. Bachilo, et al. (2002). "Band gap fluorescence from individual single-walled carbon nanotubes." Science **297**(5581): 593-596.

[Pop66] Pope, M. and J. Burgos (1966). "Charge-Transfer Exciton State and Ionic Energy Levels in Anthracene Crystal." Molecular Crystals **1**(3): 395-&.

[Tsy07] Tsyboulski, D.A., J.D.R. Rocha, et al. (2007). "Structure-Dependent Fluorescence Efficiencies of Individual Single-Walled Carbon Nanotubes." Nano Letters **7**(10): 3080-3085.

[Vol04] Volkhard, M. and O. Kuhn (2004). "Charge and Energy Transfer Dynamics in Molecular Systems." Wiley-VCH.